UNIVERSITY OF ROCHESTER
LABORATORY FOR LASER ENERGETICS

Volume 105
October–December 2005
DOE/SF/19460-659

LLE Review

Quarterly Report

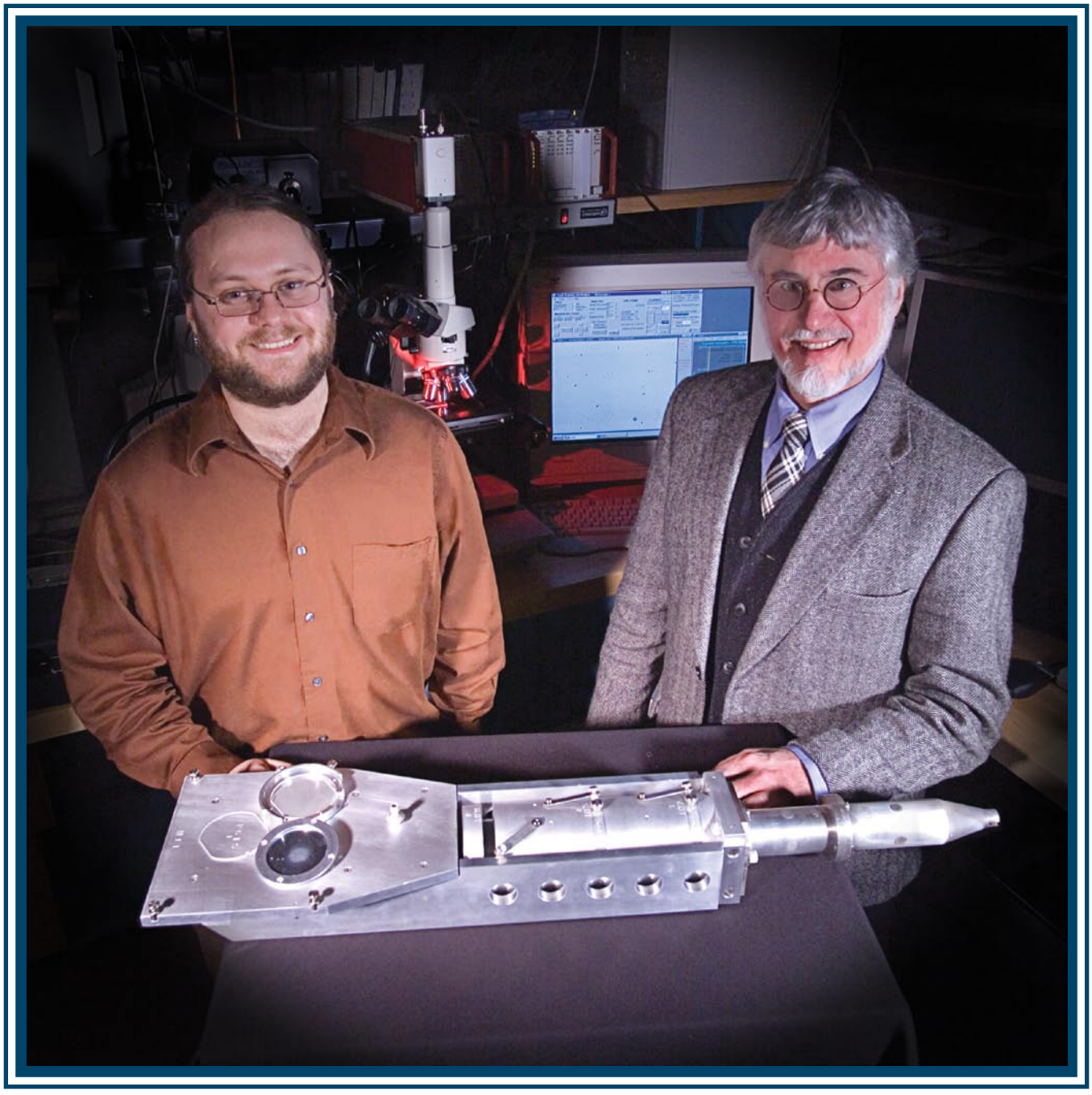

About the Cover:

The front cover shows LLE lab engineer Sam Roberts (left) and MIT scientist Fredrick Séguin (right) inspecting parts of a proton emission imaging camera developed in a MIT–LLE research collaboration. Up to three of these cameras are used simultaneously to study the 3-D spatial distribution of nuclear burn in ICF experiments on the OMEGA laser, as indicated schematically in the diagram on this page. Measurements of the distribution of burn are important because they indicate where fusion reactions actually occur as a consequence of all the complicated processes that affect capsule implosion dynamics. An article in the last issue of the LLE Review (**Proton Core Imaging of the Nuclear Burn in Inertial Confinement Fusion Implosions**, vol. 104, p. 197) described the structure of the cameras themselves, while the lead article in this issue presents the first systematic measurements of the dependence of burn region size on capsule parameters and laser drive parameters for spherically symmetric implosions. Future publications will discuss measurements of the effects of drive asymmetry and capsule shell asymmetry on burn asymmetry. The three sample images in the illustration show the surface brightness of a D^3He burn region as seen simultaneously from three orthogonal directions. Prolate ("sausage-shaped") burn asymmetry resulted from (intentional) laser drive asymmetry.

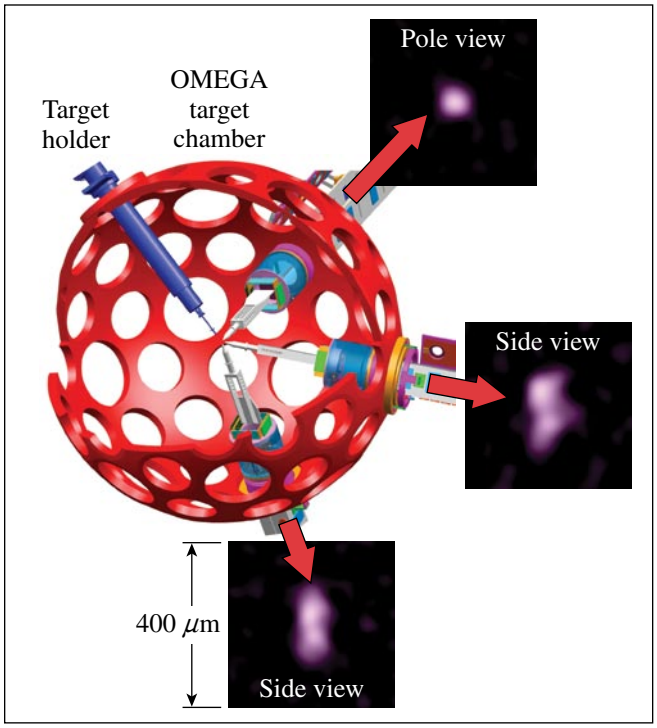

The work described in this volume includes current research at the Laboratory for Laser Energetics, which is supported by New York State Energy Research and Development Authority, the University of Rochester, the U.S. Department of Energy Office of Inertial Confinement Fusion under Cooperative Agreement No. DE-FC03-92SF19460, and other agencies.

Printed in the United States of America
Available from
National Technical Information Services
U.S. Department of Commerce
5285 Port Royal Road
Springfield, VA 22161
Price codes: Printed Copy A04
Microfiche A01

For questions or comments, contact Semyon Papernov, Editor, Laboratory for Laser Energetics, 250 East River Road, Rochester, NY 14623, (585) 275-4259.

Worldwide-Web Home Page: http://www.lle.rochester.edu/

UNIVERSITY OF ROCHESTER
LABORATORY FOR LASER ENERGETICS

Volume 105
October–December 2005
DOE/SF/19460-659

LLE Review

Quarterly Report

UR LLE

Contents

In Brief

This volume of the LLE Review, covering October–December 2005, features "Measured Dependence of Nuclear Burn Region Size on Implosion Parameters in Inertial Confinement Fusion Experiments" by F. H. Séguin, J. L. DeCiantis, J. A. Frenje, J. R. Rygg, C. D. Chen, and R. D. Petrasso (Plasma Science and Fusion Center at MIT), J. A. Delettrez, S. P. Regan, V. A. Smalyuk, V. Yu. Glebov, J. P. Knauer, F. J. Marshall, D. D. Meyerhofer, S. Roberts, T. C. Sangster, and C. Stoeckl (LLE), and K. Mikaelian, H. S. Park, H. F. Robey, and R. E. Tipton (LLNL). In this article (p. 1), the authors report on radial profiles of nuclear burn in directly driven, inertial confinement fusion implosions that have been systematically studied for the first time using a proton emission imaging system at the OMEGA Laser Facility. The system is sensitive to energetic 14.7-MeV protons from the fusion of deuterium and 3-helium. Clear relationships have been identified between variations in the size of the burn region and variations in such experimental parameters as capsule size, shell composition and thickness, gas-fill pressure, and laser energy. Different laser and capsule parameters resulted in burn radii varying from 20 to 80 μm. Since measured burn region sizes indicate where fusion actually occurs as a consequence of all the complicated processes that affect capsule implosion dynamics, they provide exacting tests of simulations.

Additional highlights of recent research presented in this issue include the following:

- V. A. Smalyuk, R. Betti, V. N. Goncharov, J. A. Delettrez, D. D. Meyerhofer, S. P. Regan, and T. C. Sangster (LLE) with O. Sadot and D. Shvarts (Nuclear Research Center at Negev) present results on Rayleigh–Taylor growth measurements of 3-D modulations in a nonlinear regime (p. 17). The measured modulation Fourier spectra and nonlinear growth velocities are in excellent agreement with those predicted by Haan's model. In real-space analysis, the bubble merger was quantified by a self-similar evolution of bubble size distributions, in agreement with the Alon–Oron–Shvarts theoretical predictions.

- M. D. Wittman and D. R. Harding report the results of studies of isotopic fractionation during the solidification of H_2–HD–D_2 mixtures (p. 26). Understanding this process is important since isotopic fractionation during the cryogenic-target layering process reduces the efficiency of the fusion reaction in future cryogenic D-T targets. It is found that H-D mixtures have to be frozen gradually over an ~1-K temperature range to achieve complete solidification. This is indicative of a completely soluble isomorphic system and that fractionation is incomplete. The maximum measured spatial concentration gradients are of the order of 0.02 to 0.05 molecular fraction per millimeter, which also points to little separation of isotopes.

- P. W. McKenty, M. D. Wittman, and D. R. Harding discuss implications of hydrogen fractionation in ICF ignition target designs (p. 35). Numerical investigation of the effects that fractionation has on hot-spot formation, ignition, and burn in ICF target designs indicates that small levels of fractionation (~10%) are acceptable for ignition performance on the NIF.

- J. A. Marozas, F. J. Marshall, R. S. Craxton, I. V. Igumenshchev, S. Skupsky, M. J. Bonino, T. J. B. Collins, R. Epstein, V. Yu. Glebov, D. Jacobs-Perkins, J. P. Knauer, R. L. McCrory, P. W. McKenty, D. D. Meyerhofer, S. G. Noyes, P. B. Radha, T. C. Sangster, W. Seka, and V. A. Smalyuk present results of polar-direct-drive (PDD) simulations and experiments on the OMEGA Laser System (p. 41).

Forty OMEGA beams arranged in six rings to emulate the NIF x-ray-drive configuration are used to perform direct-drive implosions of CH shells filled with D_2 gas. The results of the two-dimensional PDD simulations performed with *DRACO* code are in good agreement with experimental x-ray radiographs. *DRACO* simulations of NIF-scale PDD designs show ignition with a gain of 20 and the development of a 40-μm-radius, 10-keV region with a neutron-averaged ρr of 1270 mg/cm^2 near stagnation.

- S. N. Shafrir, J. C. Lambropoulos, and S. D. Jacobs report on surface features of tungsten carbide composites processed by bound abrasive deterministic microgrinding and magnetorheological finishing (MRF) (p. 51). White-light interferometry, scanning electron microscopy, and atomic force microscopy were used to characterize the surfaces after various grinding steps, surface etching, and MRF spot taking. It was found that the peak-to-valley microroughness of the surface after microgrinding with rough- or medium-abrasive tools gives a measure of the deformed layer depth. MRF spots revealed the true depth of the grinding-induced deformed surface layer.

Semyon Papernov
Editor

Measured Dependence of Nuclear Burn Region Size on Implosion Parameters in Inertial Confinement Fusion Experiments

Introduction

Images of the nuclear burn regions in inertial confinement fusion (ICF) capsules are important for fully assessing the combined results of all the complicated processes that affect capsule implosion dynamics; these processes, including drive, preheat, instabilities, and mix, must be understood and controlled to achieve ignition and energy generation.[1–3] In the direct-drive approach to ICF, a spherical capsule containing fuel is compressed and heated by direct illumination of laser beams focused on the capsule surface in a nominally uniform fashion.[2] Hydrodynamic instabilities affect the performance of these implosions,[2–10] ultimately determining the size, symmetry, and yield of the nuclear burn region. This article, the third in a series about proton emission imaging,[11–13] presents the first comprehensive studies of D^3He burn region sizes in nominally symmetric direct-drive implosions with diverse capsule and drive conditions. Radial burn profiles and total yields are obtained from measurements of energetic 14.7-MeV protons from the fusion of deuterium (D) and 3-helium (^{3}He) using methods described in Refs. 11 and 12 and in the appendix (see p. 10) of this article. Complementary data from x-ray images,[14–17] proton spectrometers,[18–23] and clean 1-D simulations[24,25] are used in interpreting the burn region sizes and their implications. Asymmetric burn distributions and their relationships to capsule and drive parameters are described in Refs. 11 and 13, and tests of the fidelity of the reconstructed images are discussed in Refs. 11 and 12. Burn images have previously been made of deuterium–tritium-filled capsules using 14.1-MeV neutrons,[8,26–29] 3-MeV protons,[30–32] or 3.5-MeV alpha particles,[32] but for a more limited range of implosion types (see also other papers cited in Ref. 11).

Experimental Conditions (p. 1) describes the drive and capsule parameters studied along with general information about the proton emission imaging cameras and the other diagnostics used. **Data Analysis** (p. 2) provides an overview of the analysis of proton imaging data with examples from two implosions that have dramatically different burn regions. Similarities and differences between nuclear burn images and x-ray images are discussed and important connections between burn profiles, areal density (ρR), and clean 1-D simulations are made. **The Dependence of R_{burn} on Laser and Capsule Parameters** (p. 5) summarizes the results obtained when capsule and drive conditions were systematically varied. The dependence of the burn radius on shell thickness, gas pressure, laser energy, and shell type is investigated for a large set of implosions and evidence of the presence of mix is discussed. **Summary and Discussion** (p. 9) details the results and future work, and the appendix (p. 10) provides detailed information about methods of calculating radial burn profiles from penumbral images (including neutron images).

Experimental Conditions

To explore the range of burn region sizes associated with different kinds of symmetrically driven implosions, and to reveal effects of complicated physics such as preheat, mix, drive efficiency, and core distortions, a wide variety of implosions were examined on the OMEGA Laser System.[33] OMEGA is a 60-beam, frequency-tripled, UV (0.35-μm) laser capable of delivering up to 30 kJ of laser energy in a variety of pulse shapes. The individual laser beams were smoothed with distributed phase plates (DPP's),[34] 2-D smoothing by spectral dispersion with a bandwidth of 1.0 THz,[35,36] and polarization smoothing using birefringent wedges.[37] Two types of DPP's (SG3 and SG4) were used in the experiments described here, producing different beam-intensity profiles.[38] Only 1-ns square laser pulses were used to directly illuminate the capsule. The beam-to-beam energy imbalance was typically less than 4% rms.

The capsules used either 1.8- to 2.3-μm-thick glass (SiO_2) shells filled with 18-atm D^3He gas or 17- to 24-μm-thick plastic (CH) shells filled with 3.6- or 18-atm D^3He gas. The glass-shell implosions used SG3 DPP's while the thick plastic-shell implosions used SG4 DPP's, except where noted. Initial capsule radii were nominally 470 μm for the SG3 DPP's and 430 μm for SG4 DPP's.

Proton core imaging system (PCIS) cameras[11–13] imaged the time-integrated D^3He proton emission distribution from

up to three nearly orthogonal directions simultaneously. These are penumbral imaging cameras, each consisting of a round imaging aperture that is significantly larger than the size of the D^3He burn region and a detector pack comprised of several ranging filters and CR-39 charged-particle detectors.[12,19] The distances from the implosion to the imaging aperture and from the imaging aperture to the detector pack (L_1 and L_2, respectively) determine the geometric magnification $M \equiv L_2/L_1$. Aperture diameters of 600 μm and 2000 μm were used; L_1 was typically 3 cm and M varied from 8 to 20. The energetic protons that pass through the aperture are detected with 100% efficiency in the CR-39 as long as the detector has filtering that slows incoming protons down to the CR-39 sensitivity range of about 0.5 to 8 MeV.

X-ray framing cameras were used to obtain 4- to 5-keV x-ray emission images[14–16] at 58-ps time intervals using 12× magnification and 40-ps integration times. At the time of peak proton production, the x-ray images represent primarily continuum emission from the heated inner portion of the shell material and can be used to estimate the radius of the fuel–shell interface, as described in Ref. 14.

Up to five proton spectrometers[19] were used simultaneously to obtain time-integrated measurements of the D^3He proton spectrum. These spectra are used to determine the total areal density $\langle \rho R \rangle$[19,23,39] using the downshift from the 14.7-MeV birth energy.[18–22,39] In these experiments the measured total ρR comprises both the shell ρR and the fuel ρR, but is usually dominated by the shell.[19,23,39] For given capsule shell and laser conditions, ρR provides a measure of shell convergence since, all else being equal, ρR scales as the inverse of the square of the shell radius at the time of burn. The PCIS and spectrometers typically give the same D^3He yield to within the observed proton-yield asymmetry of 15% to 20% rms.[19]

Data Analysis

1. Finding the Nuclear Burn Radius R_{burn}

The proton emission imaging cameras produce time-integrated penumbral images that are processed to produce either a 2-D image of the burn region surface brightness in D^3He reactions per unit area, $B(r,\phi)$, or a 1-D radial profile of the local number of D^3He reactions per unit volume, $S(r)$, which corresponds to an average over angles. The 2-D analysis technique is extremely useful for studying low-mode deviations from spherical symmetry, and simultaneous views of the burn region from three orthogonal directions can provide measurements of a 3-D structure; this approach has been used to study the important effects of asymmetric laser drive and asymmetric shell structure on implosion symmetry.[13] A disadvantage of 2-D image reconstruction is that it always requires significant smoothing for control of statistical noise, as described in detail in Ref. 11. For the types of implosions studied at OMEGA, D^3He burn region sizes and yields typically require smoothing that limits the 2-D spatial resolution to the range of 15 to 30 μm. If it is desired to make an accurate measurement of characteristic burn region size for nearly symmetric implosions, it is advantageous to use the 1-D approach; it avoids smoothing errors and typically results in statistical measurement uncertainties of a few microns. Since the object of this article is to study burn region size, we will use 1-D analysis here and discuss 2-D results elsewhere.[13]

The 1-D reconstruction approach utilizes the relationship between $S(r)$ and the radial derivative dN/dR of the penumbral image values N (proton tracks per unit area on the detector); dN/dR is equivalent to a set of line integrals through the surface brightness of the D^3He burn region, as discussed in detail in Ref. 11 and in the appendix (p. 10). Of the two 1-D methods described in the appendix, we will use the method of fitting dN/dR with a family of functions that correspond either analytically or numerically to a family of local burn profile shapes.[11] The radial profile $S(r)$ of the proton source in reactions per unit volume is represented by a member of the family of super-Gaussians and sub-Gaussians

$$S(r) = S_0 e^{-(r/r_0)^{2/p}}, \tag{1}$$

where p is a "peakedness" shape parameter and r_0 is a measure of burn radius. The median radius R_{burn} containing half of the total local emission is actually used rather than r_0 to characterize the burn region size because it can be determined much more accurately and is nearly independent of the emission profile shape (see the appendix on p. 10). The burn profile parameters and geometric parameters are then varied to generate the best fit between the measured and predicted dN/dR.

Figure 105.1 shows sample data from two very different implosions involving capsules whose shells are 2-μm-thick glass [Fig. 105.1(a)] and 20-μm-thick plastic [Fig. 105.1(e)]. The plotted data show dN/dR from the azimuthally averaged penumbral images with error bars representing statistical uncertainties. For each data set, a best fit (solid line) was found and used to determine the absolute radial profile of the burn [Figs. 105.1(c) and 105.1(g)] and its characteristic radius R_{burn} as well as the absolute radial profile of surface brightness $B(r)$ [Figs. 105.1(d) and 105.1(h)]. The values of R_{burn} were 29±2.5 μm for the plastic-shell implosion and 54±2 μm for

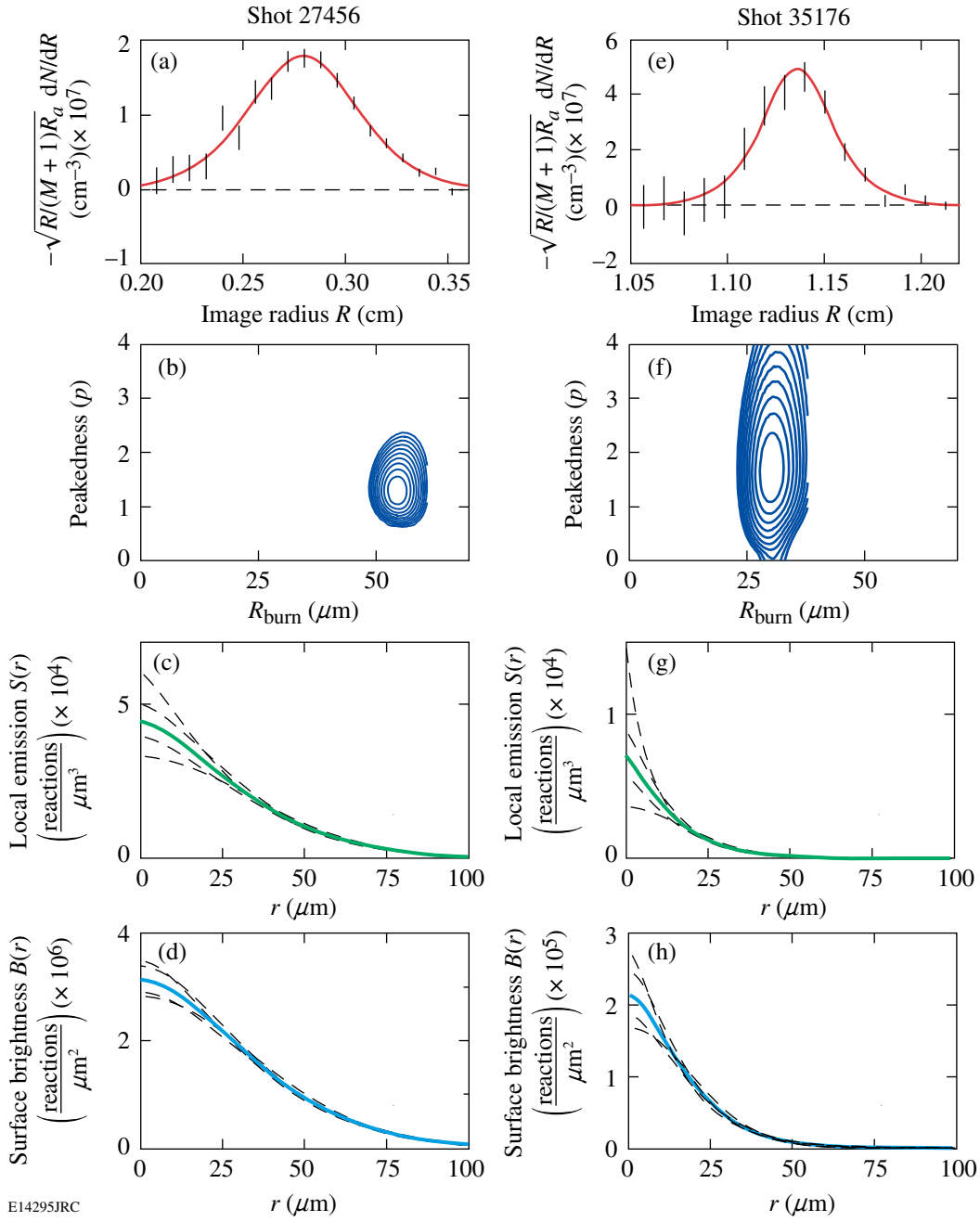

Figure 105.1

Data illustrating the burn region analysis of two very different implosions on OMEGA. The left-hand column corresponds to shot 27456 (2-μm-thick, glass-shell capsule), while the right-hand column corresponds to shot 35176 (20-μm-thick, plastic-shell capsule); each capsule was filled with 18-atm D^3He and irradiated with a 23-kJ, 1-ns laser pulse. The vertical lines in (a) and (e) represent statistical error bars for measured values of dN/dR; the locations of all individual proton tracks on the penumbral image detector are measured to a fraction of a micron, but $N(R)$ needs to be binned with a finite interval in R to achieve acceptable statistics. Note that the significance of the square root appearing as a coefficient dN/dR in the vertical axis labels is discussed in the appendix (p. 10) in connection with Eq. (14); this slowly varying coefficient is very close to 1.0 for the data shown here. The thick lines in (a) and (e) are best fits to the data using the approach described in **Data Analysis** (p. 2) and in the appendix (p. 10). Contour plots showing the total χ^2 as a function of R_{burn} and peakedness p are shown in (b) and (f); the contour levels correspond to $\chi^2_{minimum}+1, \chi^2_{minimum}+2, \ldots$. In (c) and (g) the inferred radial distributions $S(r)$ of D^3He reactions in the burn regions are shown; each thick line corresponds to a best fit while the thin dashed lines show alternate fits resulting in the total χ^2 being larger than the minimum value by 1 (indicating an approximate error envelope for the best-fit profile). The corresponding surface brightness distributions $B(r)$ are shown in (d) and (h). The parameters describing the profiles $S(r)$ are R_{burn} = 54±2 μm and p = 1.35±0.25 (shot 27456) and R_{burn} = 29±2.5 μm and p = 1.7±0.6 (shot 35176).

the glass-shell implosion (where the errors quoted here and throughout reflect statistical uncertainties). As discussed in the appendix (p. 10), the shapes of the radial profiles have their largest uncertainties at $r = 0$ and the values of R_{burn} are determined much more accurately than the shape parameter.

While multiple imaging cameras are generally used to study implosion asymmetry, a single camera provides enough information to calculate a 1-D emission profile of a nominally symmetric capsule implosion. When data from more than one camera were available for an individual implosion studied in this article, the images were analyzed separately and the values of R_{burn} were averaged.

2. Comparing Nuclear Burn Data with X-Ray Data

Since x-ray imaging has been a standard diagnostic technique for decades, it is important to compare x-ray and fusion-burn profiles even though they have very different sensitivities to plasma processes and parameters. They provide valuable and complementary spatial information. The fusion burn profile $S(r)$ represents the time-integrated spatial distribution of the nuclear reaction rate

$$RR = N_D N_{3_{\text{He}}} \langle \sigma v \rangle_{\text{D}^3\text{He}}, \qquad (2)$$

where N_D and $H_{3_{\text{He}}}$ are the D and ^{3}He ion number densities and $\langle \sigma v \rangle$ is the reaction rate for the D^{3}He reaction. In contrast, x-ray images primarily record emissions from heated CH near the fuel–shell interface.[14] In addition, the burn data are time integrated while the x-ray images are gated with a 40-ps window[16] (and show slightly decreasing size during the ~150-ps burn interval). Figure 105.2 provides a comparison between burn data and an x-ray image taken approximately at peak burn time for shot 35176 (analyzed in Fig. 105.1). Although the image of x-ray surface brightness itself [Fig. 105.2(b)] isn't quite symmetric, its azimuthally averaged radial profile allows us to estimate that the fuel–shell interface was located approximately at the radius $R_{\text{xray}} = 32 \pm 5$ μm where the brightness peaks before decreasing with increasing radius.[14] The value of R_{burn} was 29±2.5 μm; considering the different nature of the two kinds of data and the ambiguities as to exactly how they should be compared, the two measurements appear approximately consistent with each other. We will see in **The Dependence of R_{burn} on Laser and Capsule Parameters** (p. 5) that the x-ray and nuclear burn profile data respond in a similar fashion to changes in the experimental conditions for a variety of implosions.

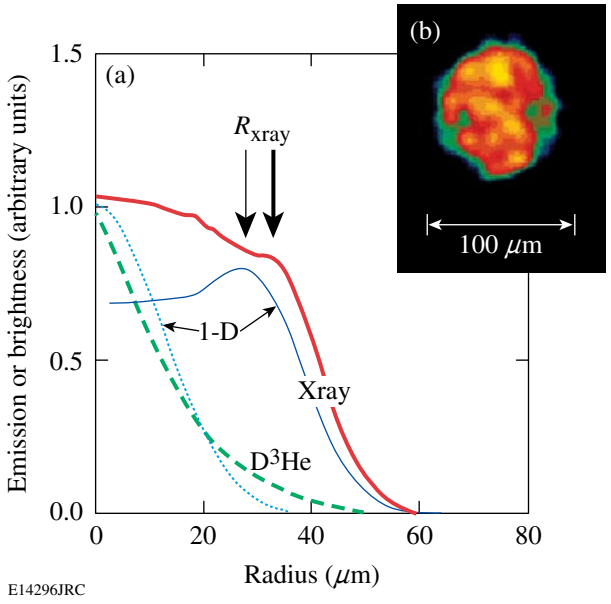

Figure 105.2
Comparison of the measured local D^{3}He emission profile, the measured x-ray surface brightness profile, and 1-D simulations for shot 35176. A 4- to 5-keV x-ray image taken at the peak nuclear burn time (a 40-ps exposure) is shown in (b), and its radial profile is shown in (a) along with a 1-D simulation (solid lines). The D^{3}He burn profile [from Fig. 105.1(g)] is also shown in (a) along with a 1-D simulation (broken lines). In all cases, the measured profiles are thick lines and the 1-D profiles are thin lines. The D^{3}He profiles are arbitrarily normalized to have the same value at $r = 0$.

3. Comparing Nuclear Burn Data and X-Ray Data with 1-D Simulations

The burn data and x-ray data can also be compared to clean 1-D simulations,[24,25] keeping in mind the fact that these simulations don't properly model such important physical processes as fuel–shell mix, preheat, or any type of implosion asymmetry and that they nearly always overestimate the nuclear burn yield.[4] In Fig. 105.2 the measured local burn profile and the measured x-ray surface brightness profile for the plastic-shell implosion 35176 are compared to simulations. The predicted value of R_{xray} is slightly smaller than the measured value (by about 15%). The predicted profile of the D^{3}He burn is quite similar in shape to the measured profile in the core [although the measured shape uncertainty is large there, as shown in Fig. 105.1(g)], but the measured emission values are considerably higher than predicted at larger radii where they contribute heavily to the yield-weighted R_{burn}: the predicted R_{burn} is about 25% smaller than the measured value. On the other hand, there are other indications that the 1-D predictions aren't exactly right: the predicted yield is about 150% higher than the measured value, while the predicted shell

areal density is 26% larger than the measured value (indicating that the shell did not converge radially as much as predicted). It will be seen in **The Dependence of R_{burn} on Laser and Capsule Parameters** (p. 5) that measured values of R_{burn} are uniformly larger than simulated values for the CH-shell implosions studied here but that the measured and predicted values agree fairly well for a wide range of glass-shell implosions (which have different implosion dynamics[40]). Possible explanations of this measurement/simulation discrepancy in terms of either systematic measurement errors (of which we have no evidence[41]) or effects not included in 1-D simulations (mix, preheat, and hydrodynamic instabilities) are considered in **Summary and Discussion** (p. 9).

The Dependence of R_{burn} on Laser and Capsule Parameters

Correlations between R_{burn} and the capsule and drive conditions allow an elucidation of some basic implosion dynamics. Systematic studies that examine the dependence of R_{burn} on laser drive energy, capsule shell material and thicknesses, capsule fill pressure, and DPP type are presented here. These external parameters are often strongly correlated with one or more fundamental quantities or processes such as ion temperature, capsule convergence, fuel density, and fuel–shell mix. For that reason, attempts were made to change only one external parameter at a time in experiments whenever possible.

1. Laser Energy

Figure 105.3(a) shows the effect of increasing laser energy for 1-ns square pulses when irradiating thin glass-shell capsules. As the energy was increased from 6 kJ to 23 kJ, R_{burn} increased from about 35 μm to 80 μm. For capsules with 19- to 20-μm CH shells and 18-atm D^3He fills, R_{burn} was about 30 μm; data are not yet available for illustrating variations with laser energy. The change in yield-weighted ion temperature $\langle T_{ion} \rangle$ [42] probably dominates the change in R_{burn} for the glass-shell capsules, as illustrated in Fig. 105.3(b) where the data of Fig. 105.3(a) are replotted as a function of $\langle T_{ion} \rangle$. Increases in $\langle T_{ion} \rangle$ should result in a larger R_{burn} since the D^3He reactivity is extremely sensitive to the ion temperature. Figure 105.3(c) replots the data of Fig. 105.3(a) with the corresponding R_{burn} values from 1-D simulations. For the glass shells, 1-D simulations agree fairly well with R_{burn} measurements and show the same variation with laser energy; for the plastic shells, the 1-D values are uniformly lower than the measured R_{burn} values.

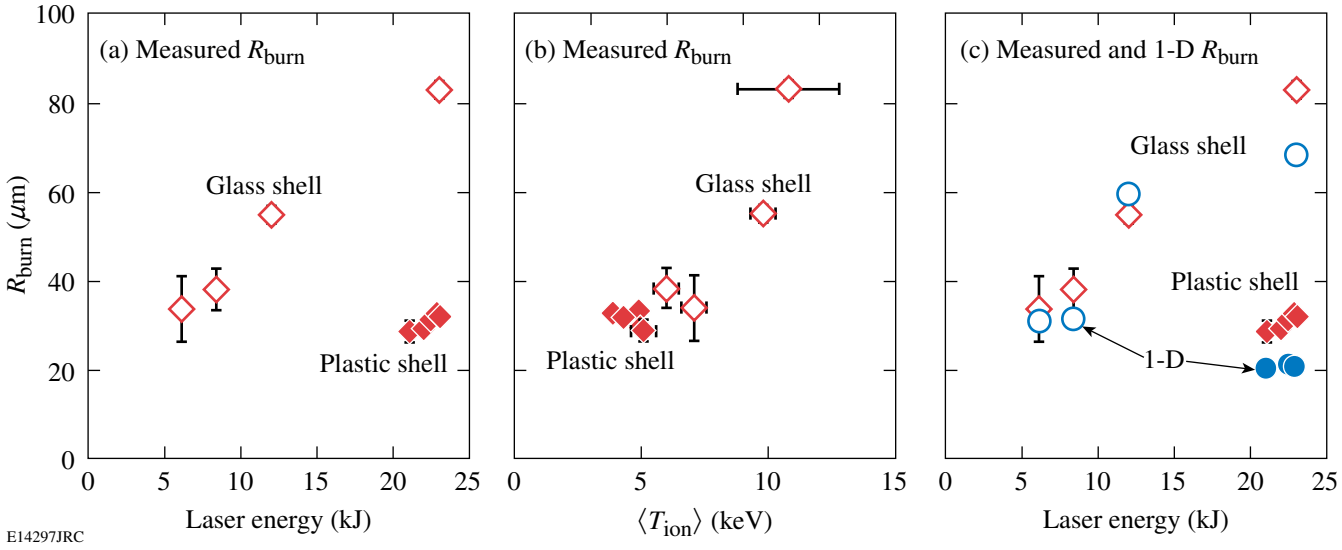

Figure 105.3
(a) Data showing the relationship of burn region size to laser energy for implosions of capsules with an 18-atm D^3He fill and either 20-μm plastic or 2-μm glass shells. For the thin-glass-shell, exploding-pusher implosions (open diamonds), increasing the laser energy results in a dramatically larger D^3He burn region radius. For the thick-CH-shell, compressive implosions, $R_{burn} \approx 30$ μm for 23-kJ laser energy (solid diamonds), but data are not currently available for lower laser energies. The ion temperature was strongly correlated with R_{burn}, as shown in (b) where R_{burn} has been plotted versus the burn-averaged ion temperature $\langle T_{ion} \rangle$ obtained with neutron time-of-flight systems. (c) Comparison of R_{burn} measurements with values from 1-D simulations (circles).

2. Capsule Fill Pressure

The effects of fill pressure changes on R_{burn} for CH-shell implosions were studied systematically. Figure 105.4(a) shows R_{burn} plotted as a function of measured $\langle \rho R \rangle$ for fill pressures of 3.6 atm and 18 atm. R_{burn} is consistently larger for the higher fill pressure. Figure 105.4(b) shows the averages of the measured values[43] for all implosions of each fill pressure in Fig. 105.4(a); the plotted values are

$$\langle R_{burn}\,(18\text{ atm})\rangle = 30.6 \pm 0.3\ \mu\text{m} \tag{3}$$

and

$$\langle R_{burn}\,(3.6\text{ atm})\rangle = 24.8 \pm 0.8\ \mu\text{m}, \tag{4}$$

where the quoted errors reflect only the statistical uncertainties and do not include any other possible systematic errors. Figure 105.4(b) also shows corresponding values of R_{xray} for which we have data. The same trend is seen in both R_{burn} and R_{xray}. Figure 105.4(c) compares values of R_{burn} and $\langle \rho R \rangle$ from 1-D simulations (solid circles for 18 atm and open circles for 3.6 atm) to the data. While the measured R_{burn} values are all larger than predicted (as for all other plastic-shell implosions studied here), there are other important differences between simulations and measurements. The 1-D simulations predict that a reduction in fill pressure from 18 atm to 3.6 atm should result in a large increase in ρR (by ~93%) due to increased radial convergence of the shell material accompanied by a substantial decrease in R_{burn} (by ~40%) largely due to a corresponding decrease in the core size. In contrast, the data indicate a much smaller increase in ρR (by ~13%), implying little change in radial convergence of the bulk of the shell material and a moderate decrease in R_{burn} (by ~20%).

These results agree quite well with data and interpretations published by C. K. Li *et al.*[4] for implosions of plastic-shell capsules with DT fills of various pressures. For laser conditions and shell thicknesses similar to those examined here, it was concluded that the experimental radial convergence increased only slightly when the pressure was reduced from ~18 to 3 atm, in distinct contrast to 1-D calculations, exactly as seen here; it was suggested that the failure to achieve higher radial shell convergence with a low fill pressure was probably due to the fuel–shell mix, which converts some of the kinetic energy of radial shell movement to lateral motion. This is also consistent with the present data, which show a significant reduction in measured R_{burn} when the pressure was decreased in spite of little change in the compressed shell radius; if the radius of most of the shell is held fixed, cooling and dilution of the outer fuel region due to the mixing in of a small amount of cooler shell

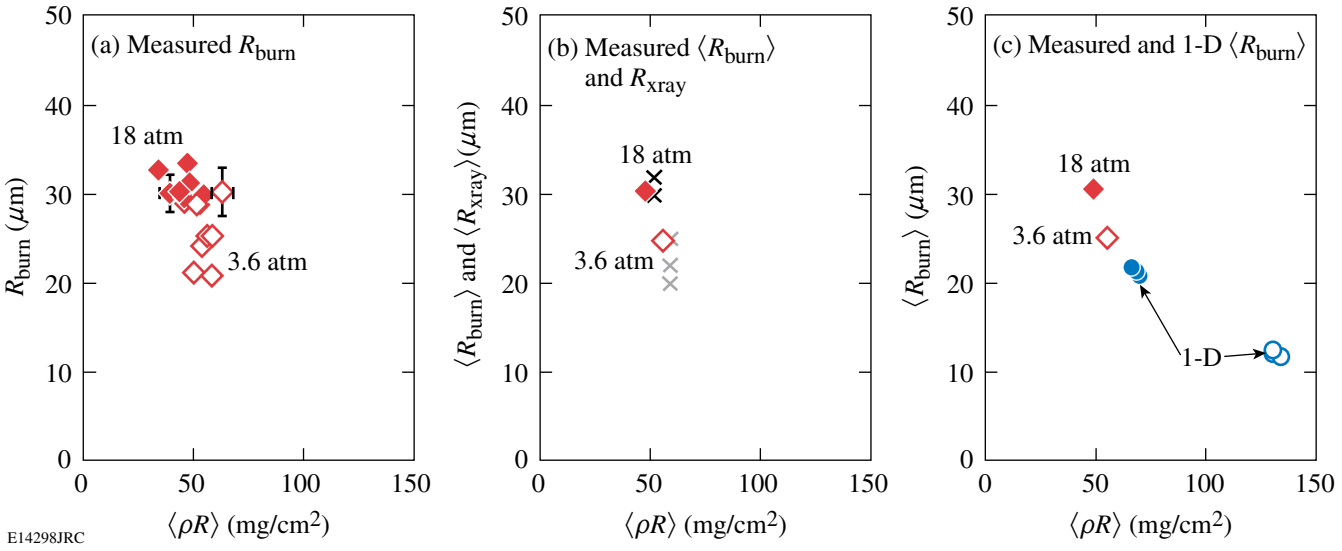

Figure 105.4

(a) A significant difference in the D^3He burn size is shown for 18-atm (solid diamonds) and 3.6-atm (open diamonds) fill pressures in implosions of D^3He-filled capsules with 19- to 20-μm plastic shells. R_{burn} is plotted as a function of the areal density $\langle \rho R \rangle$ measured from proton energy downshifts. (b) The averages of data in (a) are displayed with fuel–shell interface estimates (R_{xray}) for 18-atm (black ×'s) and 3.6-atm (gray ×'s) implosions, demonstrating agreement in the trends of both R_{burn} and R_{xray}. (c) When the average data are displayed with the 1-D calculated R_{burn} (circles), the same trend is present but the simulations predict lower R_{burn} values overall and a much larger increase in ρR with decreased fill pressure.

material would reduce the number of D^3He reactions there and reduce R_{burn}. The 1-D simulations predict a much larger decrease in R_{burn} at a lower fill pressure without invoking mix, but this is because they predict a much larger increase in radial convergence than is measured.

Finally, it seems plausible that the increased scatter of R_{burn} at lower pressures may reflect decreased stability for those implosions. As shown in Fig. 105.4(a), the standard deviation in the 3.6-atm data is larger than that for the 18-atm data (by the ratio of 3.6 μm to 1.4 μm).

3. Distributed Phase Plates

An important goal of the OMEGA program is to improve the single and overlapping beam uniformity of the laser. As a step in that direction, the older SG3 DPP's were recently replaced with SG4 DPP's that result in a flatter on-target beam intensity [$\propto e^{-(r/353\ \mu\text{m})^{4.1}}$, where r is radius from beam center, rather than $e^{-(r/308\ \mu\text{m})^{2.2}}$ with the SG3 DPP].[38] To adjust for a reduction in the new spot size, the capsule radii were also reduced from ~470 to 430 μm. Figure 105.5 shows the effect of these changes on R_{burn} for several shots, plotted as a function of ρR. R_{burn} is larger for the SG3 data than for the SG4 data. The average measurement values[43] of all implosions shown in Fig. 105.5(a) are

$$\langle R_{burn}\,(\text{SG3})\rangle = 37.1\pm0.8\ \mu\text{m} \tag{5}$$

and

$$\langle R_{burn}\,(\text{SG4})\rangle = 30.5\pm0.3\ \mu\text{m} \tag{6}$$

and are plotted in Fig. 105.5(b). The fact that convergence, determined from ρR,[4] is about the same for the SG3 and SG4 implosions, suggests that the reduction in R_{burn} for the SG4 DPP is largely a consequence of the smaller initial capsule radius (this is consistent with other measurements,[44] indicating that changing from SG3 DPP's to SG4 DPP's brought no significant improvement in overall implosion performance for capsules with 20-μm CH shells and 18-atm fills). The values of R_{xray} show the same kind of variation with DPP type as the values of R_{burn}, as shown in Fig. 105.5(b).[45] The 1-D R_{burn} simulations [Fig. 105.5(c), open circles for SG3 and solid circles for SG4] don't show as large a change with DPP type as the measured R_{burn} or R_{xray}. An interesting question to address would be whether the SG4 DPP reduces the scatter in 3.6-atm

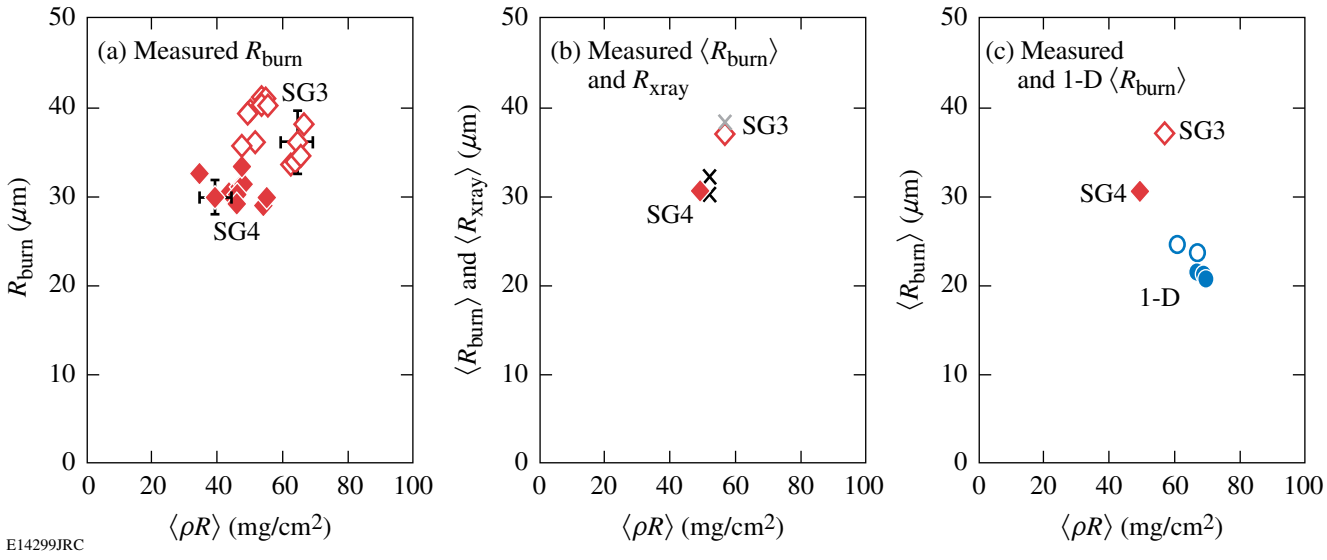

Figure 105.5
(a) Consistently smaller burn radii are produced with SG4 phase plates and targets (solid diamonds) than with SG3 DPP's (open diamonds). R_{burn} is plotted as a function of the measured areal density ρR for implosions of capsules with 19- to 20-μm-thick plastic shells and 18-atm D^3He fill. (b) The averages of burn radii data in (a) are displayed with fuel–shell interface estimates (R_{xray}) from SG3 (gray ×) and SG4 (black ×) implosions,[44] demonstrating agreement in the trends of R_{burn} and R_{xray}. (c) When the average R_{burn} data are displayed with the 1-D values (circles) the same trend is present but the simulations predict lower R_{burn} values and a smaller change in R_{burn} with the change in phase plates. The reduction in R_{burn} with the change from SG3 to SG4 DPP's seems largely dominated by the reduction in initial capsule radius from ~470 to 430 μm.

capsule performance that was discussed in connection with Fig. 105.4, but comparative data are currently unavailable.

4. Capsule Shell Thickness

The shell thickness is known to have an effect upon mix and convergence.[4–9,10] Figure 105.6(a) shows the effect on R_{burn} (diamonds). The trend of these data is more fully revealed by averaging the data over capsules with similar shell thicknesses [Fig. 105.6(b)]. As illustrated, R_{burn} increases slowly as the shell thickness increases from 17 to 24 μm with the values

$$\langle R_{burn}\,(17\ \mu\text{m})\rangle = 29.1\pm0.4\ \mu\text{m}, \tag{7}$$

$$\langle R_{burn}\,(20\ \mu\text{m})\rangle = 30.5\pm0.5\ \mu\text{m, and} \tag{8}$$

$$\langle R_{burn}\,(24\ \mu\text{m})\rangle = 32.8\pm1.1\ \mu\text{m}. \tag{9}$$

The convergence for the thicker-shell capsules was slightly smaller, as reflected in the fact that the ρR's of those capsules are about the same [Fig. 105.6(c)];[4] the larger burn radii for the thicker 24-μm capsules reflect the smaller convergence. R_{xray}, also plotted in Fig. 105.6(b), shows a similar trend. R_{burn} for 1-D simulations shows the same trend [triangles, Fig. 105.6(d)], but the absolute value, as remarked earlier, is significantly smaller.

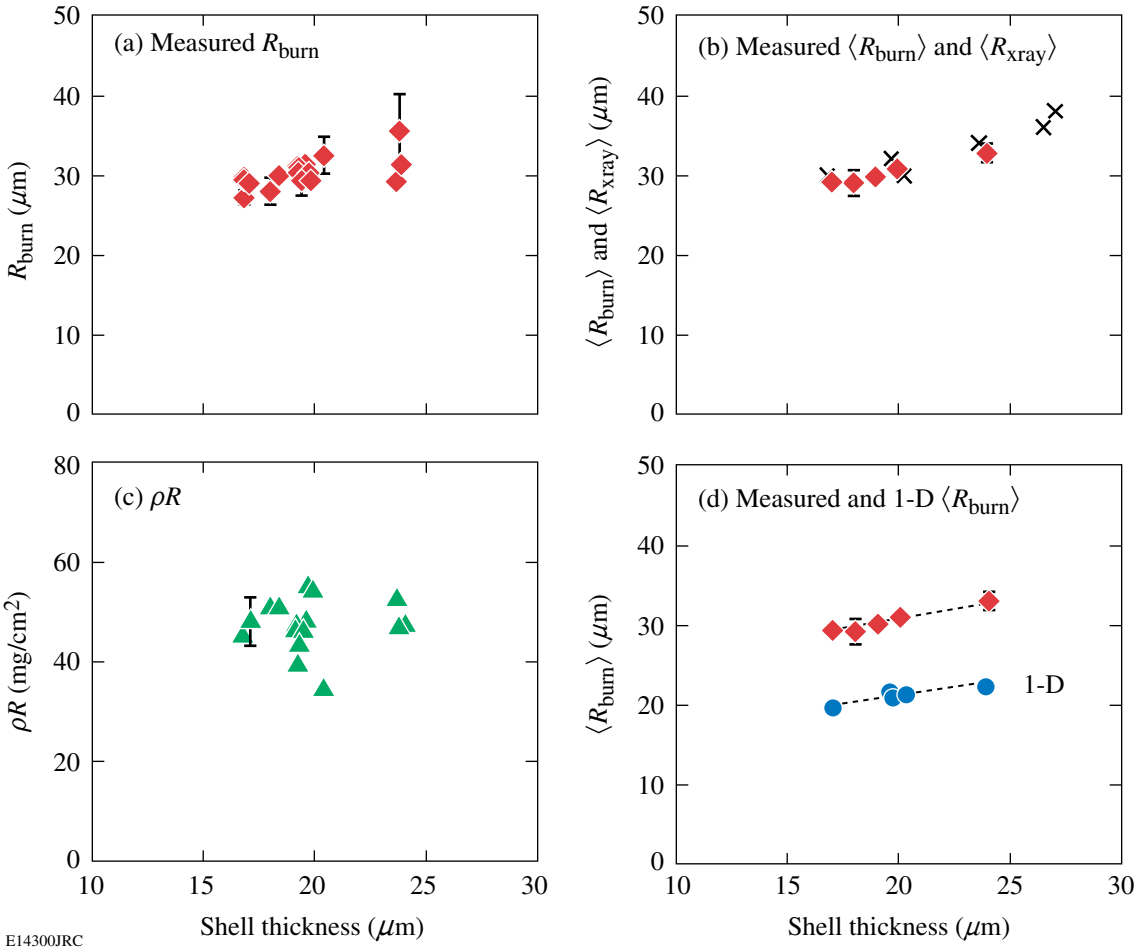

Figure 105.6
(a) The dependence of R_{burn} on plastic shell thickness provides information about mix and convergence.[2–10] (b) The trend is more obvious when the R_{burn} data for similar capsule thicknesses are averaged (diamonds). The fuel–shell interface estimates [R_{xray} (×'s)] for these implosions and others demonstrate virtually the same trend. (c) The areal densities ρR measured for the same implosions were only weakly dependent on shell thickness. (d) Predicted values of R_{burn} from 1-D simulations (circles) show the same trend as the measurements but lower values.

Summary and Discussion

In summary, we have described methods for measuring nuclear burn region sizes and presented the first measurements for a wide range of direct-drive implosion conditions, identifying systematic changes in burn region size due to changes in laser conditions and fuel capsule parameters. These measurements complement our related studies demonstrating systematic relationships between drive asymmetry, shell asymmetry, and burn asymmetry.[11,13] Collectively, this work demonstrates the practicality and usefulness of emission imaging of nuclear burn, which directly reveals the spatial distributions of the fusion reactions that are the end result of all physical processes affecting capsule implosions.

Starting with laser drive conditions, it was shown that the burn radius in capsules with thin (~2-μm) glass shells and 18-atm fills varies strongly with total laser energy, going from ~35 μm at 6 kJ to 80 μm at 23 kJ (all with 1-ns square pulses). Most measurements to date for capsules with plastic shells have been at 23 kJ, so no conclusions were drawn here about energy variations (but future experiments may investigate this). Measurements also indicated that changing from the SG3 DPP's to the SG4 DPP's for 20-μm CH shells and 18-atm fills didn't significantly change shell convergence but did result in a somewhat smaller R_{burn} that may simply reflect the smaller initial shell radius; this is consistent with other measurements,[44] indicating that changing from SG3 DPP's to SG4 DPP's brought no significant improvement in overall implosion performance for such capsules. Data for comparing R_{burn} for SG3 DPP's and SG4 DPP's with 3.6-atm fill pressures are currently unavailable.

Looking next at capsule structure, it was seen that increasing the CH shell thickness from 17 to 24 μm for 18-atm fills resulted in the burn radius increasing from 30 μm to 33 μm, a modest change largely attributed to the slightly smaller convergence of the more massive, thicker shell capsules. Measurements have not yet been made for glass capsules with different shell thicknesses, but capsules with 2-μm glass shells have burn radii 2.5 times larger than capsules with 20-μm CH shells with equal laser energy (23 kJ) and fill pressures (18 atm). It was also demonstrated that reducing the D^3He fill pressure from 18 to 3.6 atm in 20-μm CH shells resulted in little change in shell convergence but a significant change in burn radius (from 31 μm to 25 μm), a reduction largely attributed to increased fuel–shell mix for the more unstable 3.6-atm implosions. These data and interpretations are consistent with previous measurements of fuel ρR versus gas pressure in implosions of DT-filled capsules,[4] and we anticipate that more experiments and comparisons with simulations will be devoted to studying and quantifying the effects of mix.

The burn data were compared with x-ray images, which have a long history with ICF and therefore provide a very important point of comparison. As discussed in the text, x-ray images and burn images reflect different aspects of the compressed capsules and there is considerable ambiguity about how they should be compared and interpreted; the x-rays are most sensitive to CH from the inner part of the shell that is in contact with, or mixed into, the hot fuel. What was found is that the characteristic radius R_{xray}, calculated as described in Ref. 14 and thought to be an indication of the inner boundary of hot CH, is usually comparable to the characteristic burn radius R_{burn}, which represents the median burn radius. There is, therefore, usually a radial overlap between the apparent burn region and the apparent inner CH location. This overlap may represent a region of atomic mix or a region where fingers of shell material extend into the fuel region, although interpretation of the x-ray images in the presence of mix is beyond the scope of this article. A crucial fact about all of the data displayed here is that wherever R_{xray} and R_{burn} measurements are available for comparison [Figs. 105.4(b), 105.5(b), and 105.6(b)], they are comparable to each other and changes in one are tracked almost precisely by changes in the other. This is a strong independent confirmation that changes in burn region size measurements reflect true changes in the compressed capsule structure.

The burn data and x-ray data were both compared with predictions of 1-D simulations. It was found that while the 1-D burn radii were similar to the measured radii for capsules with thin glass shells [Fig. 105.3(c)], the predicted burn radii for capsules with 20-μm CH shells are smaller than the measured values by about 30% for an 18-atm fill and 50% for a 3.6-atm fill (and the measured R_{xray} was also larger than predicted for the 18-atm fill). These discrepancies are qualitatively consistent with the discrepancies between predicted and measured values of areal density, which show that shell convergence is lower than predicted for all CH-shell capsules studied. The dependence on fill pressure suggests that mix or instabilities could be a contributing factor. For a given amount of radial shell convergence, mix would be expected to make the burn region smaller by cooling the outer fuel regions, but we saw in **Capsule Fill Pressure** (p. 6) that the convergence is very much smaller than predicted for lower fill pressures, probably because of mix. In addition, mix is known to truncate the burn in time, leading to a higher-than-predicted average radius during the burn interval. Another possible explanation for the simulation/measurement difference is preheat, which

results in reduced compression due to increased pressure. For the glass-shell implosions, on the other hand, the roles of mix, hydrodynamic instabilities, and preheat are expected to be substantially smaller at burn time in glass-shell implosions than in CH-shell implosions,[40] and this could account for the closer agreement between simulation and data found in all such cases. In the future we hope to see if 2-D and 3-D simulations come closer to predicting the measured average shell convergence and measured burn region size. A thorough search for systematic errors that could lead to artificially broadened burn image data has been made, but no sources of error that could be large enough to account for the discrepancy in burn radii for CH shells have yet been identified.[12,41]

Comparisons of our D^3He burn profiles with DT and DD burn profiles now being obtained by Disdier *et al.* on OMEGA with important new neutron imaging techniques[46] for hydrodynamically similar DT- and D_2-filled capsules are now being pursued and will be reported in the future. These comparisons could provide a test of consistency of the different burn imaging methods and could potentially provide information about ion temperature profiles (through the local ratios of reaction rates).

ACKNOWLEDGMENT

The authors express their gratitude to the OMEGA engineers and operations crew who supported these experiments. In addition, we would like to personally thank Michael Canavan, Candice Culligan, and Jocelyn Schaeffer for their continuous help. This work has been supported in part by LLE (Subcontract No. 412160-001G) and LLNL (Subcontract No. B543881), and by the U.S. Department of Energy Office of Inertial Confinement Fusion (Grant No. DE-FG03-03NA00058) and under Cooperative Agreement No. DE-FC52-92SF19460, the University of Rochester, and New York State Energy Research and Development Authority.

Appendix: Notes on Determining Radial Burn Profiles from Penumbral Images

As described in Ref. 11, it is possible to determine the radial profile $S(r)$ of nuclear reactions in a burn region assumed spherically symmetric by analyzing a penumbral image made using reaction products. The details of the approach used in this article are slightly different from what is described in Ref. 11, and we discuss them here, along with alternative approaches and sample analyses. We start with the idealized assumption that the imaging aperture has a perfectly defined hard edge; a penumbral image of a point source would be uniform within a circular area and zero outside. This assumption is not warranted for the imaging of DT burn with DT neutrons, but it was shown in Ref. 12 that it should be sufficiently accurate for imaging D^3He burn with D^3He protons. A few protons will scatter off the edge of the aperture, but their scattering angle is sufficiently large that they contribute only a small, relatively flat penumbral image background that disappears when the radial derivative is taken for analysis. In **Generalization to Apertures Without "Hard Edges" and Neutron Imaging** (p. 14), we discuss how this limitation can be removed either for neutron images or for small corrections with proton images if the effects of the aperture edge can be characterized.

1. The Problem

The surface brightness of the spherically symmetric burn region is

$$B(r) = \int_{-\infty}^{\infty} S\left(\sqrt{r^2 + \ell^2}\right) d\ell. \tag{10}$$

A penumbral image made with a hard-edged, round aperture of radius R_a is azimuthally symmetric with a radial profile $N(R)$ of detected protons per unit area, where R is the radius measured with respect to the center of the image. The radial derivative of this image can be written

$$\left.\frac{dN}{dR}\right|_{R = R_d + Mx} = -\frac{1}{4\pi M\left(L_1 + L_2\right)^2} P_c(x), \tag{11}$$

where

$$P_c(x) = R_d \int_{-\pi}^{\pi} B\left[\sqrt{x^2 + 2R_c\left(R_c + x\right)\left(1 - \cos\theta\right)}\right] \cos\theta \, d\theta. \tag{12}$$

In Eq. (11), L_1 and L_2 are the source–aperture and aperture–detector distances, $M = L_2/L_1$ is the geometric magnification of the penumbral camera, and $R_d \equiv (M + 1)R_a$ is the radius of the aperture image at the detector. In Eq. (12), $R_c = R_a(M + 1)/M$ is the radius of the aperture's projection at the location of the burn region, as seen from the detector, and the angle θ is measured relative to the center of this projection. As discussed in Ref. 11, $P_c(x)$ is a set of integrals through the surface brightness of the burn region along parallel paths that are curved but become straight in the limit $R_{\text{burn}}/R_c << 1$;

$$P_c(x) \xrightarrow{R_{\text{burn}}/R_a \to 0} P(x) = \int_{-\infty}^{\infty} B\left(\sqrt{x^2 + \ell^2}\right) d\ell. \tag{13}$$

$P_c(x)$ can be thought of as a 1-D projection of the surface brightness $B(r)$.

$P_c(x)$ can be obtained experimentally from dN/dR through Eq. (11) and, if $R_{\text{burn}}/R_c << 1$, it can be used to obtain $B(r)$

through Abel inversion. Similarly, $B(r)$ can be Abel inverted to obtain the source profile $S(r)$. If R_{burn}/R_c is not negligible, then the straight-line integral $P(x)$ can be calculated approximately from $P_c(x)$ before the Abel inversion process;[47]

$$P(x) \cong \sqrt{1 + x/R_c}\, P_c(x) = -4\pi M\left(L_1 + L_2\right)^2 \sqrt{\frac{R}{R_d}}\,\frac{dN}{dR}\bigg|_{R = R_d + Mx}. \tag{14}$$

A simple analytic solution for direct calculation of the double Abel inversion relating $S(r)$ to $P(x)$ was described in Ref. 48 in connection with a different application (imaging of a spherically symmetric source with a linear slit aperture);

$$S(r) = -\frac{1}{2\pi r}\frac{dP(x)}{dx}\bigg|_{x = r}. \tag{15}$$

Equation (15) works well for perfect data (no noise or other distortions, infinitesimal sampling width, and $R_{\text{burn}}/R_c << 1$), but it isn't ideal for the data discussed in this article, even though the data generally satisfy the condition $R_{\text{burn}}/R_c << 1$ for several reasons. First, the statistics aren't good enough even after the data are binned [see the caption of Fig. 105.1(a)] except for the high-yield glass-shell capsules. Second, it becomes inaccurate when the data are binned, since this is equivalent to imposing a finite sampling width and results in artificial broadening of the inferred $S(r)$ and smoothing of any feature that is not much larger than the sampling width.[49] Finally, it has a problem at $r = 0$ where, even if $P(0) \equiv 0$, any noise or measurement uncertainty in the data near $r = 0$ translates into uncertainties in S that become infinite as $r \to 0$ [this is not a defect in Eq. (15), but a consequence of the fact that the central emissivity value applies to a small volume and has very little effect on line integrals through the surface brightness]. Nevertheless, the direct method works away from $r = 0$ if statistics allow and its application to the current data are illustrated in **Direct Calculation of $S(r)$** (p. 13).

2. Inferring $S(r)$ from Least-Squares Fits

As with many Abel inversion applications, the statistics issue can be improved by fitting the raw data with analytic functions that automatically smooth out some of the statistical fluctuations in $P(x)$ and simultaneously enforce reasonable behavior at the singular point $r = 0$. In Ref. 11, we proposed the use of powers of parabolas to represent $S(r)$ because these map analytically to other powers of parabolas for $P(x)$; the experimental $P(x)$ can be fit to powers of a parabola and $S(r)$ found analytically. This makes possible a range of profile shapes for $S(r)$ varying from hollow to peaked, with the limiting peaked shape being a Gaussian when the power goes to infinity, and works well because many of the data sets analyzed are statistically consistent with a Gaussian shape for $S(r)$. With many data sets there were indications that slightly better fits might be achieved with a profile more peaked than Gaussian, however, so here we take a different approach that has several advantages.

Instead of using a set of functions to fit to $P(x)$ and analytically deducing $S(r)$ using Eq. (15), we start by representing $S(r)$ by the family of super- and sub-Gaussians

$$S(r) = S_0 e^{-\left(r/r_0\right)^{2/p}}, \tag{16}$$

where r_0 is the "1/e" radius and p is the "peakedness" of the emission profile ($p = 0$ is flat, $p = 1$ is Gaussian, and $p > 1$ is more centrally peaked than Gaussian). From a given trial function $S(r)$, the functions $B(r)$, $P_c(x)$, and dN/dR can be calculated numerically using Eqs. (10), (12), and (11). For comparison with experimental data, the predicted dN/dR must then be convolved with a boxcar function to model the actual binning used in tabulating the measured data. To determine the most probable profile $S(r)$, the parameters R_d, S_0, p, and r_0 are varied and the values leading to a minimum χ^2 fit of predicted to measured dN/dR are determined along with their statistical uncertainties.[50] The deduced $S(r)$ can then be described by S_0 (or by the total yield), p, and r_0 though, as shown below, it turns out to be more useful to parameterize the radial size by the mean yield-weighted burn radius $\langle r\rangle_s = \int rS(r)r^2dr \Big/ \int S(r)r^2dr$ or by the median burn radius $r_{S,\text{median}}$ containing half the yield rather than by r_0.

Figure 105.7 illustrates sample shapes of $S(r)$ with corresponding functions $B(r)$ and $P(x)$. We see immediately that small differences in the shape of $P(x)$ translate into much larger differences in the shape of $S(r)$, which is characteristic of inversion procedures. This means that finite errors in the raw data are amplified into much larger errors in the shape of $S(r)$, particularly for small r, though it will turn out that errors in the characteristic radius are not amplified by the inversion process.

Figure 105.8 illustrates what happens when this technique is applied to the measured dN/dR data shown in Figs. 105.1(a) and 105.1(e). Figures 105.8(a) and 105.8(d) show contour plots of total χ^2 versus p and r_0 (using the values of R_c and S_0 that minimize χ^2 at every point). In each case there is a well-defined location

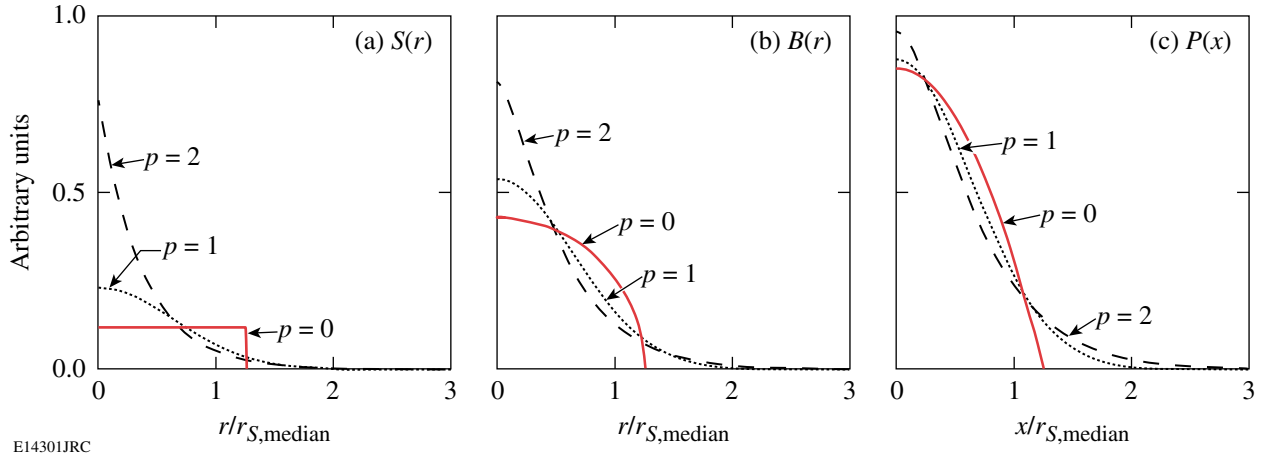

Figure 105.7
(a) $S(r)$ from Eq. (11) for $p = 0$, 1, and 2, normalized so that each curve has the same total yield. As discussed in the text, $r_{S,\text{median}}$ is the median radius (containing half the yield). (b) The corresponding curve for $B(r)$. (c) $P(x)$ for the case of no data binning. Note that hollow profiles of $S(r)$ can easily be added to this family of functions.

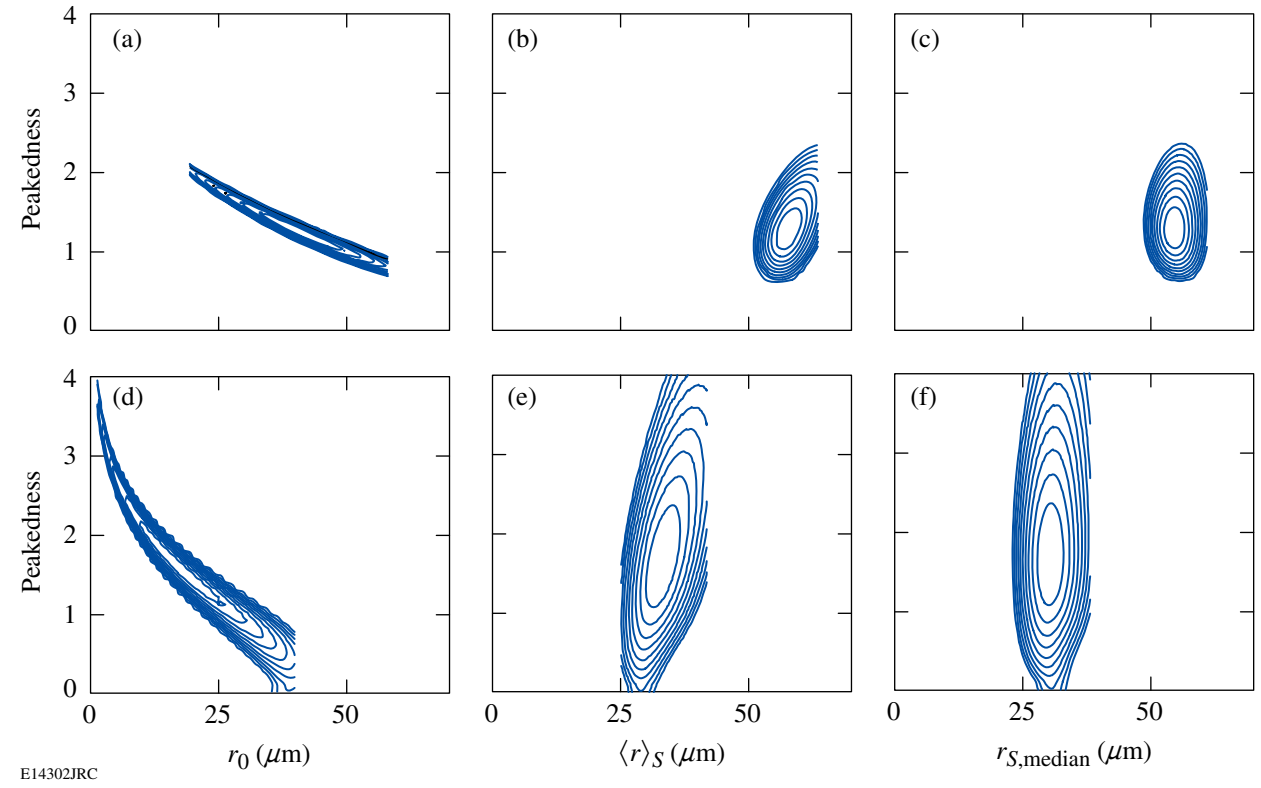

Figure 105.8
Contours of total χ^2 for fits to two real data sets as a function of the shape parameter p and either the $1/e$ radius r_0, $\langle r \rangle_S$, or $r_{S,\text{median}}$. The upper three plots correspond to shot 27456, while the lower plots correspond to shot 35176. In each case, the contour levels correspond to $\chi^2_{\text{minimum}} + 1, \chi^2_{\text{minimum}} + 2, \ldots$.

corresponding to the best fit (lowest χ^2). Figures 105.8(b) and 105.8(e) show the same contours parameterized by $\langle r\rangle_S$ rather than r_0, and Figs. 105.8(c) and 105.8(f) show parameterization by $r_{S,\text{median}}$. Notice that either $\langle r\rangle_S$ or $r_{S,\text{median}}$ is much more independent of the peakedness parameter p than r_0; the same conclusion has been reached using a wide range of functional forms for $S(r)$ and a wide range of data sets. The problem with r_0 is that a change in the central value of $S(r)$ changes the $1/e$ radius but has little effect on $P(x)$. In general, $r_{S,\text{median}}$ seems slightly better than $\langle r\rangle_S$, so henceforth we will define the characteristic burn radius R_{burn} to be $r_{S,\text{median}}$. Notice also that the percent statistical uncertainty in p is much larger than the uncertainty in R_{burn}. This is because errors in radial size do not get amplified in the inversion process, as can be shown analytically using Eq. (15) for the case $R_{\text{burn}}/R_a << 1$. The mean burn radius $\langle r\rangle_S$ is always exactly twice the average radius of $P(x)$; $\langle r\rangle_P \equiv \int xP(x)dx \Big/ \int P(x)dx = 0.5\langle r\rangle_S$, regardless of the shape of $S(r)$. This means that a fractional error in $\langle r\rangle_P$ results in the same fractional error in $\langle r\rangle_S$. A similar result holds for the median radius ($r_{P,\text{median}} = 0.44\ r_{S,\text{median}}$).

Figures 105.1(c), 105.1(g), 105.1(d), and 105.1(h) show the radial profiles of $S(r)$ and $B(r)$ corresponding to the same data and fits with uncertainties deduced from the fitting procedure. The largest uncertainties in $S(r)$ and $B(r)$ are at the center, and the uncertainties get larger with each level of inversion. The large uncertainties at $r = 0$ simply reflect the fact that the central emissivity has very little effect on penumbral images.

The family of functions represented by Eq. (16) doesn't extend to hollow profiles, but can easily be extended in that direction through the use of different functions. In addition, more complicated radial profiles using series expansions (e.g., of Chebyshev polynomials) can be used if statistics allow. But if yields are high enough, the direct calculation of $S(r)$ becomes practical.

3. Direct Calculation of $S(r)$

Subject to the conditions discussed in **The Problem** (p. 10), Eq. (15) allows direct calculation of $S(r)$ from $P(x)$ calculated with Eq. (14). Figure 105.9 shows how this works out for the two implosions analyzed above. This approach requires knowledge of R_d; for the calculations illustrated in Fig. 105.9, the values of R_d inferred from the fitting method were used. In each case the binning width was made as small as possible, consistent with the counting statistics. Shot 27456 has a high enough proton yield (~2×10^{10}) to make this method work for $r \gtrsim R_{\text{burn}}/3$; as r is reduced, the calculated values start to fall because of the effects of binning near the central peak, and as r approaches 0 the result is completely unreliable because of the singularity in Eq. (15). The yield is much lower for shot 37156 (~4×10^8), so the statistical errors on the calculated values of $S(r)$

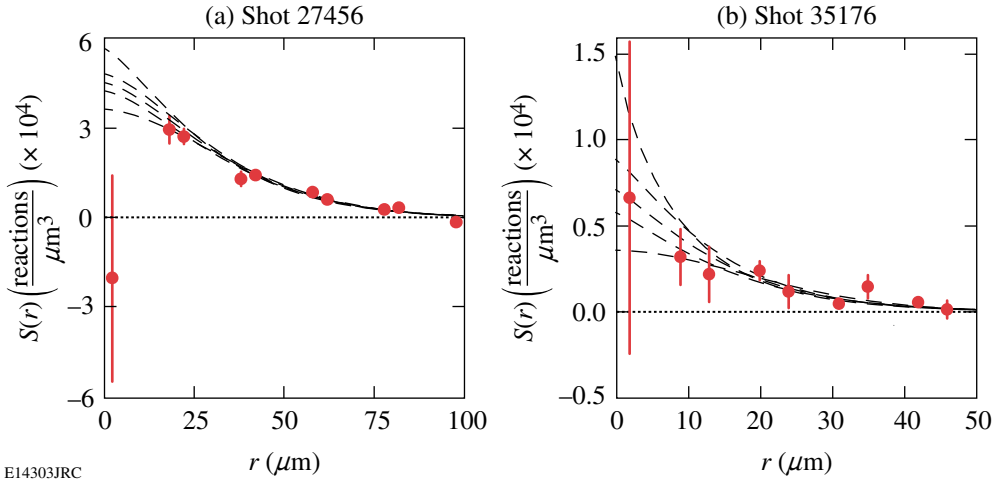

Figure 105.9
Results of applying the direct inversion method to data from shots (a) 27456 and (b) 35176. The plotted data points with error bars result from the application of Eq. (14) to the dN/dR data shown in Figs. 105.1(a) and 105.1(e); the data were binned slightly differently [with radial bins at the detector equivalent to bins in the burn region of 20 μm for (a) and 11 μm for (b), the effective ratios of bin width to R_{burn} were 0.37 and 0.41, respectively]. The uneven spacing of the data points reflects the fact that values of $S(r)$ were calculated from $P(x)$ for both positive and negative x, and S values at negative r values were reflected to positive r. The thin dashed lines correspond to the profiles shown in Figs. 105.1(d) and 105.1(h), including the error envelope.

are much larger and the shape of $S(r)$ is somewhat ill defined. The calculated value near $r = 0$ happened to be about right, but this was partly a matter of luck; changing the binning resulted in erratic values.

4. Generalization to Apertures Without "Hard Edges" and Neutron Imaging

If a penumbral-imaging aperture has a perfect, opaque edge, then the radial derivative dN/dR of a penumbral image of a point source will be a delta function. If not, and if dN/dR for a point source can be either calculated or measured, then it can be incorporated directly into the method described in **Inferring $S(r)$ from Least-Squares Fits** (p. 11). Before comparison with measured values of dN/dR, each predicted function calculated from a trial function $S(r)$ through Eqs. (10), (12), and (11) need only be convolved by an appropriate smearing function F before being convolved by the boxcar function that models the data binning. $F(R')$ is simply dN/dR for a point source evaluated at $R = R_d + R'$ and normalized to have unit integral. If the direct-calculation method is to be used instead of the least-squares fitting method, then the data must be deconvolved to remove the effect of F.

REFERENCES

1. J. Nuckolls *et al.*, Nature **239**, 139 (1972).
2. J. D. Lindl, *Inertial Confinement Fusion: The Quest for Ignition and Energy Gain Using Indirect Drive* (Springer-Verlag, New York, 1998).
3. S. Atzeni and J. Meyer-ter-Vehn, *The Physics of Inertial Fusion: Beam Plasma Interaction, Hydrodynamics, Hot Dense Matter*, International Series of Monographs on Physics (Clarendon Press, Oxford, 2004).
4. C. K. Li, F. H. Séguin, J. A. Frenje, S. Kurebayashi, R. D. Petrasso, D. D. Meyerhofer, J. M. Soures, J. A. Delettrez, V. Yu. Glebov, P. B. Radha, F. J. Marshall, S. P. Regan, S. Roberts, T. C. Sangster, and C. Stoeckl, Phys. Rev. Lett. **89**, 165002 (2002).
5. D. D. Meyerhofer, J. A. Delettrez, R. Epstein, V. Yu. Glebov, V. N. Goncharov, R. L. Keck, R. L. McCrory, P. W. McKenty, F. J. Marshall, P. B. Radha, S. P. Regan, S. Roberts, W. Seka, S. Skupsky, V. A. Smalyuk, C. Sorce, C. Stoeckl, J. M. Soures, R. P. J. Town, B. Yaakobi, J. D. Zuegel, J. Frenje, C. K. Li, R. D. Petrasso, D. G. Hicks, F. H. Séguin, K. Fletcher, S. Padalino, M. R. Freeman, N. Izumi, R. Lerche, T. W. Phillips, and T. C. Sangster, Phys. Plasmas **8**, 2251 (2001).
6. P. B. Radha, J. Delettrez, R. Epstein, V. Yu. Glebov, R. Keck, R. L. McCrory, P. McKenty, D. D. Meyerhofer, F. Marshall, S. P. Regan, S. Roberts, T. C. Sangster, W. Seka, S. Skupsky, V. Smalyuk, C. Sorce, C. Stoeckl, J. Soures, R. P. J. Town, B. Yaakobi, J. Frenje, C. K. Li, R. Petrasso, F. Séguin, K. Fletcher, S. Padalino, C. Freeman, N. Izumi, R. Lerche, and T. W. Phillips, Phys. Plasmas **9**, 2208 (2002).
7. S. P. Regan, J. A. Delettrez, F. J. Marshall, J. M. Soures, V. A. Smalyuk, B. Yaakobi, V. Yu. Glebov, P. A. Jaanimagi, D. D. Meyerhofer, P. B. Radha, W. Seka, S. Skupsky, C. Stoeckl, R. P. J. Town, D. A. Haynes, Jr., I. E. Golovkin, C. F. Hooper, Jr., J. A. Frenje, C. K. Li, R. D. Petrasso, and F. H. Séguin, Phys. Rev. Lett. **89**, 085003 (2002).
8. C. R. Christensen, D. C. Wilson, C. W. Barnes, G. P. Grim, G. L. Morgan, M. D. Wilke, F. J. Marshall, V. Yu. Glebov, and C. Stoeckl, Phys. Plasmas **11**, 2771 (2004).
9. D. C. Wilson, C. W. Cranfill, C. Christensen, R. A. Forster, R. R. Peterson, H. M. Hoffman, G. D. Pollak, C. K. Li, F. H. Séguin, J. A. Frenje, R. D. Petrasso, P. W. McKenty, F. J. Marshall, V. Yu. Glebov, C. Stoeckl, G. J. Schmid, N. Izumi, and P. Amendt, Phys. Plasmas **11**, 2723 (2004).
10. P. B. Radha, V. N. Goncharov, T. J. B. Collins, J. A. Delettrez, Y. Elbaz, V. Yu. Glebov, R. L. Keck, D. E. Keller, J. P. Knauer, J. A. Marozas, F. J. Marshall, P. W. McKenty, D. D. Meyerhofer, S. P. Regan, T. C. Sangster, D. Shvarts, S. Skupsky, Y. Srebro, R. P. J. Town, and C. Stoeckl, Phys. Plasmas **12**, 032702 (2005).
11. F. H. Séguin, J. L. DeCiantis, J. A. Frenje, S. Kurebayashi, C. K. Li, J. R. Rygg, C. Chen, V. Berube, B. E. Schwartz, R. D. Petrasso, V. A. Smalyuk, F. J. Marshall, J. P. Knauer, J. A. Delettrez, P. W. McKenty, D. D. Meyerhofer, S. Roberts, T. C. Sangster, K. Mikaelian, and H. S. Park, Rev. Sci. Instrum. **75**, 3520 (2004).
12. J. L. DeCiantis, F. H. Séguin, J. A. Frenje, V. Berube, M. J. Canavan, C. D. Chen, S. Kurebayashi, C. K. Li, J. R. Rygg, B. E. Schwartz, R. D. Petrasso, J. A. Delettrez, S. P. Regan, V. A. Smalyuk, J. P. Knauer, F. J. Marshall, D. D. Meyerhofer, S. Roberts, T. C. Sangster, C. Stoeckl, K. Mikaelian, H. S. Park, and H. F. Robey, "Proton Core Imaging of the Nuclear Burn in Inertial Confinement Fusion Implosions," to be published in Review of Scientific Instruments (see also LLE Review Quarterly Report **104**, p. 197).
13. F. H. Séguin, J. L. DeCiantis, J. A. Frenje, C. K. Li, J. R. Rygg, C. D. Chen, R. D. Petrasso, V. A. Smalyuk, F. J. Marshall, J. A. Delettrez, J. P. Knauer, P. W. McKenty, D. D. Meyerhofer, S. Roberts, T. C. Sangster, H. S. Mikaelian, and H. S. Park, Bull. Am. Phys. Soc. **49**, 63 (2004); *ibid.* "Measured Effects of Drive Asymmetry and Shell Asymmetry on Nuclear Burn Region Symmetry in Direct-Drive ICF implosions," to be submitted to Physics of Plasmas.
14. S. P. Regan, J. A. Delettrez, R. Epstein, P. A. Jaanimagi, B. Yaakobi, V. A. Smalyuk, F. J. Marshall, D. D. Meyerhofer, W. Seka, D. A. Haynes, Jr., I. E. Golovkin, and C. F. Hooper, Jr., Phys. Plasmas **9**, 1357 (2002).
15. D. Ress *et al.*, Rev. Sci. Instrum. **66**, 579 (1995).
16. V. A. Smalyuk, T. R. Boehly, L. S. Iwan, T. J. Kessler, J. P. Knauer, F. J. Marshall, D. D. Meyerhofer, C. Stoeckl, B. Yaakobi, and D. K. Bradley, Rev. Sci. Instrum. **72**, 635 (2001).
17. F. J. Marshall, J. A. Delettrez, R. Epstein, V. Yu. Glebov, D. R. Harding, P. W. McKenty, D. D. Meyerhofer, P. B. Radha, W. Seka, S. Skupsky,

V. A. Smalyuk, J. M. Soures, C. Stoeckl, R. P. Town, B. Yaakobi, C. K. Li, F. H. Séguin, D. G. Hicks, and R. D. Petrasso, Phys. Plasmas **7**, 2108 (2000).

18. F. H. Séguin, C. K. Li, J. A. Frenje, S. Kurebayashi, R. D. Petrasso, F. J. Marshall, D. D. Meyerhofer, J. M. Soures, T. C. Sangster, C. Stoeckl, J. A. Delettrez, P. B. Radha, V. A. Smalyuk, and S. Roberts, Phys. Plasmas **9**, 3558 (2002).

19. F. H. Séguin, J. A. Frenje, C. K. Li, D. G. Hicks, S. Kurebayashi, J. R. Rygg, B.-E. Schwartz, R. D. Petrasso, S. Roberts, J. M. Soures, D. D. Meyerhofer, T. C. Sangster, J. P. Knauer, C. Sorce, V. Yu. Glebov, C. Stoeckl, T. W. Phillips, R. J. Leeper, K. Fletcher, and S. Padalino, Rev. Sci. Instrum. **74**, 975 (2003).

20. F. H. Séguin, C. K. Li, D. G. Hicks, J. A. Frenje, K. M. Green, R. D. Petrasso, J. M. Soures, D. D. Meyerhofer, V. Yu. Glebov, C. Stoeckl, P. B. Radha, S. Roberts, C. Sorce, T. C. Sangster, M. D. Cable, S. Padalino, and K. Fletcher, Phys. Plasmas **9**, 2725 (2002).

21. C. K. Li, F. H. Séguin, J. A. Frenje, R. D. Petrasso, R. Rygg, S. Kurebayashi, B. Schwartz, R. L. Keck, J. A. Delettrez, J. M. Soures, P. W. McKenty, V. N. Goncharov, J. P. Knauer, F. J. Marshall, D. D. Meyerhofer, P. B. Radha, S. P. Regan, T. C. Sangster, W. Seka, and C. Stoeckl, Phys. Plasmas **10**, 1919 (2003).

22. R. D. Petrasso, J. A. Frenje, C. K. Li, F. H. Séguin, J. R. Rygg, B. E. Schwartz, S. Kurebayashi, P. B. Radha, C. Stoeckl, J. M. Soures, J. Delettrez, V. Yu. Glebov, D. D. Meyerhofer, and T. C. Sangster, Phys. Rev. Lett. **90**, 095002 (2003).

23. C. K. Li, D. G. Hicks, F. H. Séguin, J. A. Frenje, R. D. Petrasso, J. M. Soures, P. B. Radha, V. Yu. Glebov, C. Stoeckl, D. R. Harding, J. P. Knauer, R. L. Kremens, F. J. Marshall, D. D. Meyerhofer, S. Skupsky, S. Roberts, C. Sorce, T. C. Sangster, T. W. Phillips, M. D. Cable, and R. J. Leeper, Phys. Plasmas **7**, 2578 (2000).

24. M. C. Richardson, P. W. McKenty, F. J. Marshall, C. P. Verdon, J. M. Soures, R. L. McCrory, O. Barnouin, R. S. Craxton, J. Delettrez, R. L. Hutchison, P. A. Jaanimagi, R. Keck, T. Kessler, H. Kim, S. A. Letzring, D. M. Roback, W. Seka, S. Skupsky, B. Yaakobi, S. M. Lane, and S. Prussin, in *Laser Interaction and Related Plasma Phenomena*, edited by H. Hora and G. H. Miley (Plenum Publishing, New York, 1986), Vol. 7, pp. 421–448.

25. J. Delettrez, R. Epstein, M. C. Richardson, P. A. Jaanimagi, and B. L. Henke, Phys. Rev. A **36**, 3926 (1987).

26. K. A. Nugent and B. Luther-Davies, J. Appl. Phys. **58**, 2508 (1985).

27. D. Ress *et al.*, Rev. Sci. Instrum. **59**, 1694 (1988).

28. R. A. Lerche *et al.*, Laser Part. Beams **9**, 99 (1991).

29. L. Disdier, R. A. Lerche, J. L. Bourgade, and V. Yu. Glebov, Rev. Sci. Instrum. **75**, 2134 (2004).

30. Y.-W. Chen *et al.*, Opt. Commun. **73**, 337 (1989).

31. M. Nakai *et al.*, Rev. Sci. Instrum. **61**, 3235 (1990).

32. A. P. Fews *et al.*, Phys. Rev. Lett. **73**, 1801 (1994).

33. T. R. Boehly, D. L. Brown, R. S. Craxton, R. L. Keck, J. P. Knauer, J. H. Kelly, T. J. Kessler, S. A. Kumpan, S. J. Loucks, S. A. Letzring, F. J. Marshall, R. L. McCrory, S. F. B. Morse, W. Seka, J. M. Soures, and C. P. Verdon, Opt. Commun. **133**, 495 (1997).

34. Y. Lin, T. J. Kessler, and G. N. Lawrence, Opt. Lett. **20**, 764 (1995).

35. S. Skupsky, R. W. Short, T. Kessler, R. S. Craxton, S. Letzring, and J. M. Soures, J. Appl. Phys. **66**, 3456 (1989).

36. S. P. Regan, J. A. Marozas, R. S. Craxton, J. H. Kelly, W. R. Donaldson, P. A. Jaanimagi, D. Jacobs-Perkins, R. L. Keck, T. J. Kessler, D. D. Meyerhofer, T. C. Sangster, W. Seka, V. A. Smalyuk, S. Skupsky, and J. D. Zuegel, J. Opt. Soc. Am. B **22**, 998 (2005).

37. T. R. Boehly, V. A. Smalyuk, D. D. Meyerhofer, J. P. Knauer, D. K. Bradley, R. S. Craxton, M. J. Guardalben, S. Skupsky, and T. J. Kessler, J. Appl. Phys. **85**, 3444 (1999).

38. R. A. Forties and F. J. Marshall, Rev. Sci. Instrum. **76**, 073505 (2005).

39. C. K. Li, F. H. Séguin, D. G. Hicks, J. A. Frenje, K. M. Green, S. Kurebayashi, R. D. Petrasso, D. D. Meyerhofer, J. M. Soures, V. Yu. Glebov, R. L. Keck, P. B. Radha, S. Roberts, W. Seka, S. Skupsky, C. Stoeckl, and T. C. Sangster, Phys. Plasmas **8**, 4902 (2001).

40. M. D. Rosen and J. H. Nuckolls, Phys. Fluids **22**, 1393 (1979).

41. Calculations showed insignificant image broadening associated with proton scattering in the capsule, aperture, and detector filters, while experiments showed no indication of different results with different aperture size or magnification. Neither experiments nor simulations revealed any serious field effects.[12]

42. V. Yu. Glebov, C. Stoeckl, T. C. Sangster, S. Roberts, G. J. Schmid, R. A. Lerche, and M. J. Moran, Rev. Sci. Instrum. **75**, 3559 (2004).

43. The plotted R_{burn} and $\langle \rho R \rangle$ results for individual implosions already represent a mean value of the measurements obtained from that implosion; there were as many as six measurements of R_{burn}[12] and five of ρR for each implosion. When the mean value is calculated for an implosion type, all these measurements are weighted equally.

44. S. P. Regan, J. A. Delettrez, V. Yu. Glebov, V. N. Goncharov, J. A. Marozas, F. J. Marshall, P. W. McKenty, D. D. Meyerhofer, P. B. Radha, T. C. Sangster, V. A. Smalyuk, C. Stoeckl, J. A. Frenje, C. K. Li, R. D. Petrasso, and F. H. Séguin, Bull. Am. Phys. Soc **49**, 62 (2004).

45. The SG3 R_{xray} data point was taken from a hydrodynamically equivalent 15-atm, D_2 gas-fill implosion (shot 22546).[7] The substitution is reasonable; similar R_{xray} results are obtained from D_2 and D^3He gas implosions (J. L. DeCiantis, "Proton Emission Imaging of the Nuclear Burn in Inertial Confinement Fusion Experiments," M.S. thesis, Massachusetts Institute of Technology, 2005).

46. L. Disdier, A. Rouyer, I. Lantuejoul, O. Landuas, J. L. Bourgade, T. C. Sangster, V. Yu. Glebov, and R. A. Lerche, "Inertial Confinement Fusion Neutron Images," to be published in Physics of Plasmas.

47. The correction factor $\sqrt{1 + x/R_c} = \sqrt{R/R_d}$ in Eq. (14) can be found by calculating the integrals for a circular disk with uniform surface brightness and keeping the lowest-order terms. Since any radial profile of surface brightness can be made up from a superposition of disks, the result is independent of radial profile. This is a better correction than that shown in Eq. (7) of Ref. 11, which was found empirically. In any case, the correction is too small to be important for the data considered here.

48. C. M. Vest and D. G. Steel, Opt. Lett. **3**, 54 (1978).

49. M. M. Mueller, Opt. Lett. **4**, 351 (1979).

50. The parameter R_d is the radius on the detector corresponding to the center of the penumbra. In principle, this value is known in advance from the dimensions of the imaging system, but it must be known very accurately, and including it as a fit parameter allows for the possibility of small errors in camera positioning. Two more parameters that need to be known are the coordinates of the center of the penumbral image. This is found by doing a simplified version of the analysis described in the text, but varying the assumed center coordinates and finding the values that give the smallest burn radius (since any displacement from the true center broadens the average penumbra and the inferred burn radius).

Rayleigh–Taylor Growth Measurements of 3-D Modulations in a Nonlinear Regime

Introduction

Rayleigh–Taylor (RT)[1,2] instability is of critical importance in inertial confinement fusion (ICF)[3] and astrophysics.[4] In ICF, the RT instability leads to shell disruption and performance degradation of spherically imploding targets.[3] In astrophysics, when a star becomes a supernova, the outer shell is pushed by the inner exploding core and heavy material from the inner core appears in the outer shell because of the RT mixing process.[4] In the linear regime of classical RT instability,[3,5] small initial modulations grow exponentially in time with the growth rate $\gamma = (Akg)^{0.5}$, where k is the modulation wave number, g is the target acceleration, and A is the Atwood number defined as $A = (\rho_h - \rho_l)/(\rho_h + \rho_l)$, where ρ_h and ρ_l are the densities of heavy and light fluids, respectively. Most ICF-related cases involve ablative drive in which the growth rate $\gamma = \alpha(kg)^{0.5} - \beta k V_a$ is stabilized by the ablation term $\beta k V_a$, where V_a is the ablation velocity and α and β are constants.[6,7] This growth rate is an approximation of a more exact formula in Ref. 7. The growth rates of linear RT instability have been measured in both classical[5] and ablative regimes.[8–12] The indication of nonlinearity in RT growth in real space is that the modulations develop into bubbles (penetration of the lighter fluid into the heavier) and spikes (penetration of the heavier fluid into the lighter).[13] In Fourier space, this is equivalent to the harmonics generation of initial fundamental spatial modes. As the RT instability further progresses, the two fluids mix in turbulent and chaotic regimes.[14–17] There are two modeling approaches for nonlinear RT instability: a modal one[18–20] that describes the evolution in Fourier space and a bubble competition and merger that describes instability in real space.[17,21–24] In Fourier space, Haan's model[18] [see Fig. 105.10(a)] predicts that the spectral amplitudes of 3-D, broadband modulations grow exponentially with the RT growth rates of $\gamma(k)$ until they reach the saturation levels[18,25] $S_k = 2/Lk^2$ (L is the size of the analysis

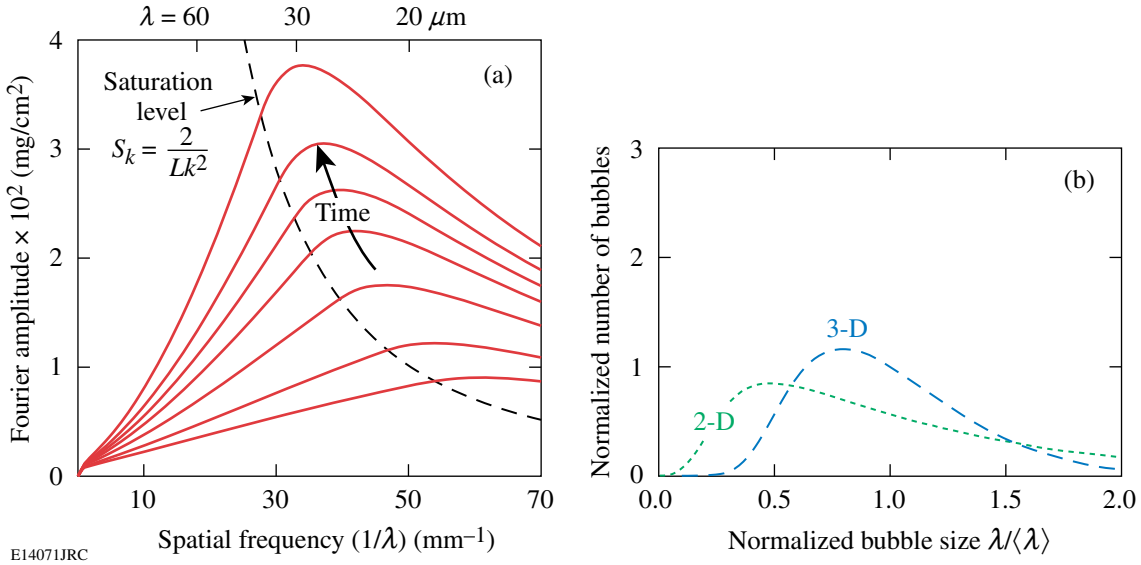

Figure 105.10
(a) Fourier spectra of target areal-density modulations driven by Rayleigh–Taylor instability, as predicted by Haan's model.[18] The dashed line is Haan's saturation level $S_k = 2/Lk^2$ (L = 400 μm is the size of analysis box) multiplied by the calculated target density to be converted to areal density.[25] (b) Bubble size distributions as a function of the bubble size normalized to the average bubble size $\lambda/\langle\lambda\rangle$ as predicted by 2-D (dotted curve) and 3-D (dashed curve) bubble competition models in a self-similar regime.[27]

box), after which they grow linearly in time with the saturation velocities[18,26] $V_s(k) = S_k\gamma(k)$. The short-wavelength modes grow initially most rapidly and quickly saturate at levels S_k while very long-wavelength modes grow more slowly. As a result, the midwavelength modes have the largest growth factors, producing a peak in the spectrum. As the evolution continues, this peak moves to longer wavelengths, as shown in Fig. 105.10(a). Haan's model applies in the weakly nonlinear regime for broadband modulation amplitudes around the saturation levels.[25] In real space, bubble competition models predict that smaller bubbles (with smaller nonlinear velocities) are taken over by larger bubbles (with higher nonlinear velocities) through bubble competition and the bubble merger processes.[17,21–24] As a result, the average size of the modulations shifts to longer wavelengths as the modulations grow. The real-space models predict that the bubble sizes and amplitudes evolve with a self-similar behavior in an advanced nonlinear regime.[24,27,28] The self-similar behavior predicts that the distribution function $f(\lambda/\langle\lambda\rangle)$ of the bubble size normalized to the average bubble size $\lambda/\langle\lambda\rangle$ is constant as the modulation average size and average amplitude grow.[24,27,28] Figure 105.10(b) shows self-similar bubble size distributions predicted by 2-D and 3-D bubble competition models.[24,27] It should be noted here that Haan's model is applicable for broadband initial spectra, which can contain both long and short wavelengths. The bubble competition model is mainly applicable for initial spectra dominated by short wavelengths, whereas long wavelengths are mainly produced by bubble merger processes.[27] This article presents results of nonlinear RT experiments[25,26,28,29] performed over several years on the OMEGA Laser System[30] and shows new results in which planar targets were directly driven by laser light and 3-D broadband modulation growth was measured near nonlinear saturation levels. The initial broadband modulations were dominated by short wavelengths in these experiments; therefore, both real-space (bubble) and Fourier-space models can be used for comparison with experimental data. This article compares measured RT evolution with that predicted by both Fourier- and real-space nonlinear RT models. The experiments with initial broadband modulations dominated by long-wavelengths modes are described elsewhere.[26]

In this article, **Experimental Configuration** (p. 18) describes the experimental configuration and measurement technique. **Experimental Results** are discussed on p. 19 and **Conclusions** are presented on p. 24.

Experimental Configuration

In the experiments, initially smooth, 1-mm-diam CH targets with thicknesses ranging from 20 to 50 μm were driven with 12-ns and 3-ns square pulses at laser intensities of ~5 × 10^{13} W/cm^2 and ~2 × 10^{14} W/cm^2, respectively, on the OMEGA Laser System.[30] The modulation growth was measured with through-foil, x-ray radiography.[29] The backlighter x rays that probe target modulations were imaged by an 8-μm pinhole array onto a framing camera, allowing up to eight images with a temporal resolution of ~80 ps and a spatial resolution of ~10 μm to be captured at different times in each shot.[29] The initial target modulations, used for RT growth measurements, were imprinted by laser-beam nonuniformities created by using standard distributed phase plates[31] (SG8 DPP's) during the first several hundred picoseconds of the drive. Figure 105.11 shows a measured equivalent-target-plane image of the laser beam with the DPP [Fig. 105.11(a)] along with its Fourier spectrum [Fig. 105.11(b)]. The beam with DPP has broadband modulations with spatial frequencies up to ~320 mm^{-1}, corresponding to the smallest spatial size of ~3 μm and an intensity

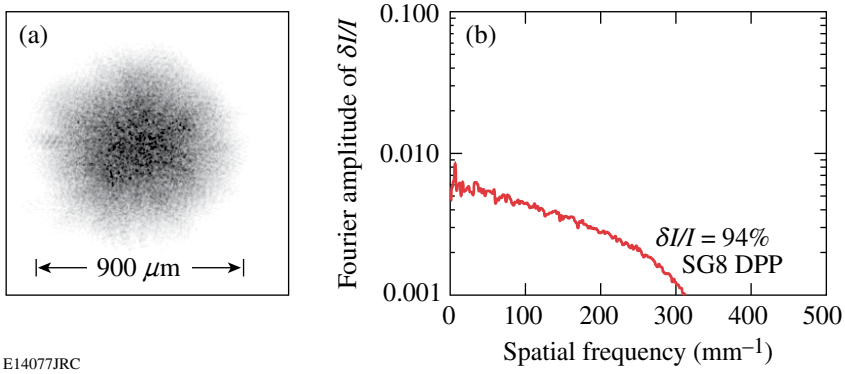

Figure 105.11
(a) The equivalent-target-plane image of the laser beam with a distributed phase plate (SG8 DPP). (b) Fourier spectrum of relative intensity [$\delta I/I$] modulations of the laser beam with a SG8 DPP. The smallest size of intensity modulations in the beam is ~3 μm and it has an intensity modulation σ_{rms} of ~94%.

modulation σ_{rms} of ~94%. The amplitudes of target modulations $a_t(k)$ are proportional to the amplitudes of relative laser modulations[32,33] $a_l(k)$, $a_t(k) = E(k)a_l(k)$, where $E(k) \sim 1/k$ is the imprint efficiency.[33–35] Some experiments used smoothing by spectral dispersion (SSD)[36] and polarization smoothing (PS)[37] to vary the spectrum of target modulations to study the dependence of the RT growth on the initial conditions. Polarization smoothing reduces the modulations of most laser spatial frequencies by a factor[37] of $\sqrt{2}$, while SSD reduces high-spatial frequency modulations more strongly than the low-spatial frequency modulations.[36]

The typical optical-depth (OD) images (obtained by taking a natural logarithm of intensity-converted, framing-camera images) of x-ray radiographs are shown in Fig. 105.12 for an experiment with a 20-μm-thick target driven with a 3-ns square pulse shape.[29] A Weiner filter (based on measured system resolution and noise) was applied to these images to remove noise and deconvolve the system's modulation transfer function to recover target OD modulations.[29] The measured target OD variations are proportional to the variations of target areal density $\delta[\rho R]$; $\delta[\mathrm{OD}(t)] = \mu_{CH}(E)\delta[\rho R(t)]$, where $\mu_{CH}(E)$ is the CH target mass absorption rate at x-ray energy E used for backlighting and t is the time of the measurement. The areal-density $\delta[\rho R(t)]$ modulations were obtained by dividing measured OD modulations by target mass absorption rates. The RT growth of the initial nonuniformities was analyzed in the central parts (with a box size of up to 400 μm) of these images where the average drive is uniform.

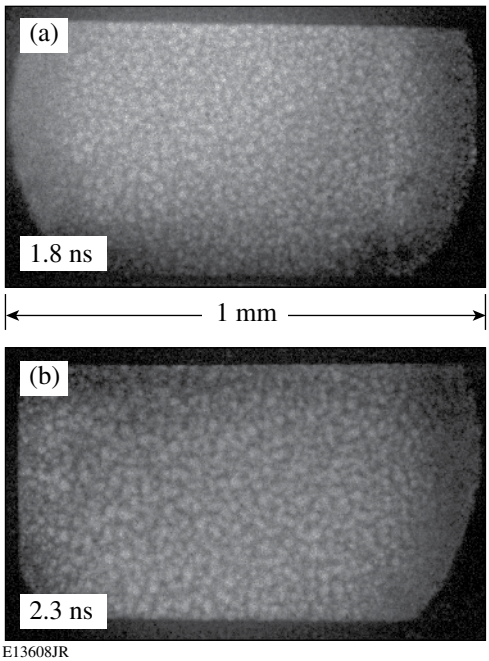

Figure 105.12
X-ray framing-camera images of RT growth modulations measured at (a) 1.8 and (b) 2.3 ns in a 20-μm-thick target driven by a 3-ns laser pulse at an intensity of ~2×10^{14} W/cm^2. Central, 400-μm-square parts of the images were taken for analysis.

As laser light is applied to the target, the pressure created by the target ablation launches a shock wave that compresses the target.[35] Any nonuniformities in the laser drive are imprinted into the target modulations at this time.[32–35] When the shock front reaches the rear surface of the target, it sends the rarefaction wave back to the ablation surface; shortly thereafter, the target begins to accelerate (in these experiments after around 0.5 to 1 ns, depending on target thickness). During the acceleration phase, the ablation-surface modulations grow exponentially because of Rayleigh–Taylor instability.[1–3] At later times these modulations become detectable with our diagnostics as their evolution enters the nonlinear regime. [25,26,28,29]

Experimental Results

Figure 105.13 shows the Fourier spectra of growing target areal-density modulations $\delta[\rho R(t)]$ measured in 20-μm-thick targets [Figs. 105.13(a) and 105.13(b)] and a 40-μm-thick target [Fig. 105.13(c)] driven with a 3-ns square laser drive pulse at an intensity of ~2×10^{14} W/cm^2 (Refs. 25 and 29). The smoothing conditions included DDP's, SSD, and PS on a shot shown in Fig. 105.13(a) and DPP's only on shots in Figs. 105.13(b) and 105.13(c). The dashed lines show Haan's saturation levels[18] (as described in the **Introduction** on p. 17). The smoothing conditions were varied to determine whether the shapes of modulation Fourier spectra in the nonlinear regime depend on the initial conditions. The target thickness was varied to measure the sensitivity of modulation Fourier spectra to drive conditions since target acceleration and growth rates depend on the target thickness. The shapes of the measured spectra are very similar to Haan's model predictions in all shots[25,29] (compare with Fig. 105.10). These shapes are insensitive to initial and drive conditions, as predicted by Haan's model. In the shot with more laser smoothing [Fig. 105.13(a)], the modulations are detected later than in the shot with less smoothing [Fig. 105.13(b)], and the growth is shifted by ~1 ns. In the shot with a 40-μm-thick target [Fig. 105.13(c)], the growth is detected later than with a 20-μm-thick target because of the reduced growth in the thicker target [compare Figs. 105.13(b) and 105.13(c)]. At later times, the measured modulation level becomes comparable with the target thickness and the effects of finite target thickness significantly slow the growth,[29] as shown in Fig. 105.14(a). The amplitudes of short-scale modulations

even decrease toward the end of the drive (~2.8 ns) because of this effect.[29] The measured target images [see Figs. 105.14(b) and 105.14(c)] show that smaller bubbles start to merge as larger bubbles grow during this time. In these earlier 1999 experiments, two questions still remained: (1) Do the bubble-merger processes happen around saturation levels or do they begin in a more deeply nonlinear regime (as it was considered in bubble-competition models)? (2) Is the bubble competition accompanied by a reduction of the short-wavelength modulations [as shown in Fig. 105.14(a)], or is this reduction because of the finite target thickness effects?

To address these questions and to make a connection between Fourier-space and real-space models, new experiments were conducted[26] with thicker targets driven to much higher amplitudes with longer pulses in a deeper nonlinear regime. Figure 105.15 shows examples of the measured images[26] for a shot with a 50-μm-thick target driven by a 12-ns square pulse

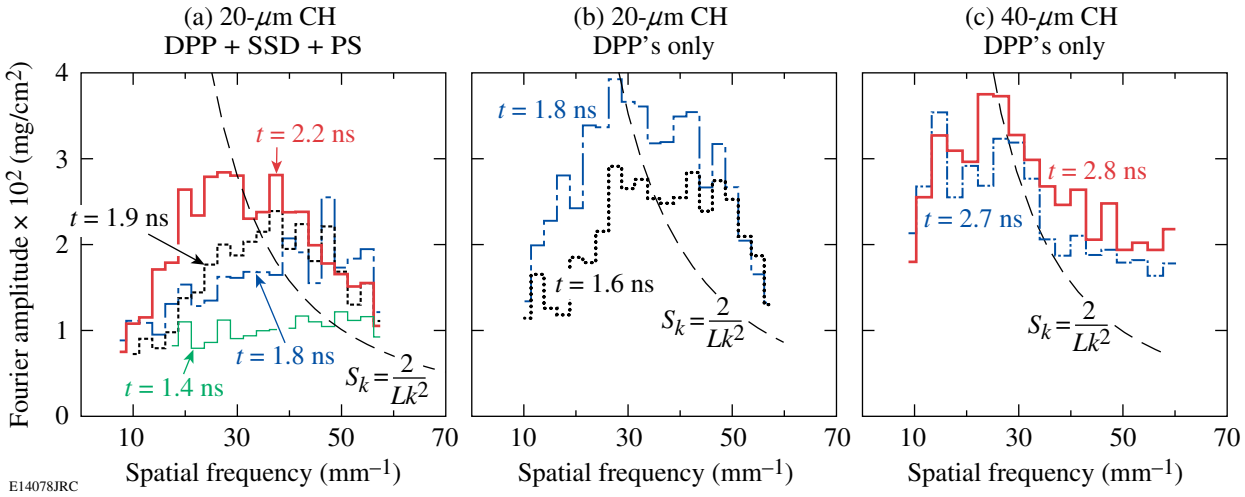

Figure 105.13
Evolution of the azimuthally averaged, areal-density modulation Fourier amplitudes as a function of spatial frequency for shots with 20-μm-thick [(a) and (b)] and 40-μm-thick (c) targets driven by a 3-ns laser pulse at an intensity of ~2×10^{14} W/cm^2 and with beam-smoothing conditions that include DDP's, SSD, and PS (a) and DPP's only [(b) and (c)]. The dashed line is Haan's saturation level $S_k = 2/Lk^2$ ($L = 400$ μm is the size of analysis box) multiplied by the calculated target density to be converted to areal density. The spectral shapes of measured modulations are similar to those predicted by Haan's model and are insensitive to initial and drive conditions.

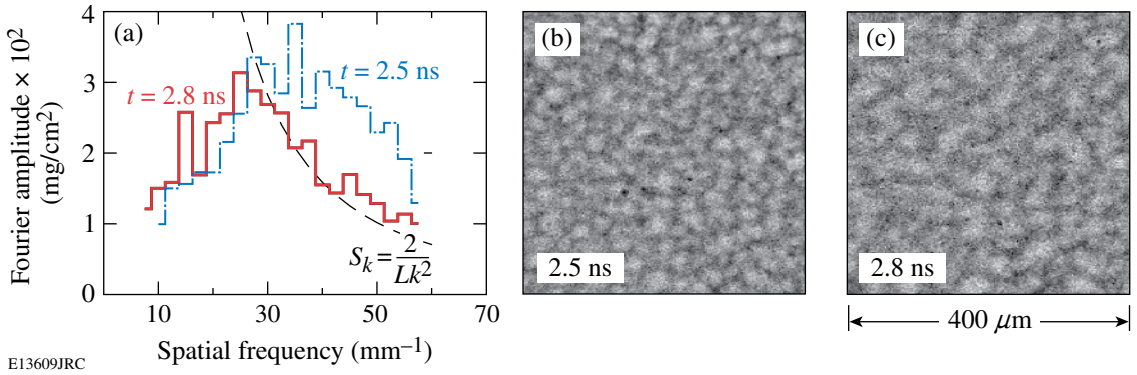

Figure 105.14
(a) Evolution of the azimuthally averaged, areal-density modulation Fourier amplitudes as a function of spatial frequency for the shot with a 20-μm-thick target driven by a 3-ns laser pulse at an intensity of ~2×10^{14} W/cm^2 and with beam-smoothing conditions including DDP's, SSD, and PS measured at 2.5 and 2.8 ns. As the level of target modulations becomes comparable to the target thickness, the modulation growth slows down and is later reversed (at 2.8 ns). The bubble-merger processes are evident from the images measured at (b) 2.5 ns and (c) 2.8 ns.

shape at an intensity of ~5×10^{13} W/cm^2. The beam-smoothing conditions in these experiments included DPP's and PS. As the modulations grow, the average bubble size shifts to longer wavelengths, big bubbles become bigger, and small bubbles disappear, as is evident from the images in Fig. 105.15. Two to three generations of bubbles change (by coalescence events) in these images, allowing clear observations of the bubble competition and merger processes. One can claim that the bubble competition and merger processes occur around saturation levels (and not only in a more advanced, turbulent regime).

Figure 105.16(a) shows examples of Fourier amplitude evolution of areal-density modulations, typical for these experiments.[26] The spectral shapes are very similar to Haan's model predictions; the amplitudes grow to much higher values than those achieved in the 1999 experiments[29] because thicker targets do not limit RT growth at the times of these measurements. The fact that in the 2005 experiments [see Fig. 105.16(a)] there is no reduction in short-wavelength modulations allows one to conclude that the bubble competition is not accompanied by a reduction of the short-wavelength modulations [as shown in

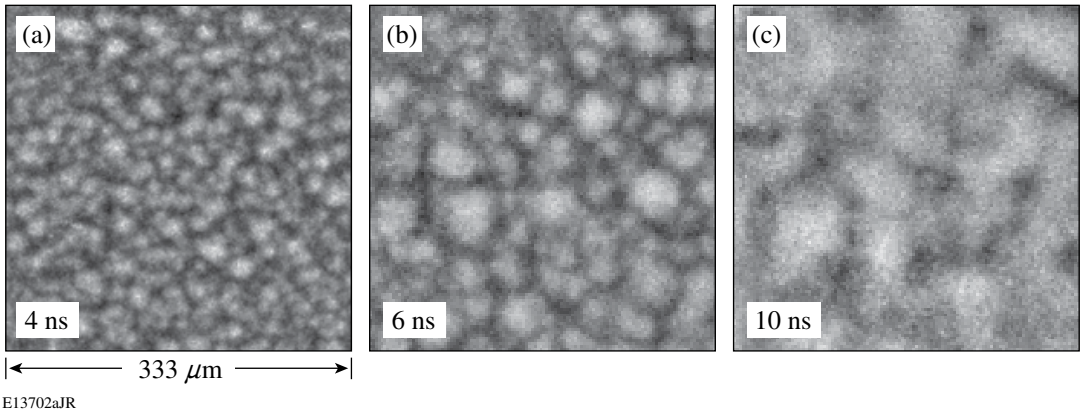

Figure 105.15
Central parts (with the analysis box size of 333 μm) of the x-ray framing-camera images measured at (a) 4 ns, (b) 6 ns, and (c) 10 ns in a 50-μm-thick target driven by a 12-ns laser pulse at an intensity of ~5×10^{13} W/cm^2 from Ref. 26. The bubble merger is evident in the images showing more advanced nonlinear RT evolution measured in thicker targets driven by longer pulses.

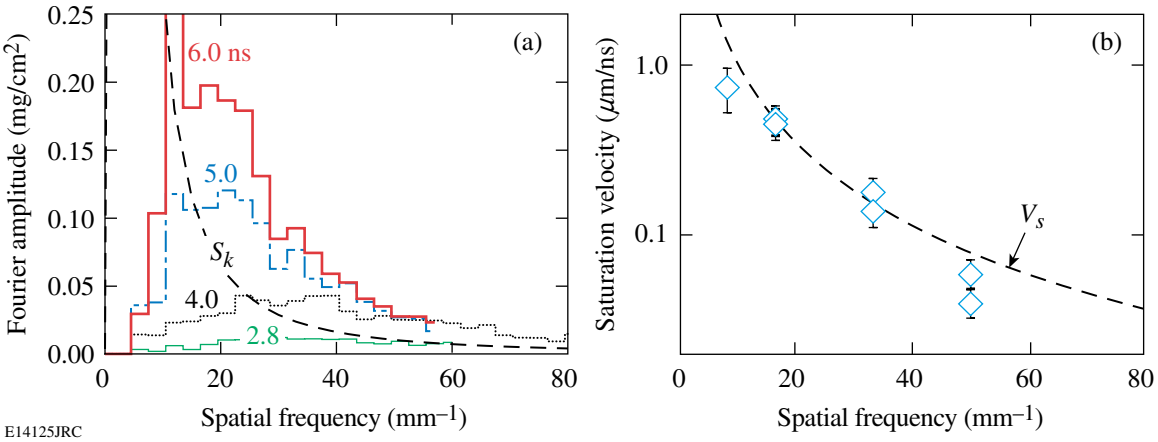

Figure 105.16
(a) Evolution of the azimuthally averaged, areal-density modulation Fourier amplitudes as a function of spatial frequency for shots with 50-μm-thick targets driven by a 12-ns laser pulse at an intensity of ~5×10^{13} W/cm^2 from Ref. 26. The dashed line is Haan's saturation level $S_k = 2/Lk^2$ ($L = 333$ μm is the analysis box size) multiplied by the calculated target density to be converted to areal density. The spectral shapes of the measured modulations are similar to those predicted by Haan's model. (b) Saturation velocities of target modulations measured at spatial frequencies of 8, 17, 33, and 50 mm^{-1} corresponding to spatial wavelengths of 120, 60, 30, and 20 μm from Ref. 26. The dashed line is Haan's saturation velocity $V_s(k) = S_k\gamma(k)$. The measured nonlinear velocities are in excellent agreement with Haan's model predictions.

Fig. 105.14(a)]—this reduction is because of the finite target thickness effects that limited RT growth and prevented clear observation of the bubble competition in the 1999 experiments. Additionally, the fact that the RT growth in the 2005 experiments is not limited by target thickness allows a direct comparison of the measured nonlinear velocities $V_s(k)$ with those predicted by Haan's model,[26] and excellent agreement between the experiments and the model was observed[26] [as shown in Fig. 105.16(b)]. We find it remarkable that this simple model predicts such complicated phenomenon as the nonlinear saturation and the postsaturation growth of the RT instability so accurately in terms of the spectral shapes and nonlinear velocities.

The real-space analysis of the 2005 experiments was based on evolution distributions of the bubble sizes and amplitudes along with the evolution of average bubble size and amplitude.[28] Figure 105.17 shows an example of the measured image with bubble edges superimposed on top of it. The bubble edges were determined using a watershed algorithm.[38] The bubble size λ was calculated using $\lambda = 2(S/\pi)^{0.5}$, where S is the bubble area. The evolution of the distributions of bubble sizes λ [corresponding to images in Figs. 105.14(a) and 105.14(b)] is shown in Fig. 105.18(a). As modulations grow, the number of bubbles decreases while their average size and amplitude increase and the distributions become broader. The measured distributions of bubble sizes were fitted with the normal distributions from which average sizes $\langle\lambda\rangle$ were determined. Figure 105.18(b) shows the normalized distributions [from Fig. 105.18(a)] as functions of normalized bubble size $\lambda/\langle\lambda\rangle$. Bubble size distributions are in the self-similar regime because the normalized distributions do not change in time. The self-similarity of RT growth is explicitly measured in these experiments using the evolution of bubble size distributions, while in earlier simulations and experiments[16,17] the self-similarity was inferred from the growth of the mixing-zone size. The dashed line in Fig. 105.18(b) represents the fit to the experimental data using the normal distribution

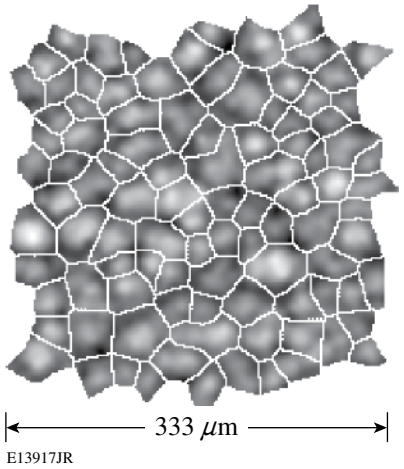

Figure 105.17
An example of the measured image with bubble edges (determined using watershed algorithm[38]) superimposed on top of it.

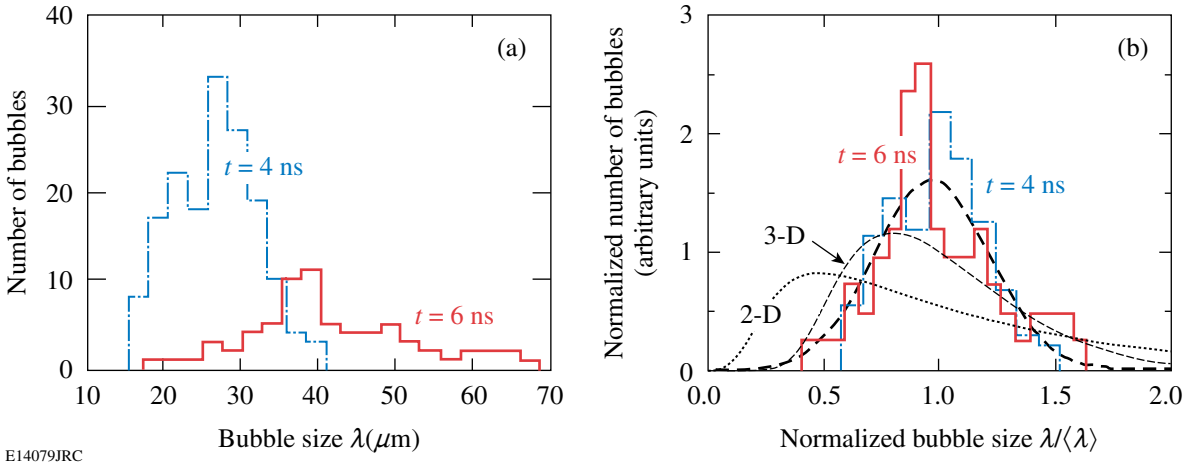

Figure 105.18
(a) Examples of the measured bubble size distributions in the images taken at 4 and 6 ns [images in Figs. 105.15(a), and 105.15(b), respectively] with a 50-μm-thick target driven by a 12-ns laser pulse at an intensity of ~5×10^{13} W/cm^2. (b) Bubble-size distributions, normalized to the total number of bubbles, as a function of the bubble size normalized to the averaged bubble size $\lambda/\langle\lambda\rangle$ for the same 4- and 6-ns images as in (a). The measured bubble distributions are in a self-similar regime because their normalized distributions do not change in time. The thicker dashed line represents a normal distribution fit to the data.

$f_\sigma(\lambda/\langle\lambda\rangle) = \exp\left[-(\lambda/\langle\lambda\rangle - 1)^2 \Big/ 2C_\lambda^2\right] \Big/ \sqrt{2\pi} \cdot C_\lambda$, where C_λ = 0.24±0.01 is the constant determined from the fit. The dotted and dot–dashed lines in Fig. 105.18(b) are the distributions predicted from the 2-D and 3-D models, respectively (presented in Ref. 27). The 3-D model prediction is in better agreement with the experimental results, as expected. It was shown[28] that the modulation $\sigma_{\rm rms}$ grows as $\alpha_\sigma g t^2$, as expected in a self-similar regime, where g is the foil acceleration, t is the time, and α_σ = 0.027±0.003 is a measured constant. The bubble-front amplitude h_b can be estimated[18] as $h_b \sim \sqrt{2}\,\sigma_{\rm rms}$, which yields $h_b \sim 0.04\ gt^2$. It was shown in Refs. 20 and 39 that Haan's saturation at amplitudes $S_k = 2/Lk^2$ in Fourier space is equivalent to self-similar growth $h_b = 0.04\ gt^2$ in real space. Therefore, experimentally measured growth is in agreement with what was predicted.[20,39] The weak, logarithmic dependence of the α_σ on the initial conditions[17] still requires experimental verification for ablative acceleration.

The experimental results presented above show the behavior of "average" modulation characteristics. The evolution of the average amplitude (calculated by the azimuthal average of the 2-D Fourier image) was compared with Haan's model predictions in Fourier space. The analysis in real space was presented in terms of bubble size distributions. The measured data, however, can also be used to quantitatively describe what happens to an individual bubble (in real space) and individual Fourier mode (in Fourier space). Figure 105.19 shows images of the modulation growth at the same area of the target measured at 2.7, 3.5, and 4.3 ns in the shot with a 35-μm-thick target driven at an intensity of ~5×10^{13} W/cm^2.

Figure 105.20 shows overlapped bubble contours of the 2.7- (gray lines) and 4.3-ns (black lines) images. As evident from this figure, some bubbles coalesce with others to form larger bubbles. Some bubbles disappear and other bubbles expand to take their place, while some bubbles stay in their original place without changing sizes. As for the Fourier-space analysis, if all modes at any wavelength grow uniformly according to Haan's model prediction for the average modulation growth, there could not be a bubble merger in real space. Therefore, to be consistent with the bubble-merger picture of real-space evolution, the individual Fourier modes at a given

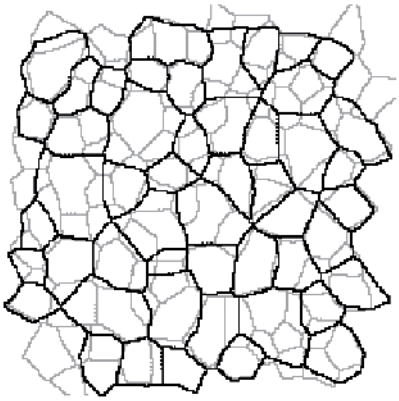
E14081JR

Figure 105.20
Bubble edge contours of the 2.7-ns (gray contours) and (c) 4.3-ns (black contours) images from Fig. 105.19. Some of the bubbles do not change their size while most bubbles merge into bigger bubbles and some bubbles disappear during evolution.

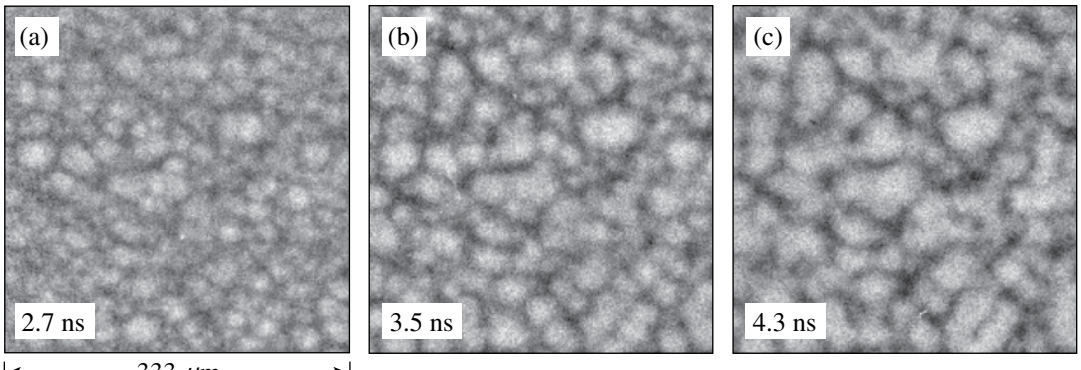

E14080JR

Figure 105.19
The evolution of the same target area as shown by the central parts (with a 333-μm analysis box size) of the x-ray framing-camera images measured at (a) 2.7 ns, (b) 3.5 ns, and (c) 4.3 ns in a 35-μm-thick target driven by a 12-ns laser pulse at an intensity of ~5×10^{13} W/cm^2. The evolution of each modulation feature can be tracked in these images.

(mainly short) wavelength should have a different growth than their average amplitude. Figure 105.21(a) shows the Fourier image with typical "spiky" amplitudes, characteristic to "noise-like" 3-D modulations. The azimuthal lineout of data at a 60-μm wavelength is shown in Fig. 105.21(b). There are many modes in this lineout and their average amplitude grows according to Haan's model prediction, as shown above. Is the growth of each individual mode in this lineout the same as the growth of the average amplitude? If it is the same, then the phase of each mode (related to the ratio of the real and imaginary parts of the mode's complex amplitude) does not change in time. Figure 105.21(c) shows the evolution of the absolute values of modes in a 60-μm wavelength lineout from 2.7 to 3.5 ns, while the evolution of the modes in a 20-μm wavelength lineout is presented in Fig. 105.21(d). These data show that all 60-μm wavelength modes grow similarly, while modes at a 20-μm wavelength do not all grow the same way and many phase changes are seen during the growth of these short-wavelength modes. Figure 105.21(e) shows the histograms of the absolute values of the phase changes of all modes at spatial wavelengths of 20, 30, and 60 μm measured between 3.5- and 2.7-ns images. At wavelengths of 30 and 60 μm, most of the modes do not change phases, while most of the modes at wavelengths of 20 μm change their phases significantly. As a result, the bubble merger in Fourier space corresponds to short-wavelength modes growing nonuniformly (with many modes changing their phases significantly), while longer-wavelength modes do not change their phases, meaning that the images keep their long-wavelength structure unchanged.

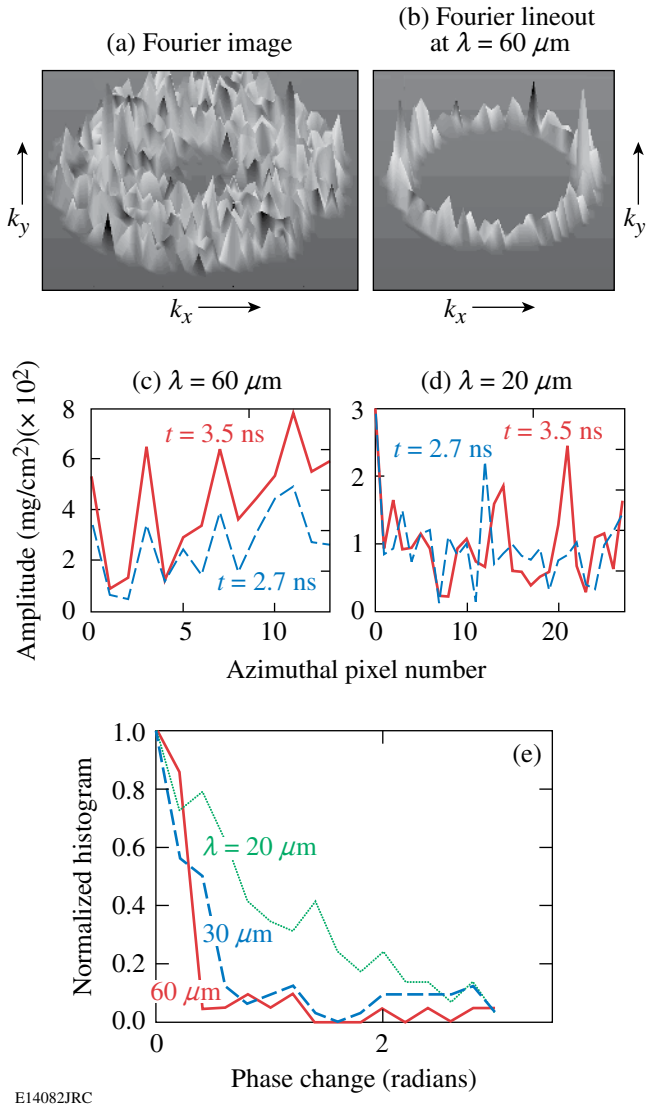

Figure 105.21
(a) An example of the typical measured Fourier-space image (shown in terms of the absolute value). (b) The azimuthal lineout of this image at a spatial wavelength of 60 μm. The azimuthal lineouts of absolute values of Fourier modes at a (c) 60-μm wavelength and a (d) 20-μm wavelength measured at 2.7 and 3.5 ns. (e) Normalized (to the value at zero phase change) histograms of the absolute phase change of the modes at spatial wavelengths of 20, 30, and 60 μm calculated from the difference of the 2.7- and 3.5-ns images. The bubble merger in Fourier space corresponds to the short-wavelength modes growing nonuniformly (with many modes changing their phases significantly), while longer-wavelength modes do not change their phases.

Conclusions

The nonlinear Rayleigh–Taylor growth of 3-D nonuniformities was measured near saturation levels using x-ray radiography in laser-driven planar foils. The initial target modulations were seeded by laser nonuniformities. The measured modulation Fourier spectra and nonlinear growth velocities are in excellent agreement with Haan's model[18] predictions in Fourier space.[25,26] These spectra and growth velocities are insensitive to initial conditions. Bubble competition and merger was quantified by the evolution of bubble size distributions in real space. A self-similar evolution of these distributions was observed.[28]

ACKNOWLEDGMENT

This work was supported by the U.S. Department of Energy Office of Inertial Confinement Fusion under Cooperative Agreement No. DE-FC52-92SF19460, the University of Rochester, and the New York State Energy Research and Development Authority.

REFERENCES

1. Lord Rayleigh, Proc. London Math Soc. **XIV**, 170 (1883).
2. G. Taylor, Proc. R. Soc. London Ser. A **201**, 192 (1950).
3. J. D. Lindl, Phys. Plasmas **2**, 3933 (1995).

4. B. A. Remington *et al*., Phys. Plasmas **4**, 1994 (1997).
5. K. S. Budil *et al*., Phys. Rev. Lett. **76**, 4536 (1996).
6. H. Takabe *et al*., Phys. Fluids **28**, 3676 (1985).
7. R. Betti, V. N. Goncharov, R. L. McCrory, P. Sorotokin, and C. P. Verdon, Phys. Plasmas **3**, 2122 (1996).
8. K. Shigemori *et al*., Phys. Rev. Lett. **78**, 250 (1997).
9. S. G. Glendinning, S. N. Dixit, B. A. Hammel, D. H. Kalantar, M. H. Key, J. D. Kilkenny, J. P. Knauer, D. M. Pennington, B. A. Remington, R. J. Wallace, and S. V. Weber, Phys. Rev. Lett. **78**, 3318 (1997).
10. C. J. Pawley *et al*., Phys. Plasmas **6**, 565 (1999).
11. J. P. Knauer, R. Betti, D. K. Bradley, T. R. Boehly, T. J. B. Collins, V. N. Goncharov, P. W. McKenty, D. D. Meyerhofer, V. A. Smalyuk, C. P. Verdon, S. G. Glendinning, D. H. Kalantar, and R. G. Watt, Phys. Plasmas **7**, 338 (2000).
12. T. Sakaiya *et al*., Phys. Rev. Lett. **88**, 145003 (2002).
13. B. A. Remington *et al*., Phys. Fluids B **5**, 2589 (1993).
14. K. I. Read, Physica **12D**, 45 (1984).
15. D. H. Sharp, Physica **12D**, 3 (1984).
16. M. B. Schneider, G. Dimonte, and B. Remington, Phys. Rev. Lett. **80**, 3507 (1998).
17. G. Dimonte, Phys. Rev. E **69**, 056305 (2004).
18. S. W. Haan, Phys. Rev. A, Gen. Phys. **39**, 5812 (1989).
19. S. W. Haan, Phys. Fluids B **3**, 2349 (1991).
20. D. Ofer, U. Alon, D. Shvarts, R. L. McCrory, and C. P. Verdon, Phys. Plasmas **3**, 3073 (1996).
21. C. L. Gardner *et al*., Phys. Fluids **31**, 447 (1988).
22. Q. Zhang, Phys. Lett. A **151**, 18 (1990).
23. J. Glimm and X. L. Li, Phys. Fluids **31**, 2077 (1988).
24. U. Alon *et al*., Phys. Rev. Lett. **74**, 534 (1995).
25. V. A. Smalyuk, T. R. Boehly, D. K. Bradley, V. N. Goncharov, J. A. Delettrez, J. P. Knauer, D. D. Meyerhofer, D. Oron, and D. Shvarts, Phys. Rev. Lett. **81**, 5342 (1998).
26. V. A. Smalyuk, O. Sadot, J. A. Delettrez, D. D. Meyerhofer, S. P. Regan, and T. C. Sangster, Phys. Rev. Lett. **95**, 215001 (2005).
27. D. Oron *et al*., Phys. Plasmas **8**, 2883 (2001).
28. O. Sadot, V. A. Smalyuk, J. A. Delettrez, D. D. Meyerhofer, T. C. Sangster, R. Betti, V. N. Goncharov, and D. Shvarts, Phys. Rev. Lett. **95**, 265001 (2005).
29. V. A. Smalyuk, T. R. Boehly, D. K. Bradley, V. N. Goncharov, J. A. Delettrez, J. P. Knauer, D. D. Meyerhofer, D. Oron, D. Shvarts, Y. Srebro, and R. P. J. Town, Phys. Plasmas **6**, 4022 (1999).
30. T. R. Boehly, D. L. Brown, R. S. Craxton, R. L. Keck, J. P. Knauer, J. H. Kelly, T. J. Kessler, S. A. Kumpan, S. J. Loucks, S. A. Letzring, F. J. Marshall, R. L. McCrory, S. F. B. Morse, W. Seka, J. M. Soures, and C. P. Verdon, Opt. Commun. **133**, 495 (1997).
31. Y. Lin, T. J. Kessler, and G. N. Lawrence, Opt. Lett. **20**, 764 (1995).
32. V. A. Smalyuk, V. N. Goncharov, T. R. Boehly, D. Y. Li, J. A. Marozas, D. D. Meyerhofer, S. P. Regan, and T. C. Sangster, Phys. Plasmas **12**, 040702 (2004).
33. V. A. Smalyuk, V. N. Goncharov, T. R. Boehly, J. A. Delettrez, D. Y. Li, J. A. Marozas, A. V. Maximov, D. D. Meyerhofer, S. P. Regan, and T. C. Sangster, Phys. Plasmas **12**, 072703 (2005).
34. S. V. Weber, S. G. Glendinning, D. H. Kalantar, M. H. Key, B. A. Remington, J. E. Rothenberg, E. Wolfrum, C. P. Verdon, and J. P. Knauer, Phys. Plasmas **4**, 1978 (1997).
35. V. N. Goncharov, S. Skupsky, T. R. Boehly, J. P. Knauer, P. McKenty, V. A. Smalyuk, R. P. J. Town, O. V. Gotchev, R. Betti, and D. D. Meyerhofer, Phys. Plasmas **7**, 2062 (2000).
36. S. P. Regan, J. A. Marozas, J. H. Kelly, T. R. Boehly, W. R. Donaldson, P. A. Jaanimagi, R. L. Keck, T. J. Kessler, D. D. Meyerhofer, W. Seka, S. Skupsky, and V. A. Smalyuk, J. Opt. Soc. Am. B **17**, 1483 (2000).
37. T. R. Boehly, V. A. Smalyuk, D. D. Meyerhofer, J. P. Knauer, D. K. Bradley, R. S. Craxton, M. J. Guardalben, S. Skupsky, and T. J. Kessler, J. Appl. Phys. **85**, 3444 (1999).
38. L. Vincent and P. Soille, IEEE Trans. Pattern Anal. Mach. Intell. **13**, 583 (1991).
39. M. J. Dunning and S. W. Haan, Phys. Plasmas **2**, 1669 (1995).

Isotopic Fractionation During Solidification of H_2–HD–D_2 Mixtures

Introduction

In inertial fusion experiments, it is energetically advantageous to form the fuel into a solid shell before compression.[1] Current cryogenic target experiments on OMEGA are being performed with pure deuterium (D_2) as the fuel.[2] Future cryogenic target experiments will be performed with an equimolar solid mixture of deuterium and tritium (D-T). An equilibrium D-T mixture consists of D_2, DT, and T_2 molecules in a 25:50:25% ratio. Each molecular species has a different triple point, which may lead to fractionation of the isotopes during fuel-layer formation. Spatial separation of the D and T nuclei due to isotopic fractionation during the cryogenic target layering process reduces the efficiency of the fusion reaction.[3]

Complete isotopic fractionation has long been predicted for hydrogen isotopes for temperatures approaching absolute zero—well below the triple point of the mixture.[4] It has been observed for ^{3}He-^{4}He mixtures but not for bulk solid hydrogen isotope mixtures. Partial fractionation of hydrogen–deuterium mixtures has been observed in monolayers adsorbed onto graphite substrates using neutron scattering and x-ray diffraction.[5] The separation is mainly limited to the formation of local molecular clusters of one isotope versus the other as the monolayer is completed. It was speculated that no long-range ordering was observed because of the limited mobility of the molecules at temperatures approaching 3 K.

We have examined the possibility of fractionation in cryogenic targets using a 25:50:25% mixture of H_2, HD, and D_2 (H-D). The use of nonradioactive hydrogen isotopes allows a simpler experimental system to be constructed without the radiological controls necessary for using tritium. Although nonradiological experiments are easier to perform, less fractionation may occur in samples containing tritium. Molecular diffusion in the bulk may be enhanced for D-T mixtures because of the large amount of energy deposited locally from β decay, which raises the neighboring solid's temperature and disassociates nearby molecular bonds. This study investigates fractionation that occurs during the liquid-to-solid phase transition near the triple point. Possible fractionation during solid-to-vapor-to-solid mass transfer during β-layering or IR-enhanced β-layering as a result of sublimation and refreezing will be investigated in a future study.

For the liquid-to-solid phase transition, there was little separation of the isotopes during the solidification process. The maximum spatial concentration gradients are of the order of 0.02 to 0.05 molecular fraction per millimeter. The average D_2 concentration gradient (percentage) is greatest for the lowest D_2 concentrations. The absorption coefficient's gradient was also measured and appears to be less for the longer cooling times, which may be indicative of solid diffusion. Thermodynamically, the mixtures form a completely soluble isomorphous system since the mixture solidifies over a finite temperature range for all concentrations.

Experimental Details

By scanning a focused infrared (IR) laser probe tuned to the major absorption band of D_2 at $\tilde{\nu} = 3162\ \text{cm}^{-1}$ ($\lambda = 3.162\ \mu$m) across a thin, slowly frozen solid sample of the mixture, the D_2 concentration as a function of position can be determined. The infrared absorption spectrum of pure deuterium is shown in Fig. 105.22. The major absorption peak of solid D_2 is from an induced dipole interaction between adjacent D_2 molecules in the crystal.[7] Solid hydrogen forms a hexagonal close-packed crystal at its vapor pressure. Therefore, each molecule has 12 nearest neighbors in the crystal, as shown in Fig. 105.23. Substitution of H_2 or HD into these sites will reduce the D_2–D_2 dipole interaction and increase the local IR transmission.

A schematic of the commercially available[8] infrared Pb:salt laser system is shown in Fig. 105.24. The IR laser diode is housed in a liquid-nitrogen (LN_2) dewar and is operated at ~125 K and ~650 mA to produce an optical power approaching 1 mW at 3162 cm^{-1}. The laser source is a PbSe double-hetero-structure, single-mode diode laser for high-resolution spectroscopy. It has a typical line width of 6.7×10^{-4} cm^{-1}, a current tuning rate of 0.09 cm^{-1}/mA, and a temperature tuning rate of 4 cm^{-1}/K. This gives a wave number tuning range of ~3.140 to 3.190 cm^{-1} over the operable temperature/current range. Even though the line

width is very narrow, by coarsely tuning the temperature and finely tuning the current, any wave number within the specified range can be achieved.

The light is collimated using an off-axis parabolic mirror which can be positioned in three dimensions. The light is sent through a grating monochrometer that has been precalibrated to transmit only 3.162±0.003-μm light. The wavelength emitted by the laser diode is adjusted by varying its current at a fixed temperature until maximum transmission through the monochrometer is obtained. The dual-detector photodiode is also housed in a LN_2 dewar. A small fraction (~10%) of the beam is split off and focused onto one detector to monitor the stability of the laser source during data acquisition (refer to this as the reference beam).

The remainder of the beam is transported through the sample. The light is focused to a 0.3-mm × 0.6-mm spot on the sample using an off-axis parabolic mirror mounted on a five-axis positioner. It is recollimated on the other side of the

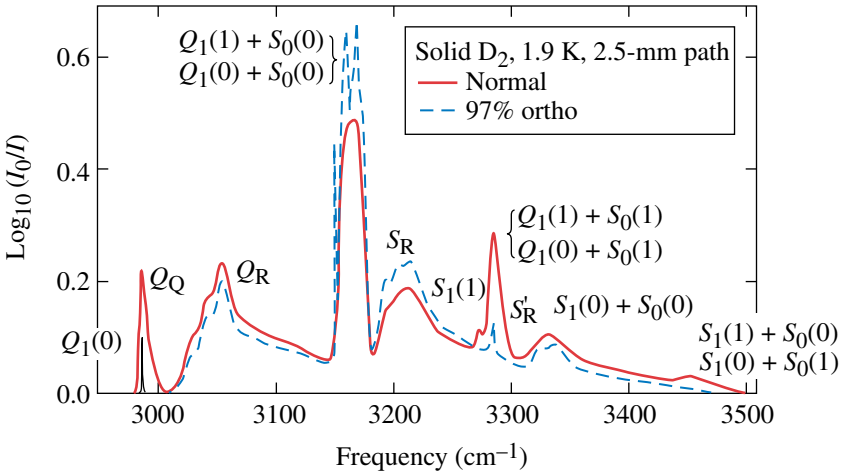

T2067aJR1C

Figure 105.22
The absorption spectrum of solid D_2 at 1.9 K for a 2.5-mm-thick sample. (Figure courtesy of the Canadian Journal of Physics.)[6]

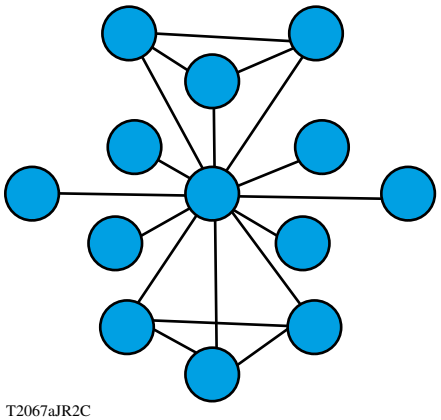

T2067aJR2C

Figure 105.23
Each molecule in the hexagonal close-packed structure of solid hydrogen is neighbored by 12 other molecules. Substitution of non-D_2 molecules into these sites will interfere with adjoining D_2–D_2 dipole interactions and greatly reduce the absorption coefficient of the solid.

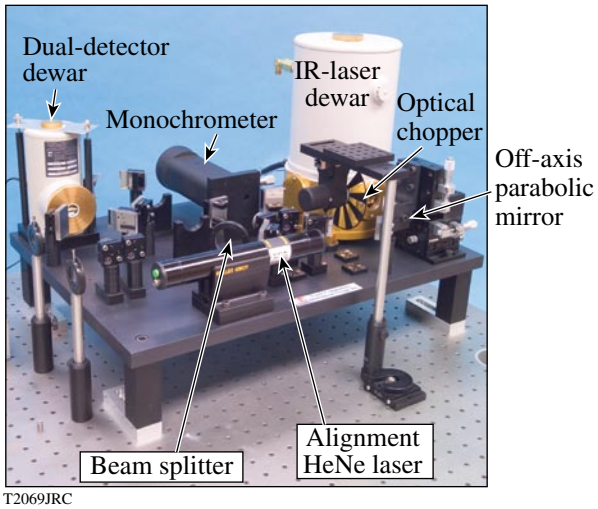

T2069JRC

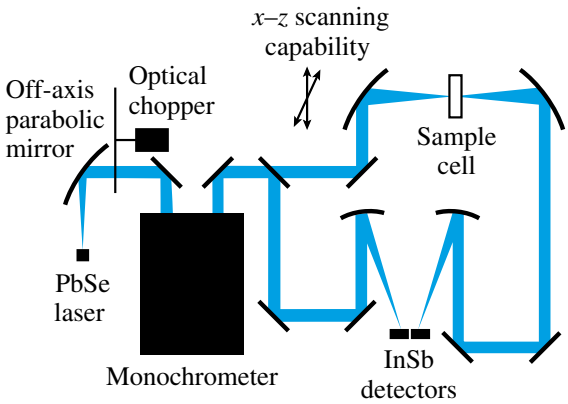

Figure 105.24
The optical layout and a schematic of the infrared Pb:salt laser system.

sample with an identical mirror and positioner. The mirrors are mounted on a stage that can be positioned with micrometer screws vertically and horizontally with respect to the fixed sample without causing the beam to "walk off" in the remainder of the optical system. This beam is subsequently focused onto the other detector (refer to this as the sample beam). The output of the IR laser is chopped at 790 Hz and the signals from each detector are sent to a chopper-synchronized lock-in amplifier with a 30-ms integration period.

A sketch of the sample cell used to form the H-D crystal is shown in Fig. 105.25. The oxygen-free, high-conductivity copper cell is cooled from the bottom using a low-vibration Gifford-McMahon cryogenic refrigerator.[9] The cylindrical void that is filled with H-D is 6.4 mm in diameter by 3 mm thick; 2-mm-thick CaF windows are glued to either side of the copper cell. CaF was used instead of sapphire because of its lower thermal conductivity but similar IR transmittance at 3.162 μm. A heater and thermometer are attached to the top and bottom of the sample to produce a temperature gradient (~0.5 K maximum) across the sample.

The sample cell is loaded with liquid H-D through a 0.5-mm-diam stainless steel fill tube using a gas source pressure <10 psia. For isotope mixtures, the sample cell is filled with just enough liquid to completely fill it before freezing to eliminate possible preferential condensation of the different isotopes from the gas-phase reservoir because of their different vapor pressures at a fixed temperature. This eliminates the possibility of a concentration gradient forming because of the different vapor pressures of each isotope instead of from their different triple points. The cell remains connected to an external room-temperature gas source for isomolecular samples since they exhibit a single vapor pressure for each temperature, thus, the frozen sample completely fills the cell for these solid samples. The sample is cooled slowly (hours to days) by reducing the temperature at the top of the cell gradually to a value just below the final freezing temperature of the mixture.

Two flip-in mirrors are mounted before and after the parabolic mirrors. The first provides white-light illumination of the sample and the second sends the transmitted light to an imaging system with a CCD detector. This allows the sample to be viewed as the H-D solidifies. When examined between crossed linear polarizers, the crystal structure of the solid H-D is revealed (see example in Fig. 105.26). A HeNe laser beam can be made coaxial to the IR beam using a flip-in beamsplitter that allows visible alignment of the IR beam path. Using the second flip-in mirror alone with the HeNe beam, the focal spot of the IR beam can be located on the sample's image to provide beam position feedback.

The IR beam is raster scanned across the sample cell to determine if a D_2 concentration gradient is present. The signal from the sample beam is recorded as a function of position at 0.5-mm increments. The signal from the reference beam is recorded periodically throughout the measurement to confirm the stability of the IR laser diode. (Typically, the output was sta-

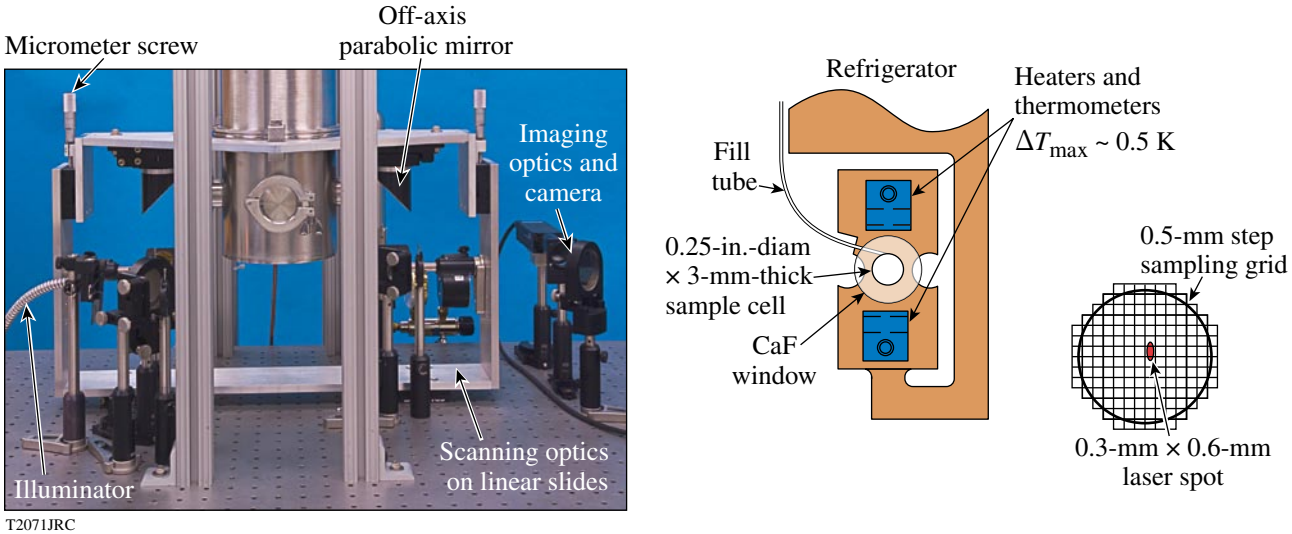

Figure 105.25
The scanning optics configuration and a sketch of the sample cell in which the H-D crystal is formed.

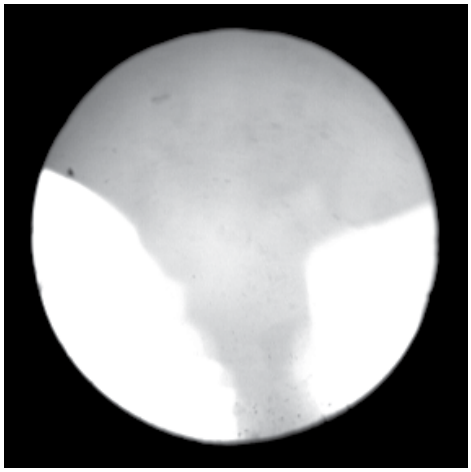
T2072JR

Figure 105.26
An image of a white-light, back-illuminated, solid pure D_2 sample. The crystal structure of the solid is revealed when examined between crossed linear polarizers; three distinct crystallites can be seen. The sample was frozen by reducing the temperature at the top of the sample from 19.2 K to 18.7 K over a 20-h period. The sample began to freeze at a bottom temperature of 18.7 K.

ble to <2% for the duration of the measurement.) The sample is subsequently vaporized at 30 K and the signal from the sample beam is recorded as a function of position for the empty cell. The two measurements are ratioed to create a transmission plot $T(x,z)$, as shown in Fig. 105.27(b). The absorption coefficient $\alpha(x,z)$ is calculated from Beer's Law and includes a correction for the change in refractive index of the sample cell's contents with the solid present and absent (see appendix, p. 33).

Results

The transmission plot of the 25:50:25% H_2:HD:D_2 mixture, along with that of a pure D_2 sample, is shown in Fig. 105.27. (The mean absorption coefficient for each sample is given in Fig. 105.29.) Note that α for the H-D mixture is ~1/20th of that for the pure D_2. This reduction is disproportionate to the reduction in D_2 nearest neighbors—from 12 to 3 in the hexagonal close-packed crystal. In fact, the 3-mm-thick H-D mixture is >96% transmissive even though one in four molecules is D_2. In contrast, a pure D_2 sample is only 40% transmissive. This is attributed to the simultaneous transition absorption requirement of two neighboring D_2 molecules, each absorbing a portion of the incident quantum.[10] Therefore, the interference of non-D_2 molecules between adjacent D_2 molecules greatly reduces the absorption coefficient of the bulk material. Any gradient present in this H-D transmission plot is easily masked by the noise in the data. The sensitivity of the D_2 absorption coefficient to concentration must first be resolved before a change in absorption can be quantified as a concentration gradient.

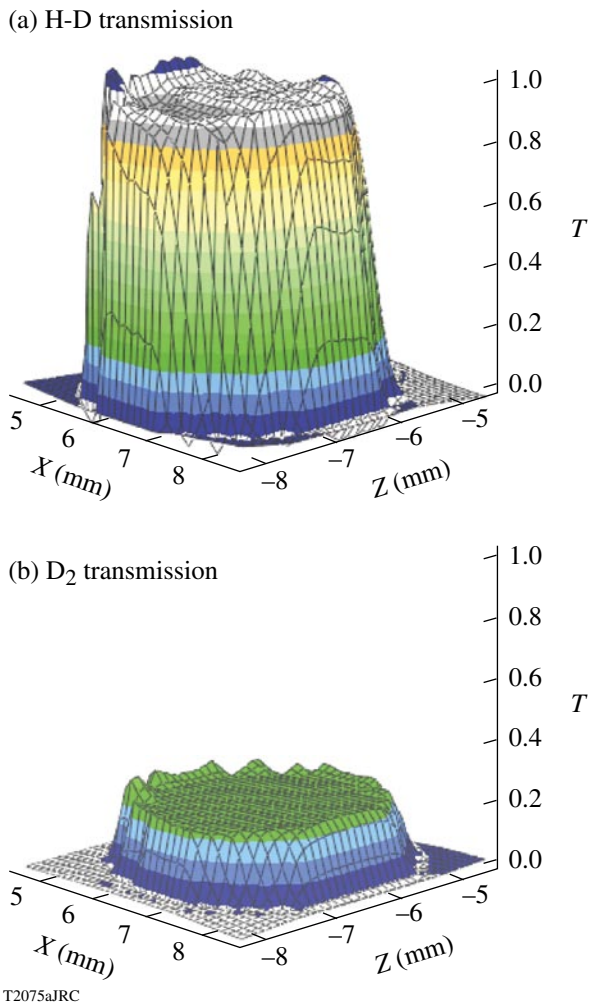

T2075aJRC

Figure 105.27
Typical transmission plots for (a) 25:50:25% H_2:HD:D_2 and (b) pure D_2. The absorption coefficients are 0.017 and 0.317 mm^{-1}, respectively; a 20× difference for a factor of 4 difference in D_2 concentration that is clearly outside the linear region of Beer's Law.

Beer's Law follows a linear relationship between the absorption coefficient and solute concentration for low concentrations (<10%). At these relatively high concentrations of D_2 in the H-D mixture (25% < D_2 < 100%), however, nonlinear deviations from Beer's Law are expected. The absorption coefficient of the D_2 in the H-D is a function of the D_2 intermolecular distance[11] as follows:

$$\alpha(\omega) \propto \sum_{nn'} (P_n - P_{n'}) \left| \langle n' | \mu | n \rangle \right|^2 \delta(\omega - \omega_{nn'}),$$

where $\omega = 2\pi c/\lambda$ is the angular frequency of the incident radiation, P_n is the probability of occupancy of state n (P_n corresponding to absorption and $P_{n'}$ to spontaneous emission), μ is the dipole moment of the molecule, and $\delta(\omega - \omega_{nn'})$ is the

Dirac delta function centered at the resonant frequency $\omega_{nn'}$. The dipole moment μ is proportional to $Q_{\text{internuclear}} + Q_{\text{eqq}}$, however, where $Q_{\text{internuclear}}$ is related to a van der Waal's interaction and Q_{eqq} is the electric quadrapole–quadrapole interaction which varies as $1/r_e^4$, where r_e is the D_2 intermolecular distance. The intermolecular distance between D_2 molecules in the H-D mixture is inversely proportional to the D_2 concentration. Therefore, by plotting the absorption coefficient of the D_2 in the H-D mixture as a function of the D_2 fraction in the mixture, the slope can be used to quantify a transmission gradient as a concentration gradient.

A variety of H_2-D_2 mixtures were solidified at varying rates and their $\alpha(x,z)$ measured. Three to seven individual samples were frozen and measured for each mixture to obtain adequate statistics. The transmission data is fit to a plane to determine the average transmission and the transmission gradient, as shown in Fig. 105.28. The resulting average absorption coefficient of the D_2 in the H-D mixture (at $\lambda = 3.151$ μm) is plotted as a function of the D_2 molecular fraction f_{D_2} in Fig. 105.29. The function that best fits the data is

$$\alpha\left(f_{D_2}\right) = \exp\left(4.20 \times f_{D_2} - 5.26\right)\text{mm}^{-1}.$$

Conversely, to find the D_2 molecular fraction from the mean absorption coefficient

$$f_{D_2} = \frac{\left[\ln(\alpha \times 1\text{ mm}) - 5.26\right]}{4.20}. \quad (1)$$

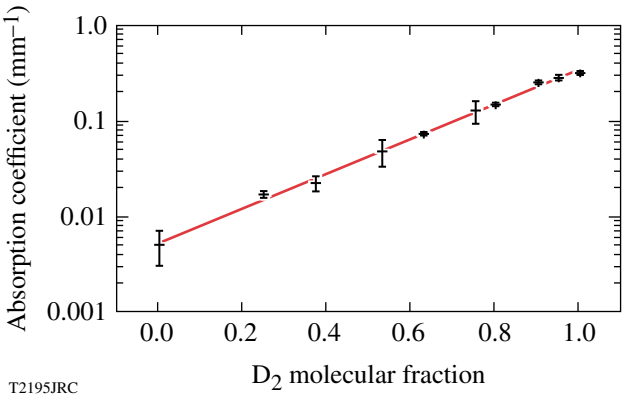

Figure 105.29
The average absorption coefficient of the D_2 in the H-D mixture as a function of the D_2 molecular fraction at an IR diode wavelength of $\lambda = 3.151$ μm. The vertical error bars indicate ±1 standard deviation of the various experimental runs that were averaged for each point. The results from pure H_2 and D_2 samples are included for completeness. The finite absorption coefficient for H_2 indicates the scattering baseline of the experiment.

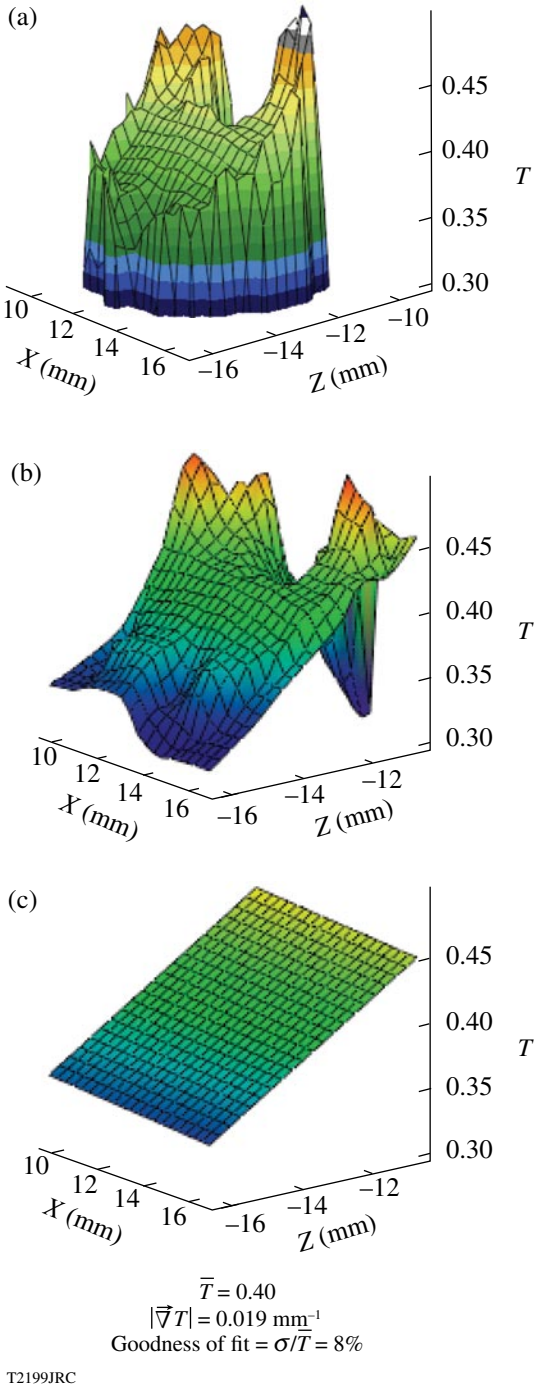

Figure 105.28
The transmission plots are processed from the raw data shown in (a) by first eliminating spurious data points to produce the plot in (b) and then fitting it to a plane, as shown in (c), to subsequently determine the D_2 concentration gradient. The hole at the top of the data is formed during solidification because of the large difference between the liquid and solid densities of hydrogen since the sample cell is filled with just enough liquid to completely fill it before freezing commences.

A plot of the absorption coefficient gradient as a function of freeze time is shown in Fig. 105.30. The samples were generally measured <2 h following solidification. The absorption coefficient gradient appears to be inversely proportional to the cooling time, but there is a large scatter in the data—especially for the shorter cooling times. This may be evidence of molecular diffusion in the bulk solid. Molecular diffusion between adsorbed H-D monolayers on graphite has been observed[5] to be of the order of 5×10^{-6} cm^2/s near the triple point (17 K). This value increases by an order of magnitude at 30 K for adsorbed monolayers, but this temperature obviously cannot be obtained in the unpressurized solid. Molecular diffusion in the bulk may be enhanced for D-T mixtures because of the large amount of energy (~12 keV average) deposited locally from β decay, thus raising the neighboring temperature and disassociating molecular bonds.

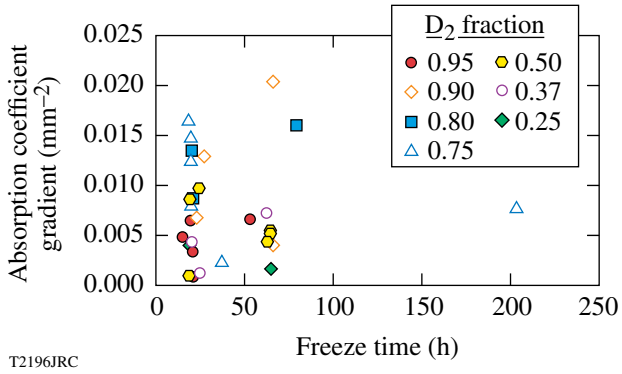

Figure 105.30
The absorption coefficient gradient as a function of freeze time. The vertical groupings indicate that most cooldowns were performed either over ~24 h or over ~72 h. A single long-duration cooldown is shown at the right of the figure. A few anomalous points occur at the top of the figure that may be indicative of IR scattering in the raw transmission data for these points.

It may be argued that scattering sites in the bottom of the sample are producing the apparent concentration gradient. These could originate from the large temperature excursion that the bottom of the sample undergoes during the freezing of the entire sample and the subsequent thermal contraction creating microcracks. This hypothesis is not supported by a plot of the absorption coefficient gradient as a function of initial bottom minus final top temperature (Fig. 105.31). In fact, observable cracks and striations do appear in the sample during the freeze duration but generally anneal out during the course of solidification. In addition, the absorption coefficient gradients for samples of individual isotopes are ~10^{-4} 1/mm^2—several orders of magnitude less than those for the mixtures—indicating that no scattering-induced gradients are present.

The average percentage D_2 concentration gradient $\left(\Delta f_{D_2} / \Delta_z \times 1 / f_{D_2}\right)$ is greatest for the lowest concentrations, as shown in Fig. 105.32. Among the samples tested, however, the absolute concentration gradients $\left(\Delta f_{D_2} / \Delta_z\right)$ are of the order of 0.02 to 0.05 mm^{-1}. The large error bars shown for the lowest concentrations indicate the signal-to-noise ratio in the measurement is smallest when the sample is the least absorptive. This is another reason why the data in Fig. 105.29 are most useful

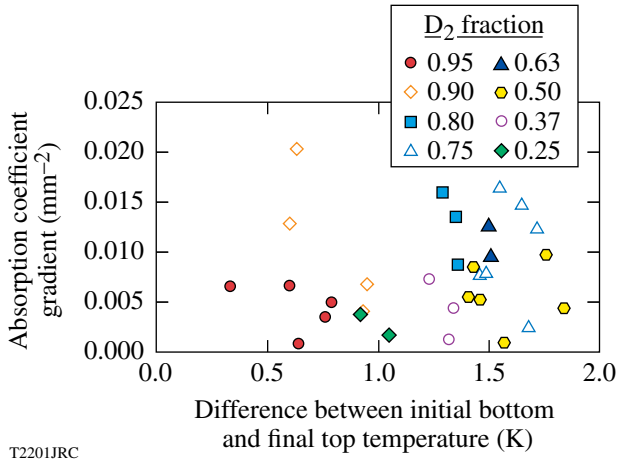

Figure 105.31
A plot of the absorption coefficient gradient as a function of the difference between the initial bottom and the final top temperature. If the gradient observed was due to increased IR scatter in the lower portion of the sample from microcracks, the trend in the data should be diagonal from bottom left to upper right. The data does not reflect this and is more or less randomly distributed.

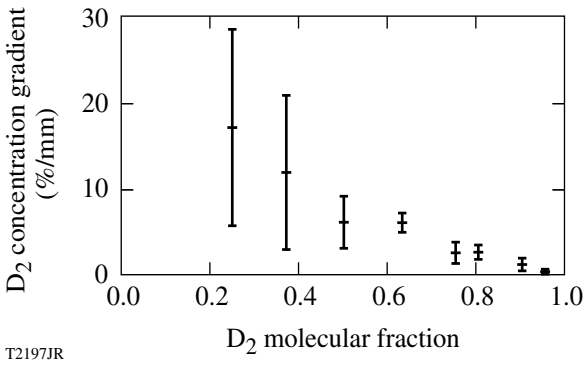

Figure 105.32
The average percentage D_2 concentration gradient in the H-D mixture as a function of the D_2 molecular fraction. The vertical error bars indicate ±1 standard deviation of the various experimental runs that were averaged for each point and are greatest for the lowest concentrations since the signal-to-noise ratio is smallest for the least absorptive samples. The absolute concentration gradients are of the order of 0.02 to 0.05 molecular fraction mm^{-1}.

Table 105.I: Calculated first-freezing temperatures for the 25:50:25% H_2:HD:D_2 mixture using Eq. (2). Molecular fractions are based on both the pressurization schedule of the gas reservoir when the sample was prepared and on an independent measurement of the sample using cryogenic gas chromatography. The final column is the first-freezing temperature of the remaining 33:67% H_2:HD mixture if the D_2 completely froze out of the solution first.

Molecule	Triple point (K)	Mass fraction from pressure	Mass fraction from mass spectrometer	Mass fraction with frozen D_2
H_2	13.96	0.249±0.005	0.26±0.02	1/3
HD	16.60	0.495±0.005	0.50±0.02	2/3
D_2	18.73	0.256±0.005	0.24±0.02	0
	First-freezing temperature (K)	16.49	16.42	15.72

Experimentally, the first-freezing temperature for the frozen mixture was 16.53 K and the mixture had completely frozen at ~16 K. This implies that complete fractionation does not occur in the mixture.

for extrapolating the D_2 concentration gradient present in a weakly absorbing 25:50:25% mixture of H_2, HD, and D_2 from more absorptive mixtures.

Another indication that significant fractionation does not occur in a H-D mixture is the thermodynamic properties of the solidification process. Each H-D mixture does not have a specific triple point but exhibits a first-freezing temperature and solidifies over a finite temperature range. First, consider the 25:50:25% mixture of H_2, HD, and D_2. The temperature at which the mixture begins to freeze (i.e., the first-freezing temperature) θ is given by

$$\theta = \sum_i \left(f_i \times T_{tp,i} \right), \tag{2}$$

where f_i and $T_{tp,i}$ are the molecular fraction and triple point of the i^{th} component, respectively. Values for this mixture are shown in Table 105.I. Molecular fractions in the table are based on both the pressurization schedule of the gas reservoir when the sample was prepared and on an independent measurement of the sample using cryogenic gas chromatography.[12] Experimentally, the first-freezing temperature for the mixture was 16.53 K and the mixture had completely frozen at ~16.1 K. This implies that complete fractionation does not occur in the mixture since the H_2 fraction would not have begun to freeze until 13.96 K. Indeed, if the D_2 had initially frozen out of solution, the remaining HD-H_2 mixture would not have begun to freeze until 15.72 K, well below the 16.1 K experimentally determined last-freezing temperature.

The first- and last-freezing temperatures were measured for each H-D mixture. As the temperature at the top of the sample was reduced, the highest temperature at the bottom of the sample at which crystallites began forming was recorded as the first-freezing temperature. Likewise, the highest temperature at the top of the sample at which the sample had completely frozen was recorded as the last-freezing temperature. The data points are shown in Fig. 105.33. This plot is indicative of a classic completely soluble isomorphous system.[13] Such behavior is not unreasonable since the chemical, and therefore crystallographic, nature of each isotope is identical.

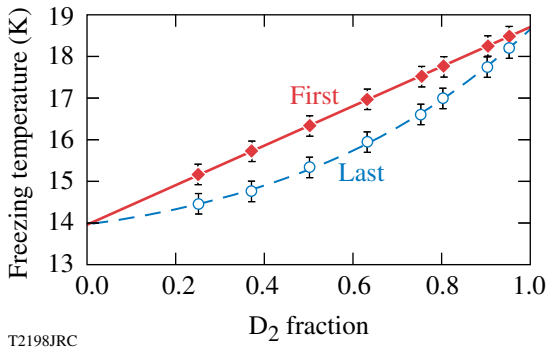

Figure 105.33
The experimentally measured first- and last-freezing temperatures (diamonds and circles, respectively) indicate that the H-D mixtures form a completely soluble isomorphous system. The upper line is from Eq. (2) and uses the known concentration of each mixture and the triple point of each molecule. The lower curve is a third-order least squares polynomial fit to the experimental data. The error bars indicate the ±50 mK uncertainty in the measured temperatures.

Conclusions

The average absorption coefficient of the D_2 in a H_2-D_2 mixture was measured as a function D_2 molecular fraction. The absorption coefficient varies exponentially with D_2 concentration. This is expected since the relatively large concentrations of D_2 in the H-D mixture used in this study deviate from the

low-concentration linear regime over which Beer's Law is valid. There was little separation of the isotopes during the solidification process. The maximum spatial concentration gradients are of the order of 0.02 to 0.05 molecular fraction per millimeter. The average D_2 concentration gradient (percentage) is greatest for the lowest concentrations. The absorption coefficient's gradient was also measured and appears to be inversely proportional to the cooling time, which may be indicative of solid diffusion. Thermodynamically, the mixtures form a completely soluble isomorphous system since the mixture solidifies over a finite temperature range for all concentrations. Possible fractionation during solid-to-vapor-to-solid mass transfer as a result of sublimation and refreezing will be investigated in a future study.

Another observation is that the absorption coefficient for deuterium in the 25:50:25% H_2:HD:D_2 mixture is nearly *twenty times lower* (0.017 mm^{-1} versus 0.317 mm^{-1} for pure D_2). This is attributed to the simultaneous transition absorption requirement of two neighboring D_2 molecules. Therefore, the interference of non-D_2 molecules between adjacent D_2 molecules makes the 3-mm-thick H-D mixture >96% transmissive even though one in four molecules is D_2. Compare this with a 40% transmission for a pure D_2 sample. This will greatly increase the time necessary to layer a D-T–filled capsule using IR-enhanced β-layering versus IR layering with pure D_2 using an IR laser tuned to the 3162 cm^{-1} absorption band of D_2.[14] One solution is to pump the DT molecule at 2888 cm^{-1}, the wave number for the peak absorption for DT.[15] In comparison to 25% D_2, DT makes up 50% of the D-T mixture and, extrapolating the data in Fig. 105.29 to similar behavior with DT concentration, will absorb significantly more IR radiation than the D_2 in the mixture.

Appendix

The Beer–Lambert Law takes on various forms: $A = \alpha' tc$, $I_t / I_0 = e^{-\alpha' tc}$, and $A = \log\left(I_0 / I_t\right)$, with $\alpha = \alpha' c = 4\pi k/\lambda$, where A is the absorbance, I_0 is the intensity of the incident light, I_t is the intensity after passing through the material, t is the distance that the light travels through the material (i.e., the path length), c is the concentration of absorbing species in the material (mole solute per mole solvent), α' is the molar absorption coefficient, α is the bulk absorption coefficient, λ is the wavelength of the light, and k is the extinction coefficient. In this treatment, since α is a strong nonlinear function of concentration, it will be used instead of the molar absorption coefficient.

The transmission data must be corrected to account for the change in reflectivity of the sample cell upon vaporization of the solid hydrogen sample. Incorporating Beer's Law above, the transmitted intensity I_t with the solid in the sample cell is given by

$$I_t = I_0 T_1^4 T_2^2 T_3^2 e^{-\alpha t},$$

where I_0 is the incident intensity, α is the absorption coefficient for the solid hydrogen, t is the sample thickness, and the transmittances T are for the interfaces given in Fig. 105.34. After vaporization,

$$I'_t = I_0 T_1^4 T_2^2 T'^{2}_{3};$$

now, let

$$T = \frac{I_t}{I'_t} = T_3^2 \frac{e^{-\alpha t}}{T'^{2}_{3}}.$$

Assuming nonabsorbing windows,

$$T_3 = \left(1 - R_3\right) \text{and } T'_3 = \left(1 - R'_3\right),$$

where

$$R_3 = \frac{\left(n_2 - n_3\right)^2}{\left(n_2 + n_3\right)^2} \text{ and } R'_3 = \frac{\left(n_2 - 1\right)^2}{\left(n_2 + 1\right)^2}$$

at normal incidence.

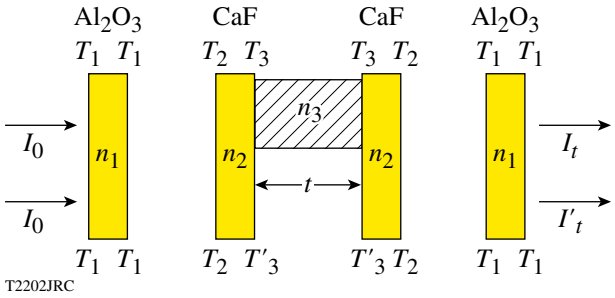

Figure 105.34
The attenuation of the sample beam as it passes through the sample cell with and without the solid hydrogen. Both the increase in absorption from the presence of the solid slab and the reduction in reflectivity at the internal boundaries of the cell's windows due to its presence must be accounted for to obtain an accurate absorption coefficient.

The refractive indices n are those shown in Fig. 105.34. Letting

$$\beta = \frac{(1 - R'_3)^2}{(1 - R_3)^2},$$

$$T = \frac{e^{-\alpha t}}{\beta} \text{ and } \alpha = -\frac{\ln(\beta T)}{t}.$$

Therefore, by measuring I_t and I'_t, taking their quotient T, and correcting it using $\beta = 0.964$ at $\lambda = 3.16\ \mu$m for these materials, the absorption coefficient can be measured.

ACKNOWLEDGMENT

This work was supported by the U.S. Department of Energy Office of Inertial Confinement Fusion under Cooperative Agreement No. DE-FC52-92SF19460, the University of Rochester, and the New York State Energy Research and Development Authority.

REFERENCES

1. P. W. McKenty, T. C. Sangster, M. Alexander, R. Betti, R. S. Craxton, J. A. Delettrez, L. Elasky, R. Epstein, A. Frank, V. Yu. Glebov, V. N. Goncharov, D. R. Harding, S. Jin, J. P. Knauer, R. L. Keck, S. J. Loucks, L. D. Lund, R. L. McCrory, F. J. Marshall, D. D. Meyerhofer, S. P. Regan, P. B. Radha, S. Roberts, W. Seka, S. Skupsky, V. A. Smalyuk, J. M. Soures, K. A. Thorp, M. Wozniak, J. A. Frenje, C. K. Li, R. D. Petrasso, F. H. Séguin, K. A. Fletcher, S. Padalino, C. Freeman, N. Izumi, J. A. Koch, R. A. Lerche, M. J. Moran, T. W. Phillips, G. J. Schmid, and C. Sorce, Phys. Plasmas **11**, 2790 (2004).

2. F. J. Marshall, R. S. Craxton, J. A. Delettrez, D. H. Edgell, L. M. Elasky, R. Epstein, V. Yu. Glebov, V. N. Goncharov, D. R. Harding, R. Janezic, R. L. Keck, J. D. Kilkenny, J. P. Knauer, S. J. Loucks, L. D. Lund, R. L. McCrory, P. W. McKenty, D. D. Meyerhofer, P. B. Radha, S. P. Regan, T. C. Sangster, W. Seka, V. A. Smalyuk, J. M. Soures, C. Stoeckl, S. Skupsky, J. A. Frenje, C. K. Li, R. D. Petrasso, and F. H. Séguin, Phys. Plasmas **12**, 056302 (2005).

3. P.W. McKenty and M.D. Wittman, Bull. Am. Phys. Soc. **50**, 115 (2005).

4. I. Prigogine, R. Bingen, and J. Jeener, Physica (The Hague) **XX**, 383 (1954); *ibid*. 516; *ibid*. 633.

5. M. Bienfait *et al*., Phys. Rev. B **60**, 11,773 (1999).

6. A. Crane and H. P. Gush, Can. J. Phys. **44**, 373 (1966).

7. J. Van Kranendonk, *Solid Hydrogen: Theory of the Properties of Solid H_2, HD, and D_2* (Plenum Press, New York, 1983), pp. 29–51.

8. L5004-IR Spectrometer System, Laser Components IG, Inc., Hudson, NH, 03051, September 2004, http://www.lasercomponents.com/wwwe/products/index.html (8 February 2006).

9. Displex Low Vibration/Mossbauer Cryostat, DMX-20 Interface, Advanced Research Systems, Inc., Macungie, PA, 18062, 2004, http://www.arscryo.com/dmx20.html (8 February 2006).

10. J. Van Kranendonk, *Solid Hydrogen: Theory of the Properties of Solid H_2, HD, and D_2* (Plenum Press, New York, 1983), pp. 105–129.

11. *ibid*. p. 119.

12. W. T. Shmayda, Laboratory for Laser Energetics, private communication (2005).

13. *Metals Handbook: Metallography, Structures, and Phase Diagrams*, 8th ed. (American Society for Metals, Metals Park, OH, 1973), p. 294.

14. G. W. Collins *et al*., J. Vac. Sci. Technol. A **14**, 2897 (1996).

15. D. N. Bittner, Shafer Corporation, private communication (2005).

Role of Hydrogen Fractionation in ICF Ignition Target Designs

Introduction

The need of using cryogenic hydrogenic fuels in inertial confinement fusion (ICF) ignition targets has been well established. Efficient implosion of such targets has mandated keeping the adiabat of the main fuel layer at low levels to ensure drive energies are kept at a reasonable minimum. In fact, it has been shown by many authors that the minimum drive energy of an ICF implosion scales roughly as the square of the fuel adiabat.[1–3] The use of cryogenic fuels helps meet this requirement and has therefore become the standard in most ICF ignition designs.

To date, most theoretical ICF ignition target designs have assumed a homogenous layer of deuterium–tritium (DT) fuel kept roughly at or just below the triple point. Such assumptions have lead to several promising ICF target designs[4–7] that have numerically demonstrated ignition and burn under a variety of illumination schemes. Recent work done at the Laboratory for Laser Energetics (LLE), however, has indicated the possibility that, as cryogenic fuel layers are formed inside an ICF capsule, isotopic dissociation of the tritium (T), deuterium (D), and DT can take place, leading to a "fractionation" of the final ice layer. Fractionation, as illustrated in Fig. 105.35, can lead to isolated areas of the ice layer that are either T rich or D rich. Under such circumstances, the performance and overall viability of previous ignition designs need to be examined.

Motivation

The possibility of isotopic dissociation leading to fractionation within cryogenic hydrogenic fusion fuels was first proposed by Prigogine[8] with initial experimental investigations carried out by Bienfait.[9,10] It is surmised that, because of the different triple point temperatures of the various constituent molecules (T_2, D_2, and DT), as a cryogenic layer is formed, the individual constituents freeze-out separately from the whole. As shown in Fig. 105.35, such a situation could lead to large volumes of the cryogenic layer being totally devoid of DT molecules. The significance of this can be understood when examining the thermonuclear reaction rates for these three molecules as a function of temperature, as shown in Fig. 105.36. The expected operating temperature for inertial confinement ignition target designs, as they approach the ignition threshold, is typically held to be in the 8- to 12-keV range.[11] As can be seen in Fig. 105.36, the reaction rates for both the T + T and

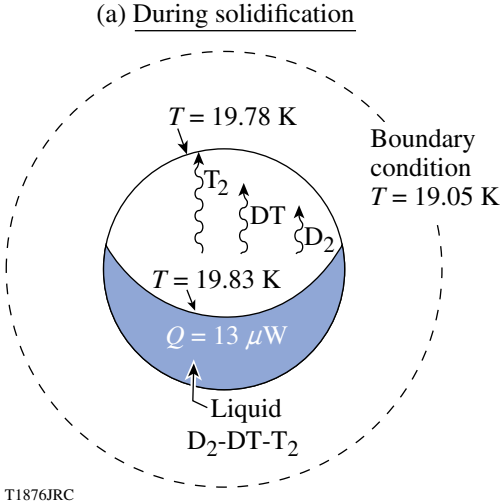

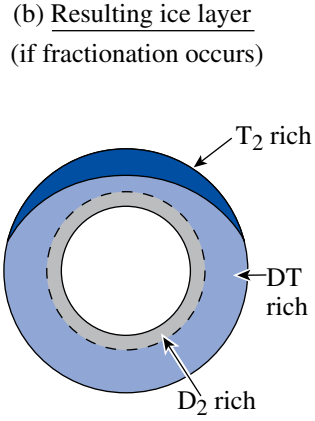

Triple point	Vap. press. (Pa) at 19.79 K
D_2 = 18.72 K	2930
DT = 19.79 K	2200
T_2 = 20.62 K	1580

Figure 105.35
(a) Fractionation of isotopic hydrogen mixtures can occur because of the variance in the triple point. (b) Such fractionation could lead to isolated fuel layers.

D + D reactions are several orders of magnitude lower than that for the D + T reaction.[12]

Several initial scenarios of fractionation, as illustrated in Fig. 105.35(b), considered complete separation of the constituents into unique and isolated regions of the cryogenic layer. The overall effect of the fractionation on target performance is then dependent on the preponderance and spatial deposition of the separated fusion-fuel molecules. Of particular note is the scenario in which the D_2 molecules are the very last species to solidify. Such a scenario is illustrated in Fig. 105.37(a), where a solid D_2 crust has formed on the inner surface of the ice layer. This is particularly damaging in that when a normal ignition experiment is assembling in preparation for ignition, a central hot spot is required to form at the very center of the target. The majority of the material in this hot spot is made up from the mass from the inner few microns of the ice layer, which, because of the large temperature present at the center due to viscous work, has ablated into the region. As the ablated material is heated, the need for large concentrations of fusing DT molecules and their fusion by-product alpha particles for the initiation of the ignition process is obvious.

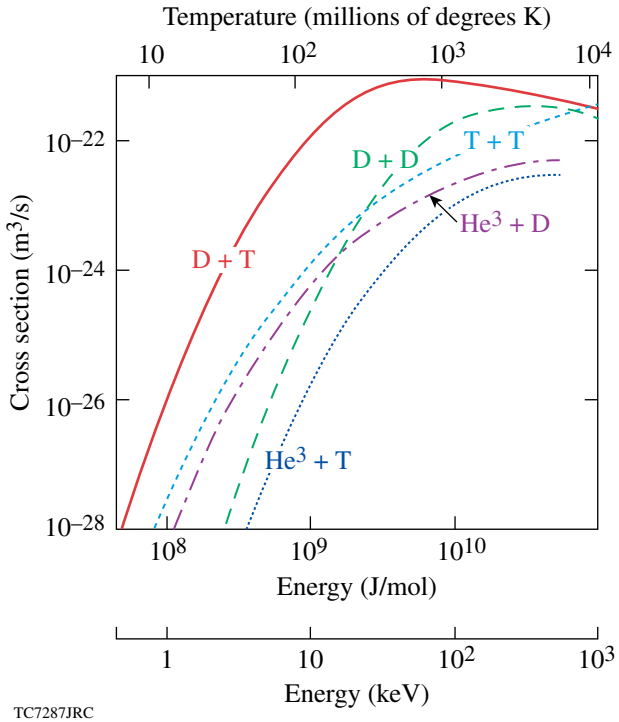

Figure 105.36
Thermonuclear cross sections for the five most easily activated fusion reactions indicate that DT fusion is the most easily obtained for ICF implosions. (Figure courtesy of the University of California/Lawrence Livermore National Laboratory.[12])

The effect of such a scenario on target performance can be quickly examined using the 1-D radiation-hydrodynamic computer code *LILAC*.[13] Several ignition implosion simulations were considered in which the inner surface of cryogenic DT fuel was replaced by solid D_2, as illustrated in Fig. 105.37(a). As shown in Fig. 105.37(b), as this inner layer increases in depth, target performance begins to degrade until eventually the target fails to achieve ignition. This behavior is due to the increasingly DT-depleted fuel that is being ablated into the hot-spot region, failing to produce the necessary alpha particle deposition in the cold, dense fuel surrounding the hot spot.

Another aspect of complete fractionation is the possible formation of a polar cap of pure T_2. Simulations of such scenarios require the implementation of a 2-D radiation-hydrodynamics computer code such as *DRACO*.[14,15] An extreme example of the effect of complete polar separation is given in Fig. 105.38(a).

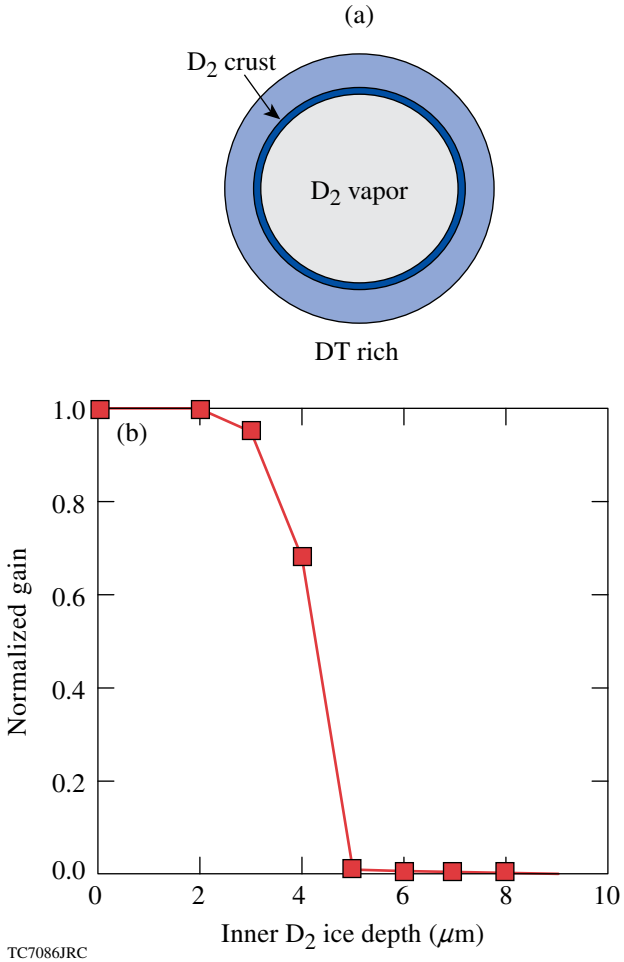

Figure 105.37
(a) Complete inner fractionation denies the ignition hot spot of the necessary tritium, which, (b) in abstenia, can preclude ignition.

Here we consider not only the formation of a northern pole cap of T_2 but, in addition, assume that a southern pole of pure D_2 has also formed. An isodensity plot of this target implosion taken at a time in the experiment after the thermonuclear blast wave has moved through the DT-rich part of the target in the equatorial regions is shown in Fig. 105.38(b). What is apparent in the density plot is that the polar regions of the target have not been able to participate in the burn because of the lack of DT. As such, while the burn wave has severely decompressed the equatorial regions, the polar caps have remained at very high densities because of the compressional nature of the ICF implosion. The overall performance of this design has suffered dramatically with the gain dropping from 45 to about 15. Results such as these clearly indicate the need to experimentally determine the possibility and overall extent of hydrogenic fractionation in ICF ignition capsules.

Experimental Setup

An experimental test bed to investigate the isotopic fractionation of fusion fuels was designed, built, and implemented at LLE, as illustrated in Fig. 105.39. The system was designed for use with nonradioactive isotopes and, as such, only examines fractionation scenarios involving H_2:HD:D_2 mixtures. We have investigated the possibility of fractionation using a deuterium–hydrogen (H–D) mixture with a similar isotopic ratio to the D–T mixture to be used in future cryogenic experiments

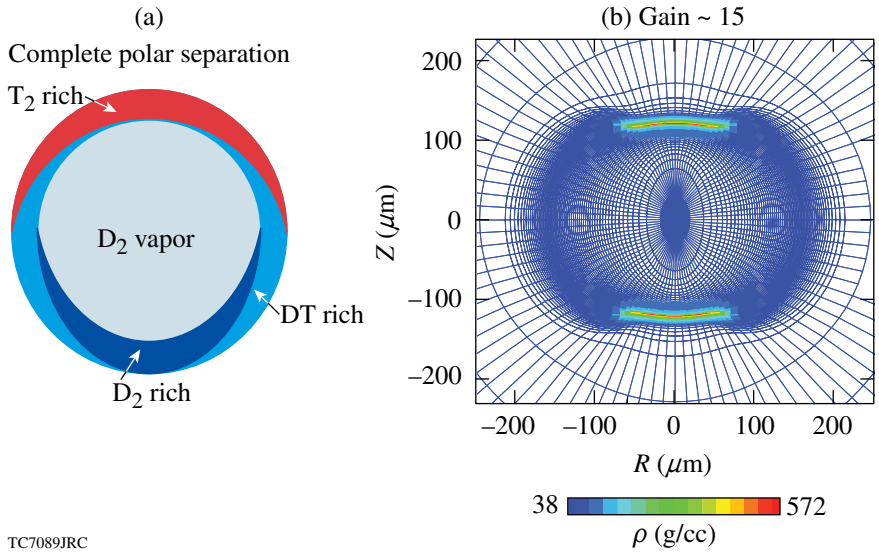

Figure 105.38
(a) A polar cap fractionation scenario exempts the DT-poor poles from the ignited burn, reducing the performance of a high-gain implosion. (b) High-density polar regions are evidence of nonburning fuel.

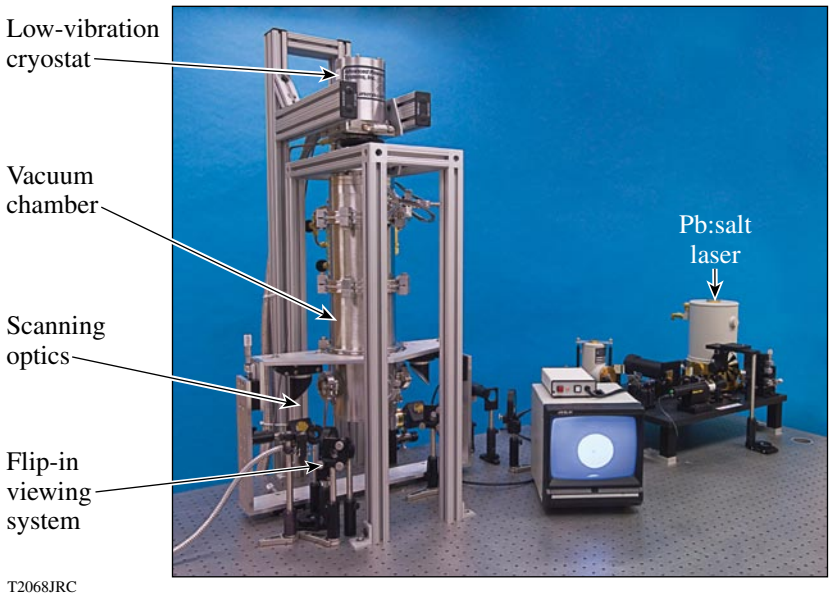

Figure 105.39
A H_2/HD/D_2 fractionation test bed is used to measure the IR absorption coefficient in a cryogenically solidified mixture.

(25% H_2, 50% HD, and 25% D_2) along with a slow-freezing protocol (–10 mK/h over a ~1-K range) that has been demonstrated to produce good-quality targets using the OMEGA Cryogenic Target Handling System. A focused beam from a Pb:salt laser tuned to the 3162 cm^{-1} absorption band of D_2 is raster scanned across a 6-mm-diam, 3-mm-thick sample of the mixture to determine the D_2 concentration as a function of position. This process was performed on samples that were solidified over several hours to several days to look for differences in fractionation due to diffusion of the different molecules to the liquid/solid interface as the sample was cooled.

Several mixtures of various H_2:D_2 ratios were examined in addition to the 25:50:25% H_2:HD:D_2 mixture. By plotting the absorption coefficient of the D_2 in the H–D as a function of the D_2 fraction in the mixture, the slope can be used to quantify a transmission gradient as a concentration gradient. The absorption coefficient for D_2 in a H–D mixture was found to be exponentionally dependent on the D_2 molecular fraction in the mixture, as illustrated in Fig. 105.40. From this, a maximum D_2 concentration gradient of 0.02 to 0.05 molecular fraction per millimeter was observed for the samples, as shown in Fig. 105.41. The average D_2 concentration gradient (percentage) is greatest for the 25% molecule fraction of D_2, which is representative of the 25:50:25% H_2:HD:D_2 mixture. The large error bars shown for the lowest concentrations indicate the signal-to-noise ratio in the measurement is smallest when the sample is the least absorptive.

Experimental Results

A complete and thorough discussion of the experimental results are presented earlier in this issue in **Isotopic Fractionation During Solidification of H_2–HD–D_2 Mixtures** on pp. 29–32. We have included a subset of this discussion to establish the relevant experimental initial conditions needed in the numerical modeling of fractionation.

Initial experiments focused on answering the question of whether or not complete fractionation, the situation where regions of pure, single isotopes freeze-out separately, occurs for these types of isotopes. Of particular interest was the experimentally observed, "first-freezing" (FF) temperature of a given cryogenic sample. The FF temperature is the temperature of the cryostat at which definitive crystal growth is observed. For pure samples or cases of complete fractionation, this would, of course, be the normal triple point of the material as given in Table 105.I on p. 32. Also given in the table are approximations for the FF temperature based on various models for the mass fraction of a given mixture. The FF temperature is calculated from a weighted sum of the product of the assumed isotopic mass fraction f_i and its appropriate triple point temperature $T_{tp,i}$ as given by

$$\sum_i f_i \times T_{tp,i}.$$

From this approximation one can see that the FF temperature for this mixture should lie in the range from 15.72 to 16.49 K. Additionally, the entire mixture should freeze-out into a layer when the FF temperature is reached and held constant.

The experiment was conducted and attention was focused on the mixture as the cryostat temperature approached the first triple point of the mixture constituents (deuterium) at 18.73 K. No appreciable crystal growth was observed. The same was true when the cryostat temperature reached and fell below the triple point of the HD molecule at 16.60 K. This experiment

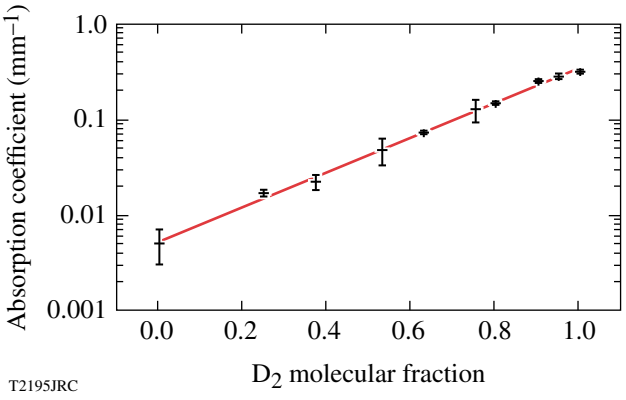

Figure 105.40
The average absorption coefficient of the D_2 in a H_2–D_2 mixture was measured as a function of the D_2 molecular fraction.

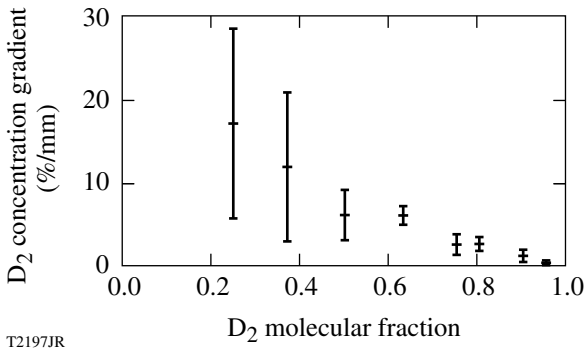

Figure 105.41
The average D_2 concentration gradient (percentage) is greatest for the lowest concentrations.

was repeated several times with the same results and indicates the absence of complete fractionation in cryogenic fusion fuels. As the experiment proceeded, it was only at a temperature of 16.53 K that appreciable crystal growth appeared. However, the entire sample did not freeze-out into a layer as the temperature was held constant. It was only after the cryostat temperature was further lowered to 16.10 K that total solidification of the mixture was observed. While the results from these experiments indicated that complete fractionation of cryogenic fuel layers does not take place, the differential temperatures required to freeze the entire sample did indicate the presence of low levels of fractionation within the mixture.

Additional experiments that examined the spatial dependence of the IR transmission coefficient of a cryogenic sample layered within the low-vibration cryostat were then carried out. As illustrated in Fig. 105.42, the experimental system recorded a spatial variation in the transmission coefficient of the cryogenic sample. Figure 105.42 also shows the singular transmission levels for pure H_2 and D_2 samples. From this image it is clear that fractionation has occurred within the cryogenic fusion-fuel layer. Interpretation of the variance in transmission indicates that fractionation levels in the sample are in excess of 5% from one side of the cell to the other and could in fact be as high as 10% overall.

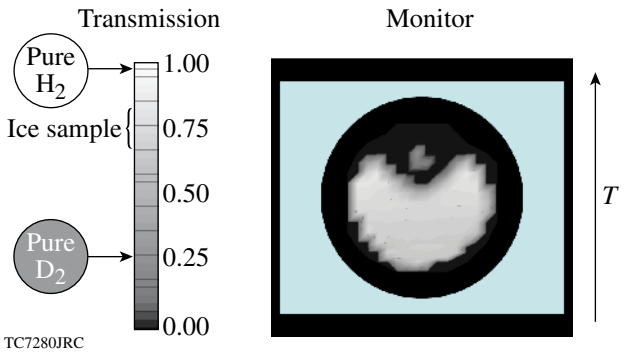

Figure 105.42
The absorption coefficient of the D_2 in the H/D mixture is less than 1/20th of that for pure D_2.

Numerical Results

A numerical fractionation scenario based on the above experimental results was constructed and studied. The particular metric investigated was the effect of the fractionation on target gain. Using the template illustrated in Fig. 105.43, the north polar fractionation within the target was numerically varied up to levels of 100%. As the level of fractionation was increased past ~30%, the increasing lack of DT at the poles of the target began disrupting the target performance. As can be seen in Fig. 105.44, this process can degrade target performance from a gain of 45 for perfect ice down to less than 10 for the cases with high levels of fractionation. For small levels of fractionation, the ignition and burn phases of the implosion proceed almost completely unaffected by the redistribution of the fusion fuel within the target. It is helpful to remember that in most ICF ignition designs the burnup fraction of fusion fuel is typically only in the 10%–15% range by molecule. As such, the target performance is relatively unaffected by small changes in the distribution of the fusion-fuel molecules. As was discussed earlier, however, as the amount of DT within a specific volume of the target is reduced, the likelihood of that region participating in the ignition burn wave is greatly diminished.

Another indication of how increasing fractionation perturbs target performance can be seen from a comparison of the

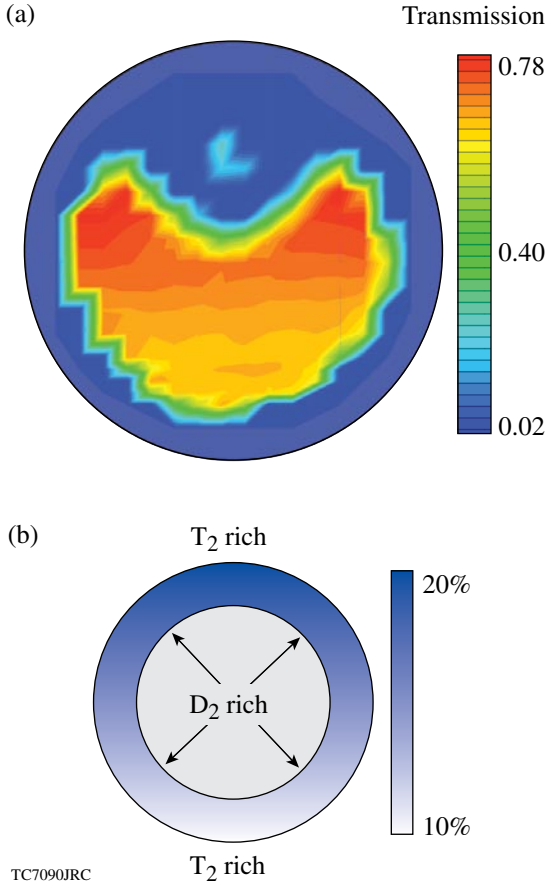

Figure 105.43
(a) Isotopic hydrogen (H_2/HD/D_2) fractionation in a solution has been observed in the laboratory at levels approaching 10%. (b) This information was used to construct a set of initial conditions for numerical studies of fractionation in ICF target designs.

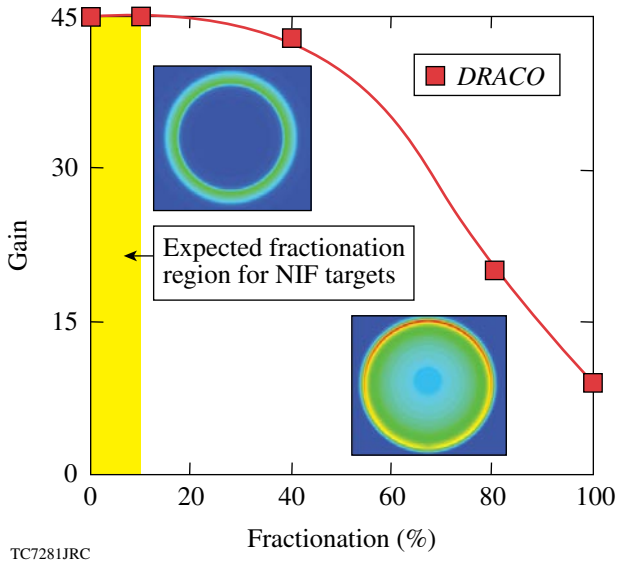

Figure 105.44
Fractionation levels in excess of ~30% are required before ignition target performance is affected. Current estimates place a 10% upper limit on the fractionation—too low to degrade target performance.

isodensity contour plots given as insets in Fig. 105.44. These contours, drawn on the same legend, demonstrate the symmetric decompression of the ice layer in the low fractionation cases. While similar decompression is apparent in the lower hemisphere of the high-fractionation case, the north polar region has remained at high compressed densities because of the region's inability to participate in the DT thermonuclear burn.

While the effects of high levels of fractionation on target performance are disturbing, the good news is that, given the experimental evidence to date, current estimates of the levels of fractionation in NIF ignition target designs are not expected to exceed 10%. As such, fractionation is not viewed as a major threat to the overall performance of ICF ignition design planned for experiments on the NIF, as illustrated as the shaded region of Fig. 105.44.

Conclusion

The need of using cryogenic hydrogenic fuels in ICF ignition target designs has been well established. Efficient implosion of such targets has mandated keeping the adiabat of the main fuel layer at low levels to ensure drive energies are kept at a reasonable minimum. To date, most theoretical ICF ignition target designs have assumed a homogenous layer of DT fuel kept roughly at or just below the triple point. However, recent work done at LLE has indicated the possibility that, as cryogenic fuel layers are formed inside an ICF capsule, isotopic dissociation of the T, D, and DT can take place, leading to a "fractionation" of the final ice layer. Fractionation studies of fusion-like fuels (H/HD/D) have demonstrated the existence of fractionation in ICF cryogenic fuel layers. However, numerical simulations of ignition target designs, using experimental fractionation scenarios, indicate that small levels of fractionation (~10%) are acceptable for ignition performance on the NIF.

ACKNOWLEDGMENT

This work was supported by the U.S. Department of Energy Office of Inertial Confinement Fusion under Cooperative Agreement No. DE-FC52-92SF19460, the University of Rochester, and the New York State Energy Research and Development Authority.

REFERENCES

1. R. Betti, K. Anderson, V. N. Goncharov, R. L. McCrory, D. D. Meyerhofer, S. Skupsky, and R. P. J. Town, Phys. Plasmas **9**, 2277 (2002).
2. M. C. Herrmann, M. Tabak, and J. D. Lindl, Nucl. Fusion **41**, 99 (2001).
3. A. Kemp, J. Meyer-ter-Vehn, and S. Atzeni, Phys. Rev. Lett. **86**, 3336 (2001).
4. T. R. Dittrich *et al*., Phys. Plasmas **5**, 3708 (1998).
5. P. W. McKenty, V. N. Goncharov, R. P. J. Town, S. Skupsky, R. Betti, and R. L. McCrory, Phys. Plasmas **8**, 2315 (2001).
6. A. J. Schmitt *et al*., Phys. Plasmas **11**, 2716 (2004).
7. J. L. Perkins and M. Tabak, Bull. Am. Phys. Soc. **49**, 61 (2004).
8. I. Prigogine, R. Bingen, and J. Jeener, Physica (The Hague) **XX**, 383 (1954); *ibid*. 516; *ibid*. 633.
9. M. Bienfait *et al*., Physica B **234–234**, 159 (1997).
10. M. Bienfait *et al*., J. Low Temp. Phys. **111**, 555 (1988).
11. J. D. Lindl, Phys. Plasmas **2**, 3933 (1995).
12. P. C. Souers, *Hydrogen Properties for Fusion Energy* (University of California Press, Berkeley, 1986). Figure courtesy of the University of California/Lawrence Livermore National Laboratory and the Department of Energy under whose auspices this work was performed.
13. M. C. Richardson, G. G. Gregory, R. L. Keck, S. A. Letzring, R. S. Marjoribanks, F. J. Marshall, G. Pien, J. S. Wark, B. Yaakobi, P. D. Goldstone, A. Hauer, G. S. Stradling, F. Ameduri, B. L. Henke, and P. Jaanimagi, in *Laser Interaction and Related Plasma Phenomena*, edited by H. Hora and G. H. Miley (Plenum Press, New York, 1986), Vol. 7, pp. 179–211.
14. D. Keller, T. J. B. Collins, J. A. Delettrez, P. W. McKenty, P. B. Radha, B. Whitney, and G. A. Moses, Bull. Am. Phys. Soc. **44**, 37 (1999).
15. P. B. Radha, V. N. Goncharov, T. J. B. Collins, J. A. Delettrez, Y. Elbaz, V. Yu. Glebov, R. L. Keck, D. E. Keller, J. P. Knauer, J. A. Marozas, F. J. Marshall, P. W. McKenty, D. D. Meyerhofer, S. P. Regan, T. C. Sangster, D. Shvarts, S. Skupsky, Y. Srebro, R. P. J. Town, and C. Stoeckl, Phys. Plasmas **12**, 032702 (2005).

Polar-Direct-Drive Simulations and Experiments

Introduction

Polar direct drive (PDD)[1] provides a viable path for direct-drive ignition on the National Ignition Facility (NIF).[2] Ideally, direct-drive ignition experiments require a symmetric arrangement[3–5] of high-powered UV laser beams pointed at the target center with focal spots that fill and overlap the spherical target surface. The NIF will be configured initially for x-ray drive, however, with the beams arranged around the polar axes to illuminate the interior of cylindrical hohlraums via entrance holes located at either end of the cylinder.[6] The PDD concept will enable direct-drive ignition experiments on the NIF while it is in the x-ray-drive configuration. Polar direct drive achieves uniform drive by repointing the beams, designing the on-target spot shapes with customized phase plates,[7,8] employing an optional CH ring that surrounds the equatorial region and acts as a plasma lens, refracting laser energy back toward the target (referred to as the Saturn target, see Ref. 9), and taking advantage of the NIF's flexible pulse-shaping capability.

The PDD concept is currently under experimental investigation on the OMEGA Laser System.[8] The goal of the experiments was to provide an understanding (both experimentally and through simulation) of the laser absorption characteristics resulting from repointing the beams and to test the ability to drive PDD implosions that obtain yields close to energy-equivalent symmetric-drive implosions. The common CH targets provide an adequate test bed for this purpose. (Surrogate cryogenic targets that scale to NIF designs are being planned for future experiments.) As shown in Fig. 105.45(a), a 40-beam subset of the 60-beam OMEGA laser has been chosen to emulate the NIF x-ray-drive configuration. Both the standard PDD and Saturn target designs utilize the OMEGA laser in this 40-beam configuration. Figure 105.45(b) illustrates how the beams are repointed for OMEGA PDD experiments. The Saturn target[9] employs an equatorial CH ring to refract laser energy from the obliquely pointed beams toward the target equator. Radiation from the CH ring also plays a role in driving the equator. The initial simulation and evaluation of these experiments was performed using the hydrodynamics code *SAGE*.[10] Present work uses the hydrodynamics code *DRACO*,[11] an arbitrary Lagrangian Eulerian (ALE) code that includes both radiation transport and fusion particle production and transport as well as a full 3-D laser ray-trace deposition package. *DRACO* can also be configured to run in a sliding-grid Eulerian mode (which is necessary to simulate the Saturn targets to support the shock transit in the space between the CH ring and the target).

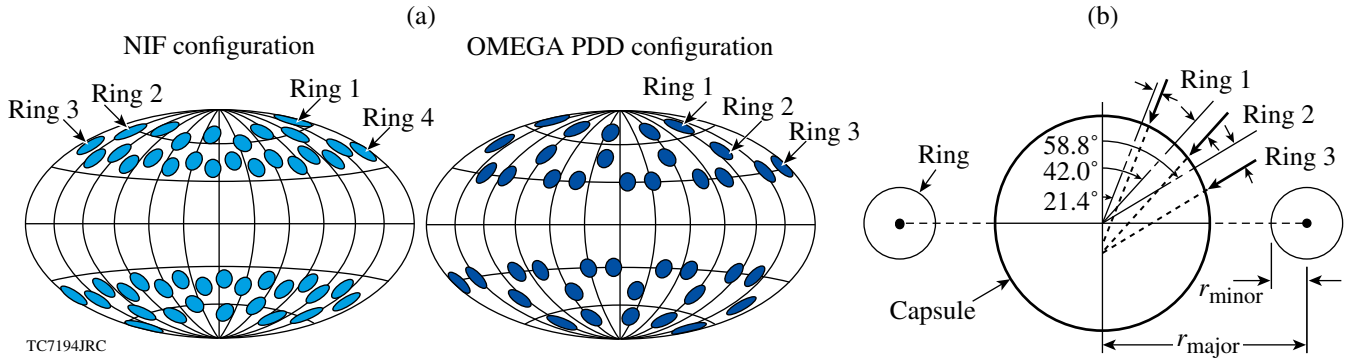

Figure 105.45
(a) Illustration of beam port positions for the NIF and OMEGA indirect-drive configurations. A 40-beam subset of the 60-beam OMEGA Laser System emulates the NIF indirect-drive configuration. (b) The beam pointing schemes described in this paper for the OMEGA PDD program. Rings 1 and 2 (each hemisphere) have five beams each, while Ring 3 (each hemisphere) has ten beams for a total of forty beams. All beams in a ring are offset in the far-field plane perpendicular to the central beam axis (as indicated by the thin arrows) by the amount shown in Table 105.II. The placement of the Saturn ring is also indicated (not to scale).

In **OMEGA Experiments and Simulations** (p. 42), OMEGA PDD experiments and simulations are presented and compared for both types of PDD targets. The *DRACO* simulations of the OMEGA experiments presented here analyze the low-ℓ-mode behavior due to beam overlap and the increased refractive losses due to repointing the beams toward the equator. The angular resolution used in these simulations was 80 zones over a 90° wedge; the low-ℓ-mode structure up to mode $\ell = 22$ is adequately resolved. (Note: there is only significant power in modes up to $\ell = 6$.) The long-wavelength effects of energy balance and beam mispointing as well as the short-wavelength behavior of single-beam nonuniformity are currently under investigation. Good agreement is found by comparing x-ray framing-camera images with *DRACO* simulations. These implosions were all simulated in the sliding-grid Eulerian mode to make a consistent comparison with the Saturn simulations that require Eulerian hydrodynamics.

In **NIF Simulations** (p. 46), substantial gain is predicted with NIF-scale, 2-D *DRACO* implosion simulations. The simulated standard PDD targets consist of cryogenically layered deuterium–tritium (DT) encased with a wetted hydrocarbon (CH) foam[12,13] and a thin CH overcoat layer. The *DRACO* simulations for the NIF also included the effect of the low-ℓ-mode behavior due to beam overlap and repointing and were simulated in the ALE mode. For 1.36 MJ of laser energy, the PDD target gives a gain of 20. In comparison, the gain is 33 if the same target is driven symmetrically with 1.0 MJ of laser energy. The compressed core near stagnation consists of a 40-μm-radius, 10-keV region with a neutron-averaged ρr of 1270 mg/cm^2. The importance of maintaining both shell and shock-front uniformity is stressed.

OMEGA Experiments and Simulations

Experimental confirmation of 2-D *DRACO* hydrodynamic simulations has been obtained by making comparisons with PDD implosions[14] carried out on OMEGA. The implosions were performed with a nominal room-temperature target consisting of 865-μm-diam, 19.7-μm-thick (experimental average) glow-discharge polymer shells filled with D_2 gas at a pressure of 15 atm. This type of target has been used extensively on OMEGA.[10,15–17] All capsules were coated with 500 Å of Al to act as a gas retention barrier and are held in place by 17-μm boron fibers glued to the target surface. (Note that the Al layer and boron fibers were not simulated.) The capsule diameters were measured to an accuracy of 1 μm and the shell thickness to 0.2 μm. The Saturn targets reported here consisted of the same capsule supported by three 10-μm-diam alumina "spokes" (which were not simulated), again glued to the target surface, inside a CH ring of circular cross section with a 1.1-mm major radius and a 150-μm minor radius (shots with a 1.25-mm major radius were also measured but not simulated). The laser drive was a 1-ns flat pulse with ~390 J per beam employing 1-THz, 2-D smoothing by spectral dispersion[18–21] with polarization smoothing.[17] The 40 OMEGA beams were repointed for PDD with a typical accuracy of 15-μm rms using the technique described by Forties and Marshall (Ref. 22). Figure 105.45(b) depicts the beam-pointing scheme used for the experiments and simulations described in this work. Table 105.II details the configurations, giving the lateral offsets from the central beam axis in the far-field plane for three different cases. Figure 105.45(b) also indicates the placement of the Saturn ring.

Table 105.II: PDD offsets, Δr (μm)

	Case	Ring 1	Ring 2	Ring 3
A	Shot 38502 Shot 39281	90	120	120
B	Shot 34669	91	188	196
C	Proposed	74	61	180

As in Refs. 10 and 14, the imploding targets were diagnosed by framed x-ray backlighting. The framing cameras were configured to operate at a magnification of 6 with 10-μm pinholes and an effective resolution of ~11 μm. Each frame's integration time was ~50 ps and the absolute time of a frame was determined by noting the time of backlighter onset (known to be better than 10 ps). Au backlighters were used with a broadband emission ranging from 2.2 to 2.5 keV. Two backlighters were available, one viewing the target from just below the equator ($\theta_{va} = 101°$) and one well above the equator ($\theta_{va} = 63°$). The latter provided a view of the partially imploded plasma even in the presence of a Saturn ring. The delay of the backlighter beams was +0.9 ns relative to the beginning of the laser pulse. All beams used the same 1-ns flattop pulse shape with 100-ps rise and fall times. Peak power occurred from 0.1 ns to 1.0 ns. Backlit radiographs were obtained after the end of the drive pulse (~1.1 ns to 1.7 ns). Stagnation occurs around 1.9 ns.

X-ray radiography was used to measure the magnitude of deviations from spherical symmetry. Early in time, the deviations from sphericity are small and the streaked and framed x-ray imaging shows that the shell trajectory closely matches the predictions of 1-D simulations.[10] Later in time, however, the deviations become larger and increasingly important. The evolution of the shell distortion can be seen in Fig. 105.46(a), where three backlit framed x-ray images taken at times t = 1.23, 1.49, and 1.68 ns are shown for OMEGA shot 38502

(19.6-μm CH shell thickness), as viewed from the angle θ_{va} = 101°. This shot utilized the pointing intended for a Saturn target (case A of Table 105.II) but the target was shot without the external CH ring; therefore, strong distortions were expected around the equatorial plane where the target was underdriven. The *DRACO* simulation of this experimental shot was post-processed with the code SPECT3D (Ref. 23) to simulate an x-ray backlighter at the same viewing angle. The *DRACO*/SPECT3D-simulated x-ray radiograph results of shot 38502 are shown in Fig. 105.46(b) at times corresponding to the experimental images. Both the size and shape of the simulated radiographs are close to those observed.

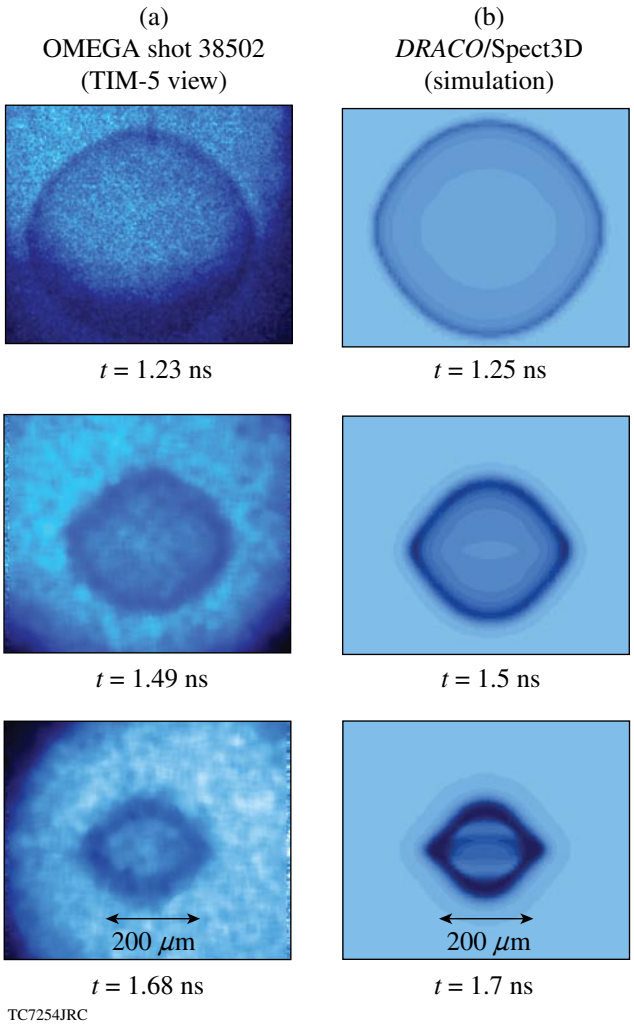

Figure 105.46
(a) Experimental x-ray framing-camera images. The dark rings (minimum x-ray transmission) indicate the evolution of the shell distortion. The times t = 1.2, 1.5, and 1.7 ns are shown for a standard PDD target on OMEGA for shot 38502. (b) Simulated x-ray radiographs at corresponding times produced from *DRACO* simulations that have been post-processed by SPECT3D. Note that the pointing used for this shot is intended for a Saturn target. The radiographs are imaged from TIM-5 at θ_{va} = 101°.

To provide a quantitative comparison between simulations and experiments, the locations of the x-ray radiograph minima of an OMEGA experiment and the simulated x-ray radiograph from a *DRACO*/SPECT3D simulation can be plotted [as a function of angle (θ') from the vertical image axis]. The x-ray radiograph minima of OMEGA shot 38502 at the viewing angle θ_{va} = 63° as a function of angle (θ') are shown in Fig. 105.47(a) (circles) taken at 1.68 ns, which was extracted from the x-ray radiograph shown in Fig. 105.47(b). The typical error in determining the position of the minimum is ±2 μm, as indicated by the example error bar in Fig. 105.47(a).

The data points extracted from a simulated radiograph are sufficiently smooth that they are well represented by a Legendre polynomial fit. These data are also extracted with

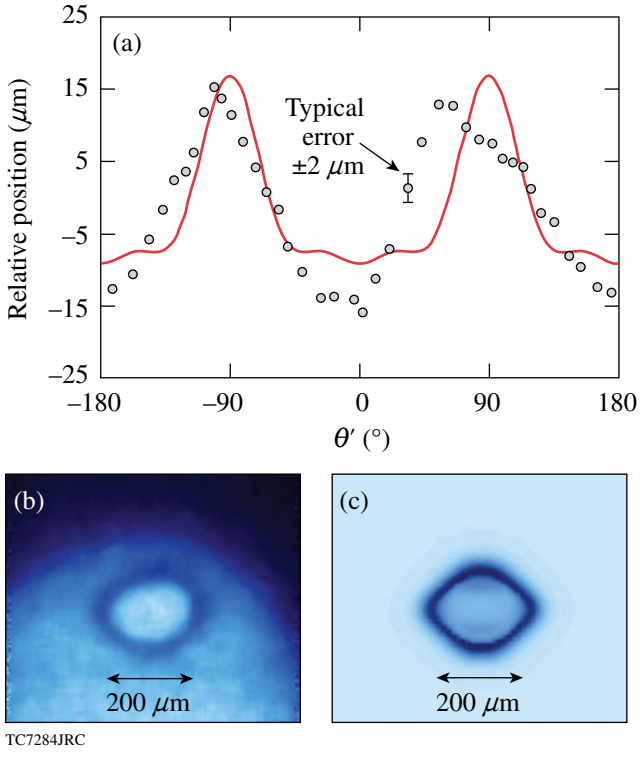

Figure 105.47
(a) The radii of the x-ray transmission minimum as a function of image polar angle (θ') are shown for OMEGA standard-PDD shot 38502 as circles at 1.68 ns relative to a radius of 93.1 μm. A Legendre polynomial fit to the simulated radiograph data is displayed as the black line at 1.7 ns relative to a radius of 94.3 μm. The peak-to-peak deviations are 15 μm for the experimental data and 13 μm for the *DRACO*/SPECT3D simulation. (b) The experimental and (c) simulated radiographs. The radiographs are imaged at θ_{va} = 63°.

an error of ±2 μm. Since the imploding shells are observed at an angle to the symmetry axis, it is necessary to transform the image's polar angle into the natural coordinates of the Legendre modes, viz.

$$\cos(\theta) = \cos(\theta')\sin(\theta_{va}), \tag{1}$$

where θ is the polar angle of the spherical coordinate system aligned with the target pole and θ_{va} is the viewing angle used in the experiment. The Legendre decomposition over the first six modes is given by

$$R_{\exp}(\theta') = \sum_{l-1}^{6} A_l \cdot P_l[\cos(\theta)], \tag{2}$$

where P_l is the Legendre polynomial of order l. This fit approximates the shape of the radiograph to that of a cut through an idealized thin shell. No significant modes above $\ell = 6$ were found, so only the fits up to 6 were included. A Legendre polynomial fit to the transmission minima from the *DRACO*/SPECT3D-simulated x-ray radiograph [Fig. 105.47(c)] is found and plotted in Fig. 105.47(a) (thick line) for the simulation time of 1.7 ns. The peak-to-peak deviations are 15 μm for the experimental data and 13 μm for the *DRACO* simulation.

The framed x-ray radiographs for a Saturn target taken at times t = 1.21, 1.46, and 1.65 ns for OMEGA shot 39281 (19.7-μm shell thickness) are shown in Fig. 105.48(a) with the same beam pointings (case A of Table 105.II). *DRACO*/SPECT3D-simulated x-ray radiographs are shown in Fig. 105.48(b) at similar times. Lineouts as a function of θ', similar to those of Fig. 105.47(a), are shown at ~1.65 ns in Fig. 105.49 with the experimental data as circles and the *DRACO*/SPECT3D data as a solid line. The peak-to-peak deviations are 10 μm for the raw data and 9 μm for the *DRACO* simulation. The effect of the external CH ring is readily observed by noting that the equatorial bulge around the equator has been decreased [compare Figs. 105.46 and 105.48 and Figs. 105.47(a) and 105.49] because of increased laser-energy deposition and radiation from the CH ring, which together increase the drive in the equatorial region.[10]

Saturn targets have obtained the best experimental yields to date relative to energy-equivalent, 60-beam symmetrically driven targets. The measured DD neutron yields for both types of PDD targets (standard and Saturn) and, for comparison, the yields obtained from symmetrically irradiated targets (60 beams with an equivalent on-target energy of 15.3 kJ) are

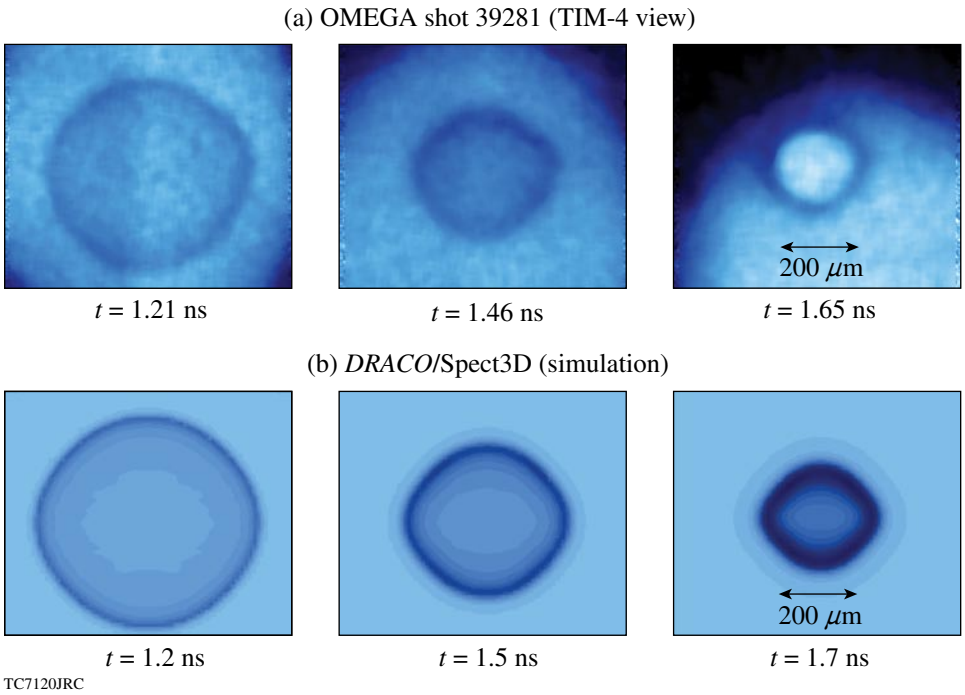

Figure 105.48
(a) Experimental x-ray framing-camera images indicating the evolution of the shell for a Saturn target on OMEGA shot 39281 at times t = 1.2, 1.5, and 1.7 ns. (b) Simulated x-ray radiographs using *DRACO* and SPECT3D. The radiographs are imaged at θ_{va} = 63°.

shown in Fig. 105.50. The standard targets obtained ~35% of the symmetric target yields. The spoke-mounted Saturn targets obtained about 75% of the symmetric target yields. The *DRACO*-simulated yield for the energy-equivalent symmetric-drive shot 34644 (19.6-μm shell thickness) was 2.91×10^{11} DD neutrons. This compares to the simulated yields for the standard PDD shot 34669 (19.3-μm shell thickness) and the Saturn shot 38291, 1.28×10^{11} and 1.73×10^{11} DD neutrons, respectively. The normalized yield results for two shots are summarized in Table 105.III. The Saturn target simulation yield increased relative to the standard PDD target but only by 34%, from 44% to 59%, whereas the experimental yield doubled (when comparing the standard PDD to the Saturn target).

Standard PDD targets can benefit from further optimization of pointing, spot shapes, and ring energy balance to produce results comparable to the current Saturn target designs. The benefit of finding an optimized standard-PDD design is the ability to fabricate and shoot a cryogenic PDD target. The Saturn design is not practical for cryogenic targets. For the sake of comparison, a warm CH target is used here since current experimental and simulated results exist. The current pointings used for standard PDD (case B in Table 105.II) were chosen on the basis of the existing phase plates on OMEGA (super-Gaussian of order 3.7). An optimization algorithm (separate from *DRACO*) was run that automatically tunes the beam pointing and spot shapes for equal energy beams, given an absorption angular spectrum extracted from a *DRACO* simulation under similar conditions. Different results will be

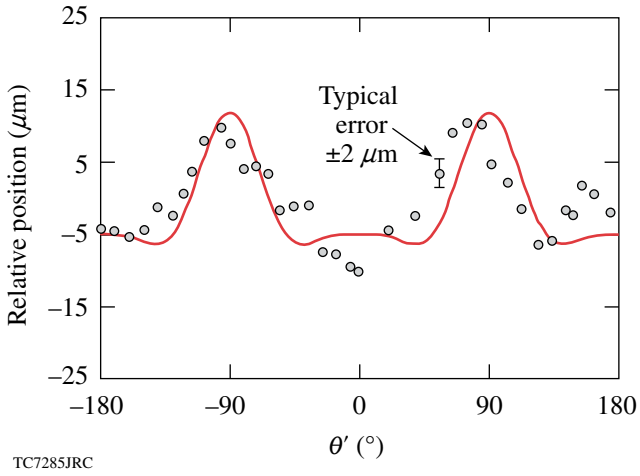

Figure 105.49
The radius of the x-ray transmission minimum as a function of image polar angle (θ') extracted from the 1.65-ns (right-hand) image of Fig. 105.48(a), shown as circles, relative to a radius of 101.7 μm. A Legendre polynomial fit to the simulated radiograph data extracted from the 1.7-ns (right-hand) image of Fig. 105.48(b) is displayed as the solid line relative to a radius of 106.6 μm. The peak-to-peak deviations are 10 μm for the experimental data and 9 μm for the *DRACO* simulation.

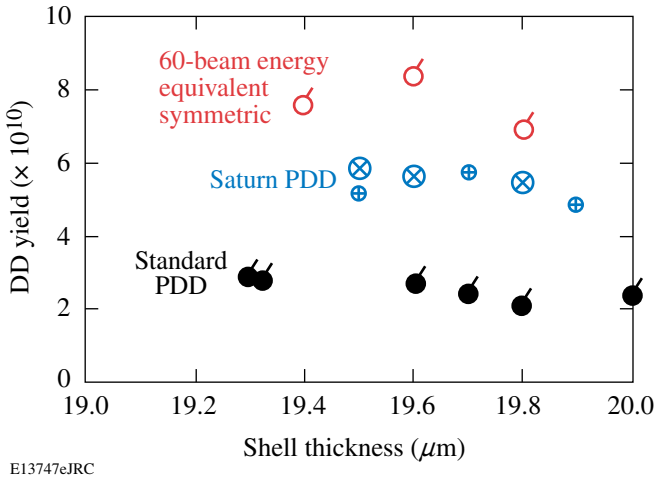

Figure 105.50
The measured DD neutron yields for both types of PDD targets (standard and Saturn) and, for comparison, the yields obtained from symmetrically irradiated targets (60 beams with the same on-target energy of 15.3 kJ). The standard-PDD targets obtained ~35% of the symmetric target yields. The Saturn targets obtained about 75% of the symmetric target yields. All shots employed a 1-ns flattop pulse with 100-ps rise and fall times. All PDD targets used optimal beam pointing ("A" of Table 105.II for Saturn, "B" for standard PDD). The Saturn shots with different major diameters are as indicated on the plot; the small symbols correspond to $r_{major} = 1100$ μm and the large symbols correspond to $r_{major} = 1250$ μm.

Table 105.III: Normalized experimental and simulation yields. The experimental yields are normalized to the energy-equivalent symmetric-drive experiment for shot 34644. The simulation yields are normalized to the simulation of the energy-equivalent symmetric-drive simulation.

	Standard PDD shot 34669	Saturn shot 39281 spoke mount
Experimental yield normalized to symmetric shot 34644	0.35	0.69
Simulation yield normalized to simulation of symmetric shot 34644	0.44	0.59

obtained by making alternate choices of sampled absorption spectra. The nonuniformity during the acceleration phase plays an important role for the long-wavelength distortions characteristic of PDD, especially when the laser energy is absorbed farther away from the critical surface around the equator. For this reason, the angular dependent absorption is taken during the acceleration phase at ~700 ps with the assumption that it is representative of the most influential period. The optimization process first overlaps the beams onto a hard sphere while accounting for the angular dependence of absorption. The spot shapes are changed and also repointed to minimize the nonuniformity of the absorbed energy profile on the surrogate target sphere. The resultant pointing for the different beam rings is 74, 61, and 180 μm. The resulting spot shapes are super-Gaussians of orders 2.58, 2.11, and 2.42, respectively, with 5% intensity contours located at 1.05× the target radius. Optimal PDD designs tend toward lower super-Gaussian orders because the narrower intensity peaks give the rings more independent control, particularly in the troublesome equatorial region; e.g., more energy can be delivered to the equator with minimal influence on the rest of the target. Additionally, the spot shapes are modulated by an order-10 super-Gaussian envelope with a 5% intensity contour at the target radius to maximize the energy delivered to the target (especially by minimizing the over-the-horizon energy near the equator). The energy of the first ring was derated by 15% to prevent overdrive in the polar region; as a consequence, the incident laser energy is only 14.8 kJ. The simulated absolute yield for this proposed configuration is comparable to that of the Saturn design (using 15.6 kJ of laser energy), and the symmetry of the shell is very similar, as shown in Figs. 105.51(a) and 105.51(b). It is expected that the shell symmetry can be improved by further tuning the beam repointing and spot shapes. The yields relative to the simulation of the energy-equivalent symmetric-drive target are 59% and 58%, respectively.

NIF Simulations

Cryogenic, DT-filled, wetted CH-foam targets show great promise for high PDD gains on the NIF.[24] The four rings of beams in the NIF indirect-drive configuration shown in Fig. 105.45(a) are repointed into three rings which are logically grouped by the angle in which the beam centers intersect the initial target radius; they are designated as polar, midlatitude, and equatorial rings. The polar and midlatitude rings are typically not repointed by a significant amount, whereas the equatorial ring is repointed the most, amounting to a transverse shift in the far-field plane of ~850 μm.

A successfully igniting PDD target requires that both shell and shock-front uniformity be maintained at a high level throughout the drive pulse. The equator experiences the highest incident angles, which lead to higher refractive losses and lower hydrodynamic efficiency, 2-D effects such as lateral mass and heat flow become important, and the relative pointing changes as the critical surface moves inward. The shell uniformity can be compromised because of the dynamic nature of the low-ℓ-

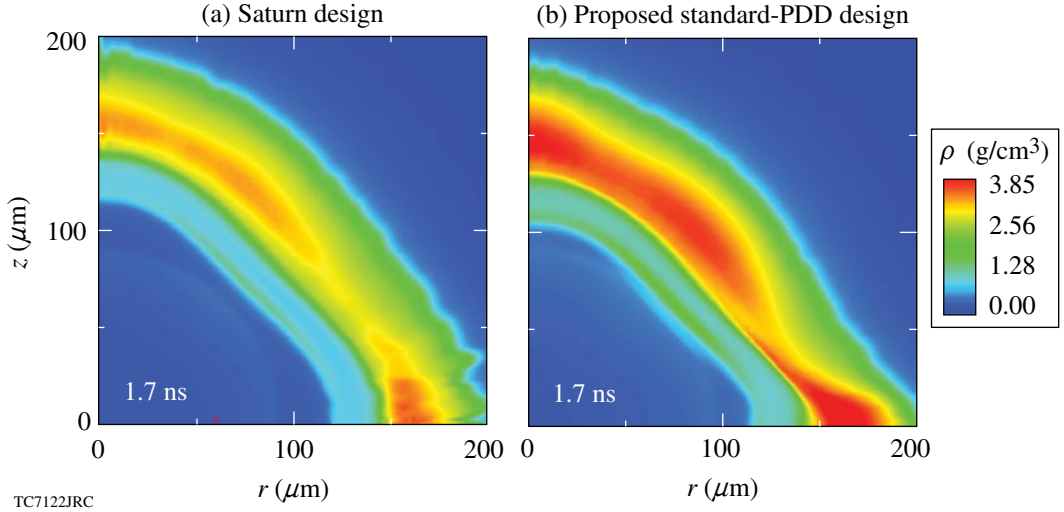

Figure 105.51
(a) The mass density for the OMEGA Saturn configuration near stagnation at 1.7 ns. (b) The mass density for the proposed OMEGA standard PDD configuration at 1.7 ns and the same distance traveled. The yields relative to the simulation of the energy-equivalent symmetric target are 59% and 58%, respectively. The axis of symmetry is along the vertical axis; i.e., the pole is pointing upward.

mode distortions inherent in the PDD setup. Their effect can be controlled, however, through sufficient overall drive uniformity. The uniformity can be optimized through beam pointing, spot shape designs, and time-dependent pulse shaping. The energy deposited near the equator must be increased to compensate for the higher refractive losses (lower energy absorption) and lower hydrodynamic efficiency (due to the laser energy being deposited farther out in the corona). This can be accomplished by using elliptical spot shapes and/or higher power in the equatorial rings.[25] The level of shock-front uniformity determines the symmetry of the shock-heated core and cannot be ignored. An improperly timed shock front can cause a design to fail because of a small and distorted shock-heated hot spot, whereas small adjustments during the foot pulse can make the same target ignite by developing a large and minimally distorted hot spot.

The NIF PDD target presented here is based on a 1.0-MJ, symmetric-drive, cryogenic, DT-filled, wetted CH-foam target with a thin CH overcoat that obtains a gain of 33. The interior DT vapor layer is 1380 μm in radius. The cryogenic DT ice layer is 180 μm thick. The wetted CH-foam layer is 70 μm thick and is modeled by a uniform mass density of 0.392 g/cm^3. A thin CH layer overcoats the target and is 1.2 μm thick. The 1.0-MJ pulse shape used for this target is plotted in Fig. 105.52(a).

For the *DRACO* simulation of the cryogenic, DT-filled, wetted CH-foam target reported here, all the rings have the same primary spot shape: a low super-Gaussian order of 2.2. A secondary elliptical super-Gaussian of the same order is superimposed on the equatorial beams. It has an ellipticity of 5, a relative strength (compared with the primary spot shape) of around 0.45, and a relative shift of 0.15 times the initial target radius. An equation for the composite equatorial spot can be written as

$$I_{\text{eq}} = e^{\alpha\left(x^2+y^2\right)^{\text{sg}/2}} + 0.45e^{\alpha\left\{\left[5\left(x-0.15\,r_t\right)\right]^2+y^2\right\}^{\text{sg}/2}}, \tag{3}$$

where $\alpha \equiv \ln(0.05)/r_t^{sg}$, sg $\equiv 2.2$, and r_t is the initial target radius. The secondary ellipse increases the energy deposition near the equator.

Beam repointing, spot shapes, and the relative pulse strengths of the different beams determine the in-flight shell uniformity. Initial guesses of the spot positions and the spot shapes are found off-line from *DRACO* using the same optimization technique mentioned in the previous section. Fine-tuning of the beam pointing takes place by running further *DRACO* simulations. The repointings used for the simulations presented here are 23.5°, 44.5°, and 80° for the polar, midlatitude, and equatorial rings, respectively.

An active pulse-shape optimization process internal to *DRACO* is then invoked to determine the relative pulse strengths at each ring by minimizing shell nonuniformity throughout the simulations. The optimized pulse shapes divide roughly into two separate temporal regions: the foot and the main drive. During the foot, the conduction zone is relatively uniform and does not require a large amount of compensation near the equator for a drive similar to the pole. Thus, the relative strengths between the ring pulse shapes are not very dif-

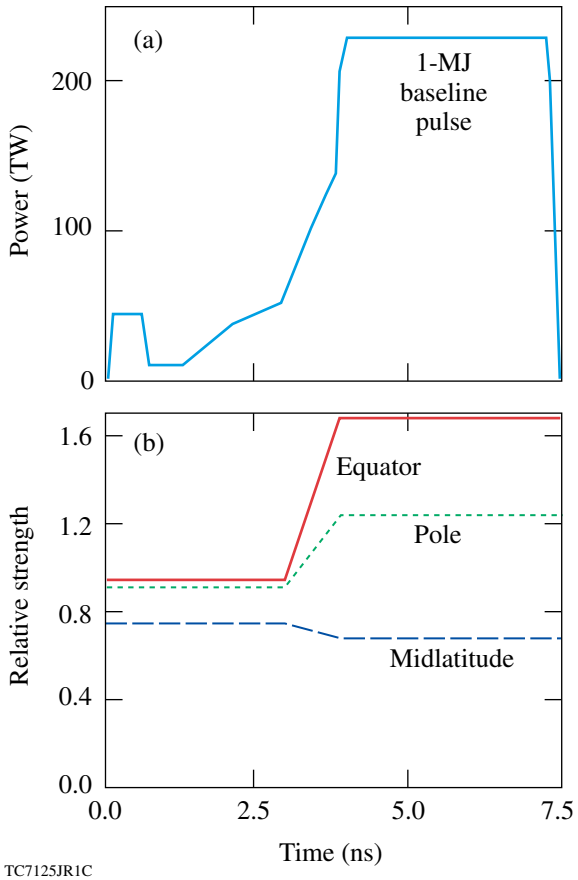

Figure 105.52
(a) Baseline 1.0-MJ pulse designed for a symmetrically driven NIF target. (b) Time-dependent multipliers giving the relative strengths of the three rings of beams (pole, midlatitude, and equator) in a standard PDD configuration. The three PDD pulses (baseline pulse multiplied by the relative strengths) represent 1.36 MJ overall.

ferent. (Fine-tuning for the shock front will still be required.) As the main pulse ablates the shell at a higher rate, however, the conduction zone becomes progressively nonuniform with the greatest standoff distance (separation distance between the energy deposition region and the ablation surface) occurring near the equator, and, consequently, the relative strengths between the ring pulse shapes are different with the most power given to the equatorial ring. The pulse shapes are then smoothed and fine-tuning takes place by adjusting the relative strengths after observing the shell and shock-front distortions during *DRACO* simulations. The main trend of the optimized pulse shapes increases the power in the equatorial beams relative to the other beams during the main drive. The smoothed pulse shapes vary continuously, which makes it difficult to adjust the relative factors between the different pulse shapes for each ring. It is found that using constant relative strengths in the foot that change to new constant factors during the main drive is adequate to tune the pulse shapes. The constant relative strengths in the foot and main drive sections of the pulse are initially chosen as the average value of the optimized pulses in each separate period. The constant relative strengths in the two sections of the pulse are independently adjusted to fine-tune the shell and shock-front uniformity.

Maintaining both the shell and shock-front uniformity is critical to obtaining substantial gains. Correcting only for the shell distortions can have a detrimental side effect of distorting the shock front. If the shock front is distorted, nonuniform shock heating produces a misshaped and small hot spot (defined here as the 10-keV temperature contour, which does not necessarily reflect the uniformity of the shell), leading to a failed target. The shell can have adequate uniformity at stagnation but with a severely distorted and small hot spot. When compared to a simulation that ignites, the 10-keV hot spot is large and conformal to the shell.

The application of this design process is given here for an igniting NIF PDD target with the parameters given in the beginning of this section. The symmetric-drive target and 1.0-MJ baseline pulse in Fig. 105.52(a) are used as a guide for tuning the ring pulse shapes by requiring that the shell trajectory matches that of the symmetric case as close as possible. In addition, the shock-front uniformity must be high enough to produce a large hot spot. The constant multiplication factors of each of the three rings resulting from the optimization algorithm described above are calculated first based on the optimized spot shapes and ring repointings found outside of *DRACO*. Then the constant factors in the main pulse are adjusted to closely match the trajectory of the symmetric-drive case while also obtaining the best overall low-ℓ-mode shell uniformity. Since only the pulse strengths of the three rings can be adjusted, a limited range of ℓ modes can be controlled (typically $\ell \leq 8$). Once the shell uniformity is tuned, the relative shock strengths are tuned using the foot portion to improve the shock-front uniformity. The shell uniformity is not greatly affected by the typical adjustments needed during the foot to compensate for shock-front distortions. By this point the shock front has roughly the same symmetry as the shell but still needs improvement. It is adequate to compare the shock positions of the pole relative to the equator. The relative shock positions as a function of time with and without shock-front adjustments are plotted in Fig. 105.53. The fine-tuning of the shock-front uniformity aligns the shock front prior to ignition. Without the fine tuning, the misalignment is about 20 μm at 8.0 ns, whereas the tuned shock front achieves almost perfect alignment. The multiplication factors found after the complete tuning process are plotted in Fig. 105.52(b).

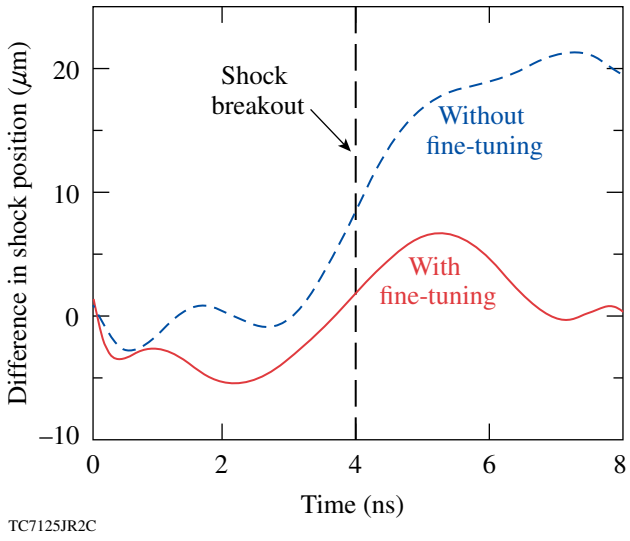

Figure 105.53
Relative shock positions (shock position along the pole minus shock position along the equator) as a function of time with and without fine-tuning of the shock front for the NIF simulations. The dashed line is without fine-tuning. The solid line is after fine-tuning the shock front. The case with fine-tuning ignites.

A *DRACO* simulation in ALE mode was run for the PDD cryogenic, DT-filled, wetted CH-foam target on a 90° wedge. The angular resolution used in the simulations was 60 zones over a 90° wedge; the low-ℓ-mode structure up to mode ℓ = 16 is adequately resolved. The simulation used the 23.5°, 50°, and 80° pointings for the polar, midlatitude, and equatorial rings. The optimal pulse shapes for the three rings are plotted in Fig. 105.52. Simulated mass density and ion-temperature

profiles near the stagnation of this tuned design, at 8.12 ns, are shown in Fig. 105.54. The 10-keV hot-spot radius is about 40 μm. This simulation produced a gain of 20 using a flux limiter of 0.06 and required 1.36 MJ of laser energy for the PDD configuration compared with the 1.0 MJ required for symmetric drive with a gain of 33. The laser energy is higher because of the required compensation for losses at the equator.

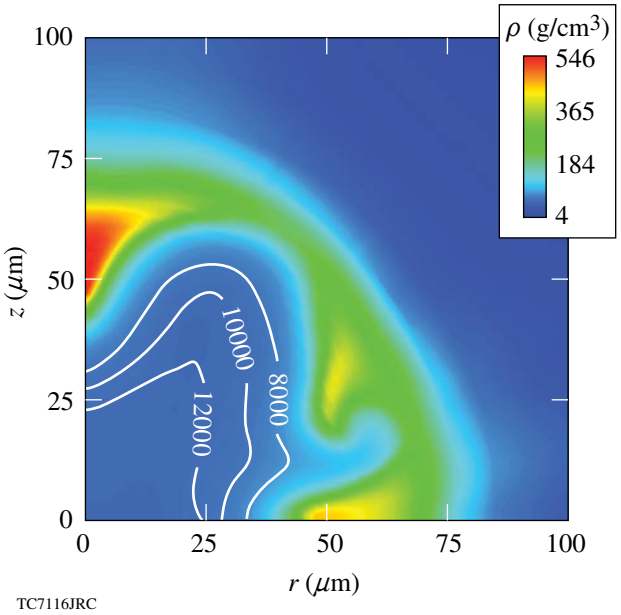

Figure 105.54
Mass density ρ and ion temperature contours in electron volts calculated by *DRACO* for a cryogenic, DT-filled, wetted CH-foam PDD target irradiated with 1.36 MJ of laser energy. The temperature contours show the formation of a ~40-μm-radius hot spot. This simulation predicts a gain of 20. The axis of symmetry is along the vertical axis; i.e., the pole is pointing upward.

Conclusions

The *DRACO* simulations of both standard-PDD and Saturn targets agreed well with the experiments during the acceleration phase by observing the characteristics of the shell evolution in the experimental and simulated x-ray radiographs. The simulations also showed the same trend as the experiments in that the Saturn targets produced higher yields than the standard-PDD targets using the existing phase plates on OMEGA (super-Gaussian of the order of 3.7). An optimized standard-PDD design was proposed that used customized phase plates, different pointings and power balance, and was able to produce a yield on par with the current Saturn design but with 5% less incident energy. Further optimization of OMEGA standard-PDD designs is expected and is currently under investigation using the techniques described here and also by employing a shimmed CH ablator on the target.

A 1.36-MJ, cryogenic DT, standard-PDD design for the NIF using the same targets as the 1.0-MJ symmetric-drive design ignited and produced a gain of 20 in a *DRACO* simulation. The PDD design employed customized phase plates, optimized beam repointings, and tuned pulse shapes for the polar, midlatitude, and equatorial rings. Maintaining a high level of shell and shock-front uniformity is found to be critical to obtaining substantial gains. Further simulations are under investigation to test the robustness of this design by including the effects of mispointing, power imbalance, and short-wavelength perturbations.

ACKNOWLEDGMENTS

This work was supported by the U.S. Department of Energy Office of Inertial Confinement Fusion under Cooperative Agreement No. DE-FC52-92SF19460, the University of Rochester, and the New York State Energy Research and Development Authority. The support of DOE does not constitute an endorsement by DOE of the views expressed in this article.

REFERENCES

1. S. Skupsky, J. A. Marozas, R. S. Craxton, R. Betti, T. J. B. Collins, J. A. Delettrez, V. N. Goncharov, P. W. McKenty, P. B. Radha, T. R. Boehly, J. P. Knauer, F. J. Marshall, D. R. Harding, J. D. Kilkenny, D. D. Meyerhofer, T. C. Sangster, and R. L. McCrory, Phys. Plasmas **11**, 2763 (2004).
2. J. Paisner *et al*., Laser Focus World **30**, 75 (1994).
3. P. W. McKenty, V. N. Goncharov, R. P. J. Town, S. Skupsky, R. Betti, and R. L. McCrory, Phys. Plasmas **8**, 2315 (2001).
4. E. M. Campbell and W. J. Hogan, Plasma Phys. Control. Fusion **41**, B39 (1999).
5. J. D. Lindl, *Inertial Confinement Fusion: The Quest for Ignition and Energy Gain Using Indirect Drive* (Springer-Verlag, New York, 1998), Chap. 6, pp. 61–82.
6. J. D. Lindl *et al*., Phys. Plasmas **11**, 339 (2004).
7. T. R. Boehly, R. S. Craxton, T. H. Hinterman, J. H. Kelly, T. J. Kessler, S. A. Kumpan, S. A. Letzring, R. L. McCrory, S. F. B. Morse, W. Seka, S. Skupsky, J. M. Soures, and C. P. Verdon, Rev. Sci. Instrum. **66**, 508 (1995).
8. J. A. Marozas, "Fourier-Transform-Based, Phase-Plate Design Technique: A High-Pass Phase-Plate Design as an Application for OMEGA and the NIF," submitted to the Journal of the Optical Society of America A.
9. R. S. Craxton and D. W. Jacobs-Perkins, Phys. Rev. Lett. **94**, 095002 (2005).
10. R. S. Craxton, F. J. Marshall, M. J. Bonino, R. Epstein, P. W. McKenty, S. Skupsky, J. A. Delettrez, I. V. Igumenshchev, D. W. Jacobs-Perkins, J. P. Knauer, J. A. Marozas, P. B. Radha, and W. Seka, Phys. Plasmas **12**, 056304 (2005).

11. P. B. Radha, V. N. Goncharov, T. J. B. Collins, J. A. Delettrez, Y. Elbaz, V. Yu. Glebov, R. L. Keck, D. E. Keller, J. P. Knauer, J. A. Marozas, F. J. Marshall, P. W. McKenty, D. D. Meyerhofer, S. P. Regan, T. C. Sangster, D. Shvarts, S. Skupsky, Y. Srebro, R. P. J. Town, and C. Stoeckl, Phys. Plasmas **12**, 032702 (2005).

12. R. A. Sacks and D. H. Darling, Nucl. Fusion **27**, 447 (1987).

13. S. Skupsky, R. Betti, T. J. B. Collins, V. N. Goncharov, D. R. Harding, R. L. McCrory, P. W. McKenty, D. D. Meyerhofer, and R. P. J. Town, in *Inertial Fusion Sciences and Applications 2001*, edited by K. Tanaka, D. D. Meyerhofer, and J. Meyer-ter-Vehn (Elsevier, Paris, 2002), pp. 240–245.

14. F. J. Marshall, R. S. Craxton, M. J. Bonino, R. Epstein, V. Yu. Glebov, D. Jacobs-Perkins, J. P. Knauer, J. A. Marozas, P. W. McKenty, S. G. Noyes, P. B. Radha, W. Seka, S. Skupsky, V. A. Smalyuk, J. A. Frenje, C. K. Li, R. D. Petrasso, and F. H. Séguin, "Polar-Direct-Drive Experiments on OMEGA," submitted to Inertial Fusion Science and Applications 2005.

15. F. J. Marshall, J. A. Delettrez, R. Epstein, V. Yu. Glebov, D. R. Harding, P. W. McKenty, D. D. Meyerhofer, P. B. Radha, W. Seka, S. Skupsky, V. A. Smalyuk, J. M. Soures, C. Stoeckl, R. P. Town, B. Yaakobi, C. K. Li, F. H. Séguin, D. G. Hicks, and R. D. Petrasso, Phys. Plasmas **7**, 2108 (2000).

16. F. J. Marshall, J. A. Delettrez, R. Epstein, R. Forties, R. L. Keck, J. H. Kelly, P. W. McKenty, S. P. Regan, and L. J. Waxer, Phys. Plasmas **11**, 251 (2004).

17. T. R. Boehly, V. A. Smalyuk, D. D. Meyerhofer, J. P. Knauer, D. K. Bradley, R. S. Craxton, M. J. Guardalben, S. Skupsky, and T. J. Kessler, J. Appl. Phys. **85**, 3444 (1999).

18. S. Skupsky, R. W. Short, T. Kessler, R. S. Craxton, S. Letzring, and J. M. Soures, J. Appl. Phys. **66**, 3456 (1989).

19. *LLE Review Quarterly Report* **78**, 62, Laboratory for Laser Energetics, University of Rochester, Rochester, NY, LLE Document No. DOE/SF/19460-295 (1999).

20. S. P. Regan, J. A. Marozas, R. S. Craxton, J. H. Kelly, W. R. Donaldson, P. A. Jaanimagi, D. Jacobs-Perkins, R. L. Keck, T. J. Kessler, D. D. Meyerhofer, T. C. Sangster, W. Seka, V. A. Smalyuk, S. Skupsky, and J. D. Zuegel, J. Opt. Soc. Am. B **22**, 998 (2005); S. P. Regan, J. A. Marozas, J. H. Kelly, T. R. Boehly, W. R. Donaldson, P. A. Jaanimagi, R. L. Keck, T. J. Kessler, D. D. Meyerhofer, W. Seka, S. Skupsky, and V. A. Smalyuk, J. Opt. Soc. Am. B **17**, 1483 (2000).

21. J. A. Marozas, J. Opt. Soc. Am. B **19**, 75 (2002).

22. R. A. Forties and F. J. Marshall, Rev. Sci. Instrum. **76**, 073505 (2005).

23. J. J. MacFarlane *et al*., in *Inertial Fusion Sciences and Applications 2003*, edited by B. A. Hammel, D. D. Meyerhofer, J. Meyer-ter-Vehn, and H. Azechi (American Nuclear Society, La Grange Park, IL, 2004), pp. 457–460; Prism Computational Sciences, Inc., Madison, WI, 53711.

24. S. Skupsky, R. S. Craxton, F. J. Marshall, R. Betti, T. J. B. Collins, R. Epstein, V. N. Goncharov, I. V. Igumenshchev, J. A. Marozas, P. W. McKenty, P. B. Radha, J. D. Kilkenny, D. D. Meyerhofer, T. C. Sangster, and R. L. McCrory, "Polar Direct Drive—Ignition at 1-MJ," submitted to Inertial Fusion Sciences and Applications 2005.

25. S. Skupsky, R. S. Craxton, F. J. Marshall, R. Betti, T. J. B. Collins, R. Epstein, V. N. Goncharov, I. V. Igumenshchev, J. A. Marozas, P. W. McKenty, P. B. Radha, J. D. Kilkenny, D. D. Meyerhofer, T. C. Sangster, and R. L. McCrory, Phys. Plasmas **11**, 276 (2004).

A Magnetorheological-Polishing-Based Approach for Studying Precision Microground Surfaces of Tungsten Carbides

Introduction

Tungsten carbide (WC) hard metals exhibit a unique combination of hardness and toughness, which makes them desirable engineering materials for wear-resistance applications such as cutting and milling tools.[1] The mixing of the hard and brittle WC particles with the more soft and ductile binder produces a composite with optimal mechanical properties.[2,3]

The metallic binder of cemented carbides is usually cobalt; however, when the application exposes the material to an acid environment, a nickel-based binder is favored for its better corrosion resistance. Another approach for improving corrosion resistance is to reduce the amount of binder,[4] namely binderless carbides. This work focuses on Ni-bonded and binderless cemented carbides. All of these materials are nonmagnetic.

The use of tungsten carbide materials in optical systems[5] as either mold masters[6] or mirrors[7] is the motivation behind achieving nanoscale surface roughness from grinding and subsequently polishing. Surface roughness is closely related to the wear mechanism of the material. SEM images of the ground surfaces exposed the similarities between the wear behavior of Ni-bonded and Co-bonded materials, in particular, the formation of a deformed surface layer because of the extrusion of the nickel binder between the WC grains, as described for Co-bonded[3,8] materials. Previous studies by others show that although the tungsten carbide wear mechanism involves brittle fracture, fatigue, and plastic deformation, it is dominated by the extrusion of the soft binder between WC grains.[1,8–10] Redeposited binder and WC debris cover the ground surface, forming a deformed layer[11] that is also known as subsurface damage, which masks the true surface roughness induced by grinding. In a recent study, the deformed layer depth was reported to be near 1.5 μm for ground WC-10 wt% Co composites (20-μm grains) with a 91-μm (approximately 34-μm nominal abrasive size) diamond wheel.[11] Because of the inhomogeneity of the composite carbide grains and the diamond distribution on the grinding wheel, however, the amount of damaged material that needed to be removed during the subsequent polishing stage could not be determined. Therefore, a more deterministic technique is needed to measure the deformed layer depth after grinding.

The goal of this work is a better understanding of the correlation between the response of tungsten carbide hard metals to microgrinding and nanopolishing with the resulting surface microroughness. In recent work done by Randi *et al.*,[12] it was demonstrated that magnetorheological finishing (MRF) can be used to determine subsurface damage depth for optical crystals and glasses. Because both Ni-bonded and the binderless cemented carbides are nonmagnetic, they are excellent candidates for MRF. In this study, we demonstrate that MRF spots can be placed on ground nonmagnetic tungsten carbides and that the spots can be used to evaluate the depth of the damaged layer. We focus on five nonmagnetic WC materials, which include four WC-Ni composites with variations in nickel binder content and one binderless sample, all with different grain sizes.

Experimental Procedures

1. Tungsten Carbide

Five commercial nonmagnetic WC samples were used for this study. The materials are commercially designated as BC12N,[13] K801,[14] M45,[15] M10,[15] and Cerbide.[16] They were selected on the basis of their nickel content and grain size as well as their mechanical properties. The WC grain sizes varied from 0.2 μm to 7 μm, and the nickel binder concentration varied from none (in the binderless carbide) to 12.5 wt%. Hardness measurements were obtained on all materials using a Tukon micro-indenter equipped with a Vickers diamond indenter and a microscope (50× objective), averaging the diagonals of five random indents on the surface with a load of 1 kg and a duration of 15 s. The applied load was enough to produce radial cracks[17] at the corners of the indentations in M10 and Cerbide. These two materials have a low ductility index (DI)[18] $(K_c/H_v)^2$, where K_c is the fracture toughness (kg/mm^2 m$^{0.5}$) and H_v is the Vickers hardness (kg/mm^2). Fracture-toughness values were calculated from the observed cracks using the Evans correlation.[19] The Laugier correlation[20] for WC material (H_v ≥ 10,000 MPa) was applied to calculate the fracture toughness

for the other three materials, which did not exhibit cracking under 1-kg loads. Relevant microstructural, mechanical, and physical properties are listed in Table 105.IV, ranked according to decreasing value of the ductility index.

2. Grinding Experiments

The grinding experiments were performed on the OptiPro SX50 platform,[21] a deterministic computer numerical control (CNC) ultraprecision grinding machine. The SX50 is capable of generating rotationally symmetric spherical and flat surfaces. For all our grinding experiments, a contour-tool grinding configuration for flat surfaces was used (Fig. 105.55) with three different diamond tools, rough, medium, and fine (40-μm, 10- to 20-μm, 2- to 4-μm grit size, respectively). Both the rough and medium tools were made of a bronze matrix while the fine tool matrix was resin. To avoid taking the part off the machine between operations, the tools were trued and dressed in advance using Al_2O_3 dressing sticks that were 320 or 800 grit (29- to 32-μm and 9- to 12-μm grit size, respectively). Table 105.V lists the grinding conditions used where Ω_t is the wheel speed, and Ω_w is the spindle speed.

Each workpiece was glued on a steel base with hot wax and then placed in the grinding machine parallel to the tool axis of rotation. Water–oil emulsion coolant (Opticut solution 5%, 9–10 pH)[22] was delivered to the interface between the workpiece and tool to avoid burn out and thermal damage. The grinding was done with two passes for each tool; i.e., the total material removed depth of cut per tool was 200, 40, and 10 μm (rough, medium, and fine tools, respectively). For example, the fine grinding was done only after the part had gone through two-pass cycles with the rough and mediums tools. Finally, the workpieces were cleaned using acetone.

3. Investigation of the Deformed Layer

a. Etching of ground surface. After the materials were ground, a small area on the processed surface was etched to remove the deformed nickel binder. The etching solution contained 15-ml deionized water, 15-ml glacial acetic acid, 60-ml hydrochloric acid/32%, and 15-ml nitric acid/65%.[11] Each surface was etched for 3 min, then rinsed with water, and finally cleaned with acetone.

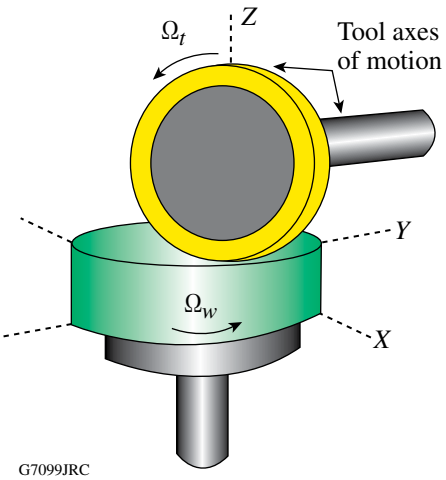

Figure 105.55
Schematics of the contour-grinding configuration adapted from Ref. 30.

Table 105.IV: Material microstructural and mechanical properties.[(a)]

Material ID	Dimensions (mm) per number of samples	Grain size (μm)	Ni wt%	Hardness Rockwell A	Young's modulus E (GPa)[(c)]	Vickers hardness H_v (GPa)[(e)]	Fracture toughness K_c (MPa $\sqrt{m}$)	Ductility index DI $\left(K_c/H_v\right)^2$ (μm)
BC12N[13]	30 × 26/2	1.0	12	87.5–89.0	(614)[(d)]	12.01±0.13	12.98[(g)]	1.17
K801[14]	40 Φ/3	7.0	6.3	90.7	618	13.71±0.17	10.15[(g)]	0.55
M45[15]	30.01 Φ/3	0.6–1.3	12.5[(b)]	89.5	500	14.78±0.17	8.06[(g)]	0.30
M10[15]	30.01 Φ/3	0.2–0.6	9.5[(b)]	92.5	510	18.54±0.2	6.35±0.10[(e),(f)]	0.12
Cerbide[16]	56 × 32/2	0.4	None	95.5	620	24.72±0.61	5.75±0.04[(e),(f)]	0.05

[(a)]Catalog values, unless specified otherwise. [(b)]Approximate values from EDS measurements. [(c)]Converted from PSI. [(d)]Estimated value. [(e)]Average of five Vickers indentations at 1 kgf. [(f)]Evans.[19] [(g)]Calculated values by using Laugier's[20,32,33] correlation $K_c = 2.15 \times 10^6 \, (E/H_v)^{0.6} \, (1 + 0.012 \, E/H_v)^{0.6} \, H_v^{-1.5}$ for WC-Co composites containing a ductile (i.e., binder) phase, where E is the Young's modulus in units of MPa and H_v is the Vickers hardness in units of MPa for $H_v \geq 10{,}000$ MPa.

Table 105.V: Contour grinding conditions used on the OptiPro SX50 in a single pass.[a]

Tool grit size (μm)	Depth of cut (μm)	In-feed (Z-axis) (mm/min)	Duration of single pass (s)	Cross feed (X-axis) (mm/min)	Duration of single pass (min)
40[b]	100	0.5	12	1.0	30–40
10–20[b]	20	0.5	2.4	1.0	30–40
2–4[c]	5	0.5	0.6	5.0	6–8

[a]The following parameters remained constant: wheel speed, Ω_t = 6800 rpm and work spindle speed, Ω_w = 100 rpm. [b]Bronze-bonded, 75 diamond concentration. [c]Resin-bonded, 75 diamond concentration.

b. Processed surface spotting. Magnetorheological finishing (MRF)[23,24] is a commercial polishing process for the manufacturing of precision optics. It was used in our experiment to measure the depth of the deformed layer from grinding and the quality of the subsurface subsequently exposed. Specifically, we used a MRF research platform called the spot-taking machine,[25] which polishes spots onto the surface of a nonrotating part by lowering the part surface into contact with a rotating magnetic fluid ribbon under CNC control. The material removal rate is determined from the amount of material removed, i.e., ratio of spot volume, divided by the spotting time. The MRF fluid used in this work consisted of an aqueous mixture of nonmagnetic nanodiamond[26] abrasives, magnetic carbonyl iron, water, and stabilizers. Machine parameters such as the magnetic field strength (~2–3 kG), wheel speed (250 rpm), pump speed (125 rpm), ribbon height (1.6 mm), and depth of the part penetrating into the ribbon (0.3 mm) were kept constant and the spotting time was varied. Spotting was done on unetched regions of rough-ground, medium-ground, and fine-ground surfaces of each material. Multiple spots with time durations of 3, 6, 12, 18, and 40 min were taken on subsets of the generated surfaces as described in **Subsurface Damage Evaluation from the Spotting Experiment** (p. 56).

4. Microscopy of Processed Surfaces

Surfaces were studied using a white-light interferometer, scanning electron microscope (SEM), contact profilometer, and atomic force microscope (AFM). Before analyzing the surfaces, the samples were ultrasonically cleaned in acetone and then rinsed with alcohol; surfaces were dried using a nitrogen gun after ultrasonication and after rinsing.

Metrology was conducted as follows:

- Average microroughness data [peak-to-valley (p–v), and root mean square (rms)] were obtained with a Zygo NewView 5000 noncontacting white-light interferometer[27] over five 350-μm by 250-μm areas randomly distributed across ground and unetched areas. This instrument has a lateral resolution of ~1 μm and a vertical resolution of ~0.3 nm. Data were similarly obtained inside MRF spots; see details in **Subsurface Damage Evaluation from the Spotting Experiment** (p. 56).

- The morphologies of the processed surfaces after grinding, etching, and MRF were analyzed using a LEO 982 FE SEM equipped with a secondary electron detector, a backscatter detector, and also an energy dispersive x-ray spectroscopy detector (EDS). The preferred imaging configuration was a mix signal of the in-lens and in-chamber secondary electron detectors. The EDS x-ray detector was used to approximate Ni content for WC samples M10 and M45.

- The Taylor Hobson TalySurf 2 PGI stylus profilometer[28] was used to perform 3-D scans of the MRF spots, which were then used to extract the spot physical dimensions, i.e., spot volume, peak removal depth, and spot profile. The stylus tip is a cone with a 60° angle and a 2-μm spherical tip radius of curvature. The instrument has a 12-nm vertical resolution.

- Additional surface scans for selected spots were taken on the Digital Instruments/Veeco Metrology Dimension 3100S-1 AFM[29] over three 10- × 10-μm^2 areas randomly distributed across areas in spots where the deepest point of fluid penetration (ddp) occurred, as discussed below. This instrument has a vertical noise resolution of less than 0.5 Å.

Experimental Results

1. Surface Roughness and Surface Morphology from Grinding

Surface-roughness data for all materials after each grinding stage were taken using the white-light interferometer. Results are reported in Table 105.VI for all surfaces in their as-ground state.

The data given in Table 105.VI show the expected result of smoothing with decreasing diamond abrasive size. The p–v surface roughness varied from ~3280 nm (BC12N) to ~5820 nm (M10) with the coarse tool, from ~550 nm (K801) to ~3850 nm (M10) with the medium tool, and from ~53 nm (M45) to ~86 nm (BC12N) with the fine tool. The smoothest surface after fine grinding was ~7-nm rms (M45).

After the samples were ground with the fine resin tool (2- to 4-μm grit size), a "mirror quality" surface finish was achieved, as shown in Fig. 105.56. Surface roughness measurements were below 100 nm p–v and below 13-nm rms for all materials, as seen in Fig. 105.57. All surfaces had some degree of midspatial frequency artifacts (i.e., cutter marks), however, with a better surface for the circular-shaped parts over the rectangular ones because of the interrupted cut during part rotation. All the grinding tools showed some degree of material accretion from the workpiece.

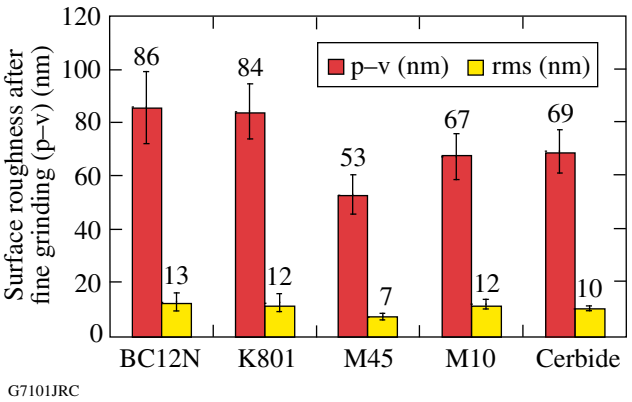

G7101JRC

Figure 105.57
Surface roughness of fine-ground surfaces (2- to 4-μm grit size) versus WC material type. The error bars represent the standard deviation of five areal measurements.

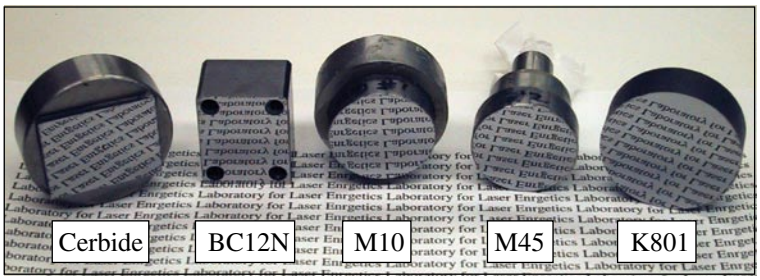

G7100JRC

Figure 105.56
Optical image of the "mirror-like" fine-ground WC material after fine grinding (2- to 4-μm grit size). Surface-roughness measurements were below 100-nm p–v and below 13-nm rms.

Table 105.VI: Tungsten carbide surface roughness under contour grinding conditions using rough, medium, and fine tools. Measurements were taken on the white-light interferometer.

	BC12N	K801	M45	M10	Cerbide
	Rough tool (40-μm grit size)				
p–v (nm)	3280±194	3802±289	3915±371	5823±975	3857±326
rms (nm)	154±19	151±30	286±113	695±289	242±67
	Medium tool (10- to 20-μm grit size)				
p–v (nm)	2372±59	552±136	1915±175	3854±265	3322±153
rms (nm)	72±4	27±4	65±11	195±14	142±9
	Fine tool (2- to 4-μm grit size)				
p–v (nm)	86±13	84±10	53±7	67±9	69±8
rms (nm)	13±3	12±3	7±1	12±2	10±1

SEM images illustrated that the topography of the ground surfaces, from rough to fine, were in agreement with the surface-roughness measurements. Figure 105.58 gives the typical morphology of rough-ground surfaces (rough tool, 40-μm grit size). Fragmented WC particles and plastically deformed material (arrows 1 and 2) are observed on the ground surfaces, forming a deformed surface layer, as described by Hegeman *et al.*[11] Material K801, with an average grain size of 7 μm (the coarsest of all materials studied, see Table 105.IV), showed some pullout of individual grains. Figure 105.58(a) shows that the deformed layer is absent in regions of grain pullout[11] (arrow 3). We observed different morphologies of the deformed layer for the different materials. The deformed layer appears smoother for materials with a submicron grain size (0.2 to 0.6 μm) [Fig. 105.58(c) and 105.58(d)]. The plastic deformation of the binderless material is similar to that for the Ni-bonded materials, i.e., fragmented and plastically deformed WC grains (arrows 1 and 2, respectively), suggesting that only small amounts of the binder are present in the deformed surfaces, compared to the bulk material, as observed by Yin *et al.*[5] and Hegeman *et al.*[11] Therefore, the deformed surfaces mostly consist of plastically deformed WC grains.

Figure 105.59 shows SEM images of the fine-ground surfaces that reveal the material microstructure, i.e., the carbide grains and the nickel binder. Fragmented traces of the WC grains are visible inside "pockets" between grains (arrow 1). Traces from single diamond scratches and tool marks[30] can be seen at arrow 2.

All ground surfaces were etched in small regions to remove the nickel binder, exposing the subsurface of the deformed layer. In some areas on the surface the plastically deformed material, as well as WC debris, was removed, leaving small etching pits. The etching procedure also removed bronze and resin tool residue from the surface. Figure 105.60 shows a SEM image of a typical etching pit in a fine-ground surface, which exposed the subsurface of the ground surface. It can be clearly observed that almost all the nickel binder between grains was removed along with fragmented WC particles that were embedded. High-magnification images of the etched pits [Fig. 105.61(a)] showed subsurface damage in the form of cracked grains after rough grinding (40 μm). Figures 105.61(b) and 105.61(c), for both medium and fine tools (10- to 20-μm, and 2- to 4-μm grit size, respectively), reveal no evidence of

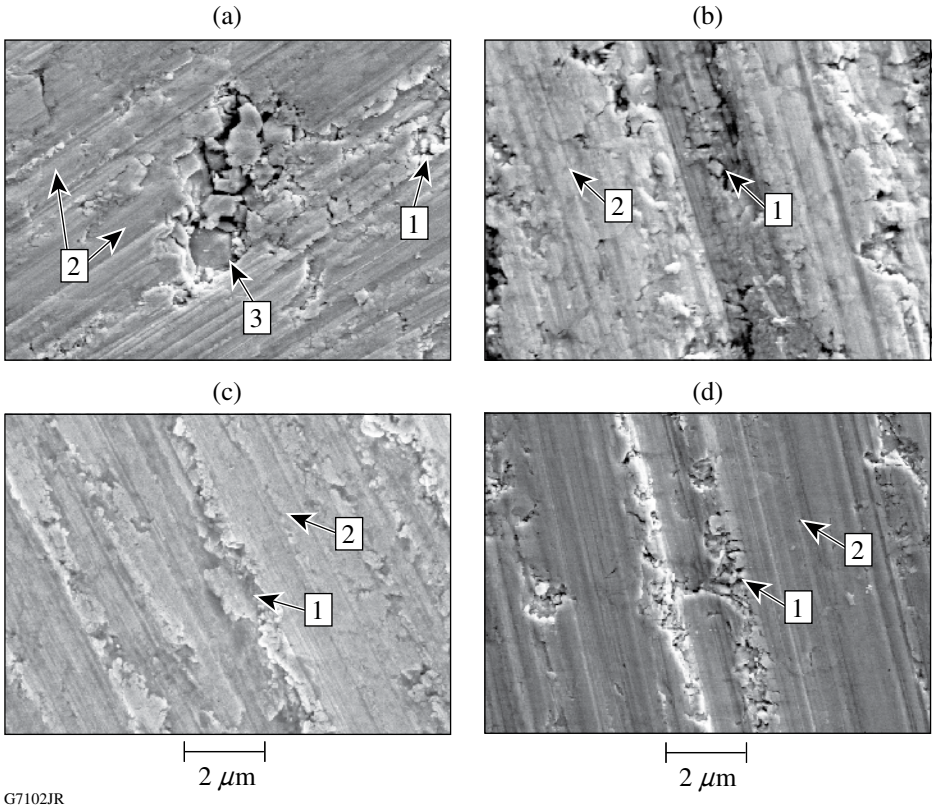

Figure 105.58
SEM images of typical rough-ground surfaces (40-μm grit size). Average grain sizes are (see Table 105.IV) (a) K801, 6.3 wt% Ni, 7 μm; (b) M45, 12.5 wt% Ni, 0.6–1.3 μm; (c) M10, 9.5 wt% Ni, 0.2–0.6 μm; and (d) Cerbide, 0.4 μm. Arrows represent (1) fragmented WC, (2) plastically deformed WC, and (3) the pullout of an individual grain.

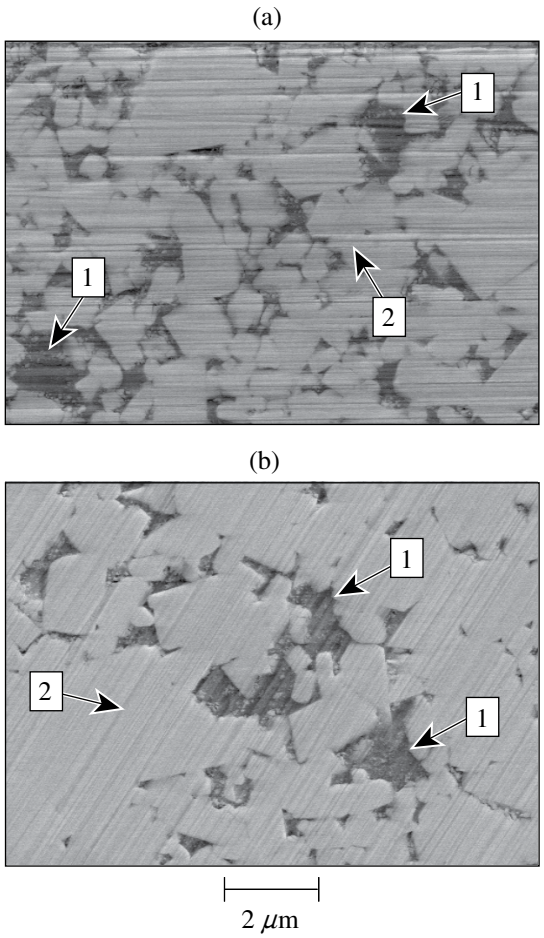

Figure 105.59
SEM images of fine-ground WC surfaces (2- to 4-μm grit size). (a) BC12N, 12 wt% Ni, 1-μm grain size and (b) K801, 6 wt% Ni, 7-μm grain size (see Table 105.IV). Arrows represent (1) "pockets" between grains and (2) single diamond scratches/tool marks.

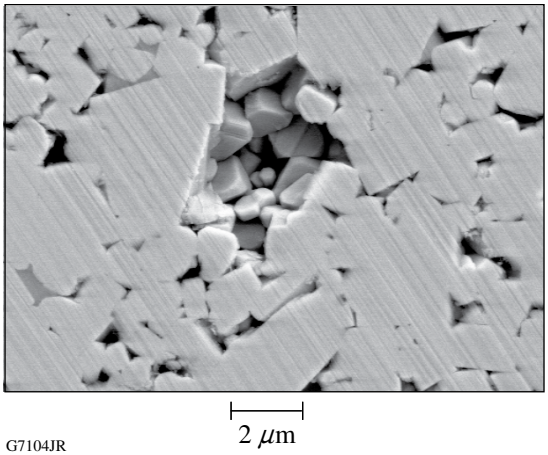

Figure 105.60
SEM images of a typical etched pit in a fine-ground (2- to 4-μm grit size) WC surface, K801, 6 wt% Ni, 7-μm grain size (see Table 105.IV).

fractured WC grains, suggesting that the wear mechanism is controlled by plastic flow. The Cerbide ground surface was not affected by the etching, as expected.

2. Subsurface Damage Evaluation from the Spotting Experiment

MRF spots of various durations were taken on all rough-ground surfaces and 6-min spots were taken on both fine- and medium-ground surfaces. Figure 105.62 shows a typical 3-D map of a polished MRF spot indicating the spot leading edge (MRF fluid ribbon entrance/penetration point into the material), spot ddp (deepest point of MRF fluid penetration), and spot trailing edge (point of the fluid leaving the part) using the profilometer. From analyzing the 3-D scans, we were able to extract spot profiles, which were then used to identify the

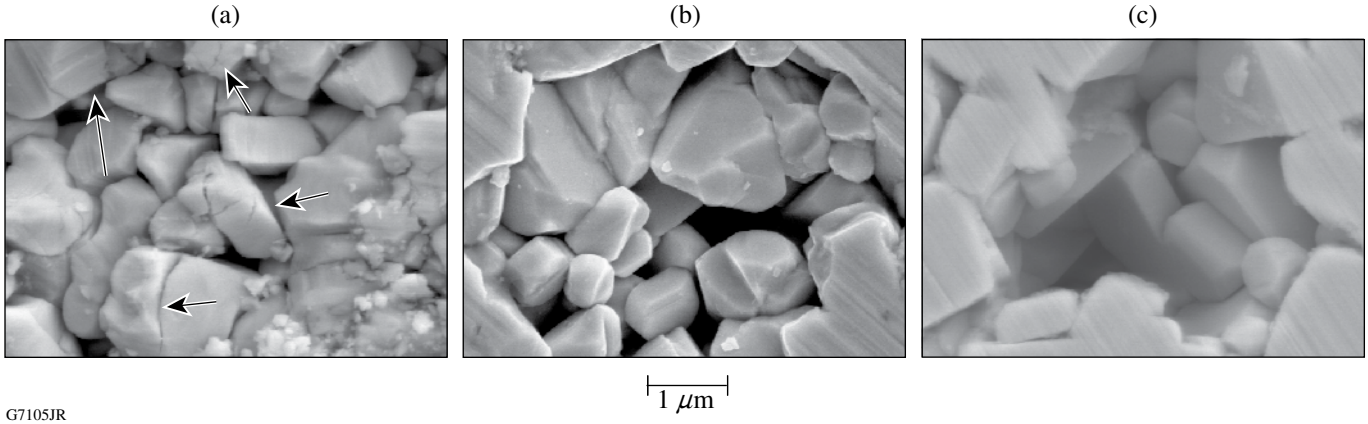

Figure 105.61
High-magnification SEM images of etching pits in ground WC composites showing the (a) rough, (b) medium, and (c) fine ground. The arrows in (a) point at cracks in the carbide phase. The materials are (see Table 105.IV) (a) BC12N, 12 wt% Ni, 1-μm grain size and (b) and (c) K801, 6 wt% Ni, 7-μm grain size.

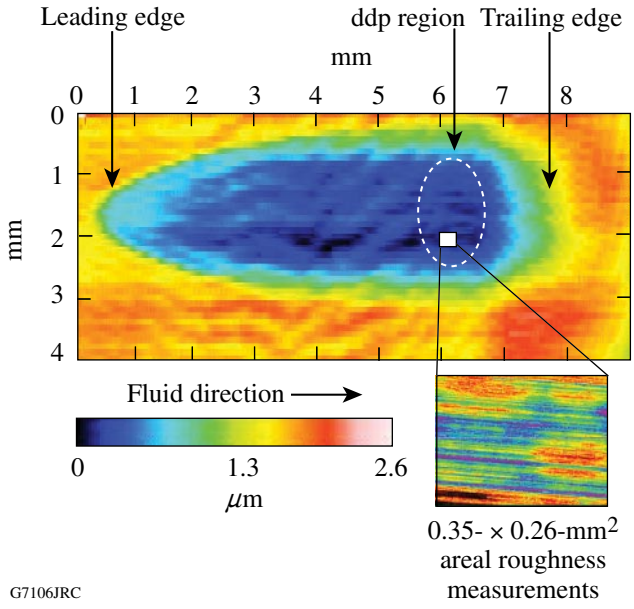

Figure 105.62
3-D image of an MRF spot taken with a Taylor Hobson TalySurf profilometer on WC M10 for 6 min. Arrows indicate the spot leading edge (MRF fluid ribbon entrance/penetration point into the material), spot ddp (deepest point of MRF fluid penetration), spot trailing edge (were the MRF fluid leaves the material), and fluid flow direction. The white rectangle within the ddp region represents one of the five sites over which surface roughness was measured using white-light interferometry.

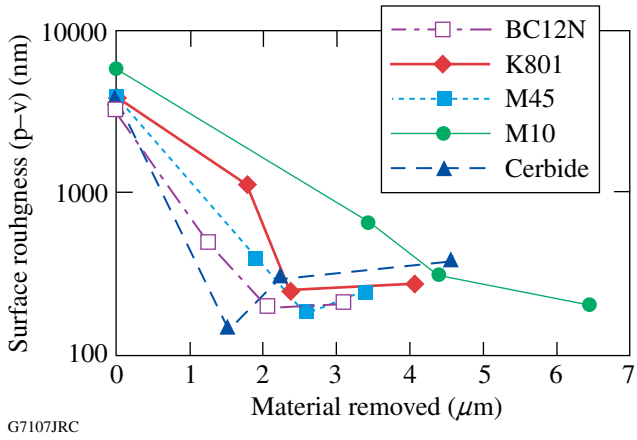

Figure 105.63
Evaluation of surface roughness, p–v (nm) semilog, versus MRF spot material removed (μm). The starting condition is the rough-ground surface (p–v roughness in the range of 3.3 to 5.8 μm). After removing 2 to 3 μm of material from the surface, the p–v roughness decreases to 180–310 nm.

ddp. The spot volume and maximum depth ddp are listed in Table 105.VII. These spot profiles were not similar to profiles typically observed for other optical glasses and crystals.[25]

After the location of the spot ddp was identified, surface-roughness measurements at five random locations within the ddp region were taken with the white-light interferometer. Results are given in Table 105.VII. To investigate the amount of material needed to be removed by the MRF spot (i.e., the depth of the deformed layer from the grinding cycles), we plotted the evolution of the surface roughness with the maximum amount of material removed (see Fig. 105.63). It was observed that the initial surface roughness is removed for BC12N, K801, M45, and Cerbide when the MRF penetrates past 2.1 to 2.6 μm of the deformed layer thickness. However, surface roughness eventually increased with increasing MRF material removal. A monotonic decrease in surface roughness with increasing material removal was noted for M10. SEM images taken within the ddp region of the optimal spot (i.e., least roughness) confirmed that the deformed layer induced by grinding is completely removed by the MRF process (see Fig. 105.64). It should be emphasized that the clean surfaces shown in Fig. 105.64 are due entirely to the MRF process, without any pre- or post-etching.

Table 105.VII also demonstrates the influence of the initial surface roughness on the surface response inside MRF spots. For initial rough-ground surfaces, surface roughness improved after MRF penetrated 2.1 to 2.6 μm past the deformed layer for BC12N, K801, M45, and Cerbide and 4.4 μm for M10. The p–v surface roughness varied from ~185 nm (M45) to ~303 nm (Cerbide). For initial fine-ground surfaces, the p–v surface roughness varied from ~29 nm (Cerbide) to ~86 nm (BC12N). The smoothest surface for the initial fine-grinding surface conditions was ~3.4-nm rms (Cerbide). We also observed an increase in surface roughness inside MRF spots for materials with a higher ductility index, however, after 1 to 1.8 μm was removed (by the MRF spot).

3. MRF Surface Evolution with Increasing Depth Removed

Further study of the surface after MRF polishing was done for rough-ground K801 with an ~3802-nm initial p–v surface roughness [see Fig. 105.65(a)] where additional MRF spots at varying depths of MRF removal were taken. Figure 105.65 shows that after 1.8 μm of material is removed by the MRF spot, the deformed layer induced is not completely removed [see Fig. 105.65(b)], in agreement with the surface-roughness values. With a longer MRF spotting time, a total of 2.4-μm of material was removed [see Fig. 105.65(c)], an amount sufficient to expose the undisturbed subsurface. However, additional material removal slightly increases the surface roughness. Similar behavior is observed by monitoring the evolution of the rms surface roughness.

Table 105.VII: Summary results of the spotting experiments. Surface-roughness measurements were taken at five random locations within a spot ddp with the white-light interferometer. The maximum spot depth and volume removed were extracted from the profilometer 3-D scans.

Spot time (min)		BC12N	K801	M45	M10	Cerbide
		Initial surface conditions: rough ground				
3	p–v (nm)	505±37	1106±143	399±52	657±216	146±17
	rms (nm)	43±5	46±5	47±5	83±16	25±5
	Depth (μm)	1.3±0.08	1.8±0.01	1.9±0.08	3.4±0.28	1.5±0.03
	Vol. (mm^3)	0.01±0.0	0.01±0.0	0.01±0.0	0.02±0.01	0.01±0.0
6	p–v (nm)	204±10	248±24	185±26	312±20	303±20
	rms (nm)	35±2	39±5	31±11	61±6	55±11
	Depth (μm)	2.1±0.01	2.4±0.03	2.6±0.05	4.4±0.21	2.3±0.12
	Vol. (mm^3)	0.02±0.0	0.02±0.0	0.02±0.0	0.03±0.01	0.03±0.0
12	p–v (nm)	—	287±31	—	—	—
	rms (nm)	—	43±10	—	—	—
	Depth (μm)	—	3.2±0.07	—	—	—
	Vol. (mm^3)	—	0.03±0.0	—	—	—
18	p–v (nm)	212±51	276±60	240±32	205±50	383±56
	rms (nm)	33±5	45±12	40±11	39±10	63±14
	Depth (μm)	3.1±0.08	4.0±0.09	3.4±0.31	6.4±0.06	4.6±0.13
	Vol. (mm^3)	0.02±0.0	0.04±0.0	0.03±0.0	0.06±0.01	0.04±0.0
40	p–v (nm)	—	395±134	—	—	—
	rms (nm)	—	53±9	—	—	—
	Depth (μm)	—	8±0.13	—	—	—
	Vol. (mm^3)	—	0.08±0.0	—	—	—
		Initial surface conditions: medium ground				
6	p–v (nm)	215±5	456±33	107±13	113±21	114±20
	rms (nm)	35±2	27±5	16±1	19±2	20±3
	Depth (μm)	1.8±0.05	1.5±0.03	1±0.04	1.9±0.10	1.5±0.06
	Vol. (mm^3)	0.02±0.0	0.02±0.0	0.01±0.0	0.02 ±0.0	0.02±0.0
		Initial surface conditions: fine ground				
6	p–v (nm)	202±39	185±23	151±26	80±15	29±2
	rms (nm)	27±5	26±4	22±6	9±3	3±0.3
	Depth (μm)	1.9±0.03	2.2±0.05	1.6±0.03	1.7 ±0.02	1±0.06
	Vol. (mm^3)	0.02±0.0	0.02±0.0	0.01±0.0	0.02 ±0.0	0.01±0.0

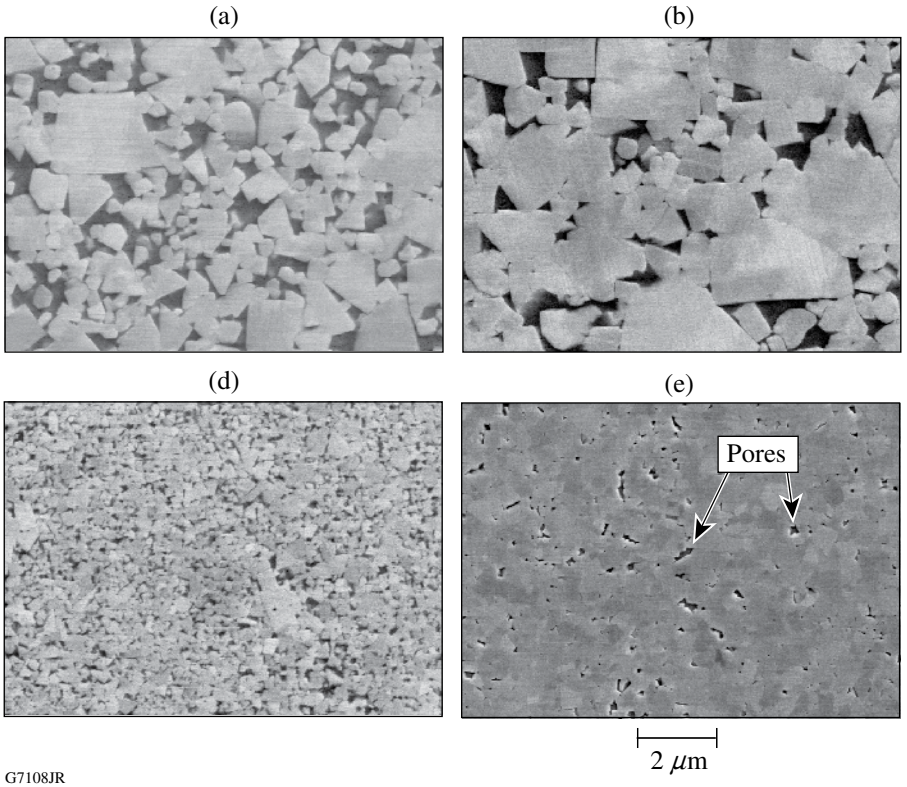

Figure 105.64
SEM images of WC-Ni composites polished for 6 min with MRF fluid containing nanodiamond abrasives. The average grain sizes are (see Table 105.IV) (a) BC12N, 12 wt% Ni, 1 μm; (b) K801, 6.3 wt% Ni, 7 μm; (c) M45, 12.5 wt% Ni, 0.6–1.3 μm; (d) M10, 9.5 wt% Ni, 0.3–0.6 μm; and (e) Cerbide, 0.4 μm.

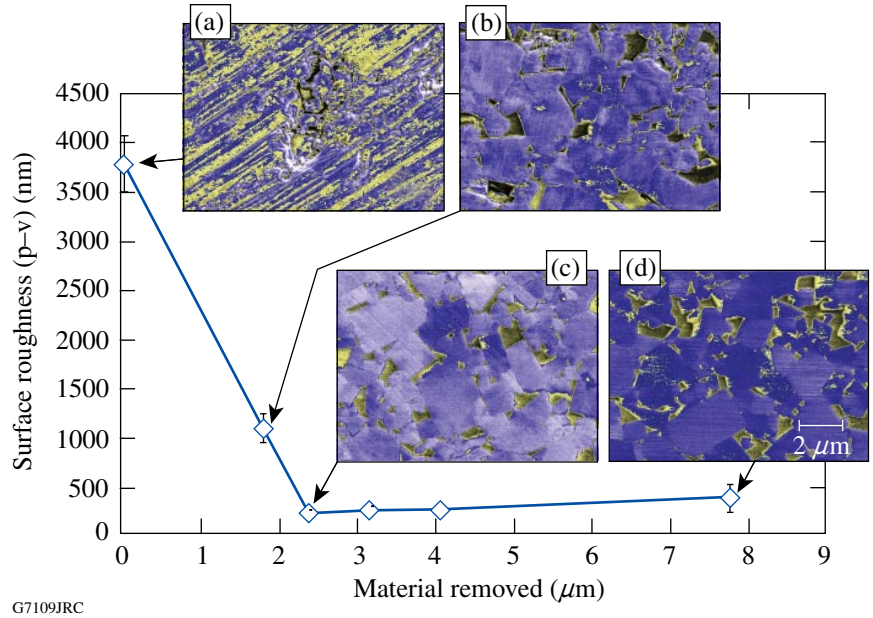

Figure 105.65
Surface roughness in the MRF spots, p–v (nm), versus MRF spot material removal in microns for rough-ground K801. Each data point represents a spot time of as rough ground, 3, 6, 12, 18, and 40 min. The SEM images correspond to the (a) initial ground surface and (b) 1.8-, (c) 2.4-, and (d) 8-μm material removed (within the spot ddp region). The error bars represent the standard deviation of five areal measurements.

Discussion

The results from the grinding experiments indicate no correlation between grinding-induced surface roughness and the materials' microstructure, i.e., Ni wt% or grain size, for all grinding conditions, as also observed by Yin *et al.*[5] In addition, surface roughness did not correlate well to the materials' hardness. As observed in the case of optical glasses under deterministic microgrinding conditions,[18] surface roughness correlates with the ductility index $(K_c/H_v)^2$ (units of length) for both grinding and MRF processes conditions. Figure 105.66 shows that surface roughness values increased with increasing ductility index value. The true surface roughness is not well characterized as a result of heavily deformed material, fragmented WC, and tool residue over the ground surface.

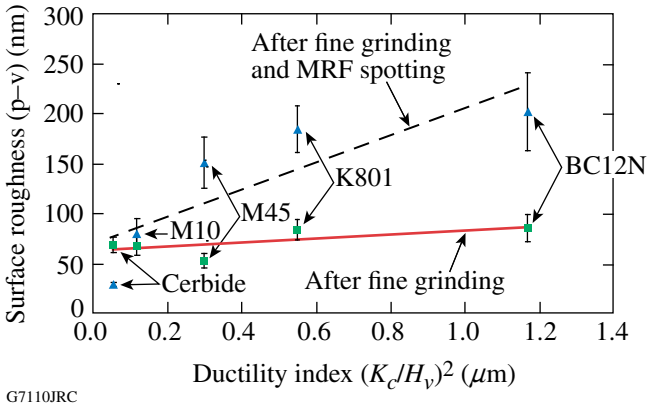

Figure 105.66
Surface-roughness measurements versus the materials' ductility index $(K_c/H_v)^2$. Data are for surfaces that were fine ground (correlation with ductility index has $R^2 = 0.47$) or fine ground and subsequently MRF spotted (correlation with ductility index has $R^2 = 0.70$).

Etching of the ground surface exposed some of the subsurface damage below the ground surface. SEM high-magnification images in the etching pits exposed cracks in WC grains of rough-ground surfaces, whereas for the medium- and fine-ground surfaces, removal was found to be within the ductile/plastic regime (see Fig. 105.61).

MRF spots are useful for analyzing both the material microstructure as well as for measuring the depth of the deformed surface layer from grinding. By removing an optimal amount of material (proportional to the initial p–v roughness in the rough-ground surfaces), the surface roughness is significantly reduced. However, additional material removal (beyond the optimal amount) resulted in a slight increase in surface roughness for materials with a high ductility index value. These results suggest that to completely remove the deformed surface layer after rough grinding (~40-μm grit size), an amount of material equivalent in depth to the initial p–v surface roughness that needs to be polished/removed. For the materials tested, removing the initial p–v surface roughness values was sufficient to completely eliminate the damaged/deformed surface layer with the exception of WC M10, which showed a monotonic decrease of roughness with the amount of material removed. The increase in surface roughness for the Cerbide can be explained in Fig. 105.64(e), which clearly shows some degree of porosity at the carbide boundaries.

The effect of the initial surface roughness from grinding with rough, medium, or fine tools on the MRF performance is shown in Tables 105.VI and 105.VII. Initial ground surface conditions, either coarse or fine, had a small effect on the resulting surface roughness inside the MRF spot for materials with a high ductility index. The p–v and rms surface roughness improved with a decreasing ductility index for initial fine-grind conditions. However, we found that MRF spot surface roughness was higher than the initial fine-ground surface, e.g., from ~86 nm (BC12N) after fine grinding to ~202 nm (BC12N) following MRF removal in the range of 1 to 2.2 μm.

Further investigation of surface response inside a MRF spot for materials with a high ductility index was done to investigate the eventual slight increase of roughness with the amount of material removed. Figure 105.65 suggests that additional spot time promotes preferential polishing of the nickel binder, which resulted in increasing surface-roughness values. The effect of preferential polishing on surface roughness is also known as grain decoration.[31] A selective AFM scan demonstrates preferential polishing/grain decoration on the resulting surface roughness inside the MRF spot. Figure 105.67(a) shows AFM scans from the ddp in K801 (7-μm average grain size) after an optimal 2.4-μm amounts of material have been recovered (pit depth in the range of 9 to 12 nm), while Fig. 105.67(b) shows the development of preferential grain decoration when an excessive amount (8 μm) has been removed (pit depth in the range of 27 to 61 nm). These features show that MRF spot-derived material removal can be optimized to remove the damaged layer at the surface without acceleration grain decoration. Excessive amounts of MRF removal may lead to grain decoration in a material with a higher ductility index. On the other hand, materials with a lower ductility index like M10 may show a monotonic reduction to surface roughness with the amount of material removed by MRF. This represents true polishing of this material, a desired outcome for the manufacture of mold masters or other optics from WC.

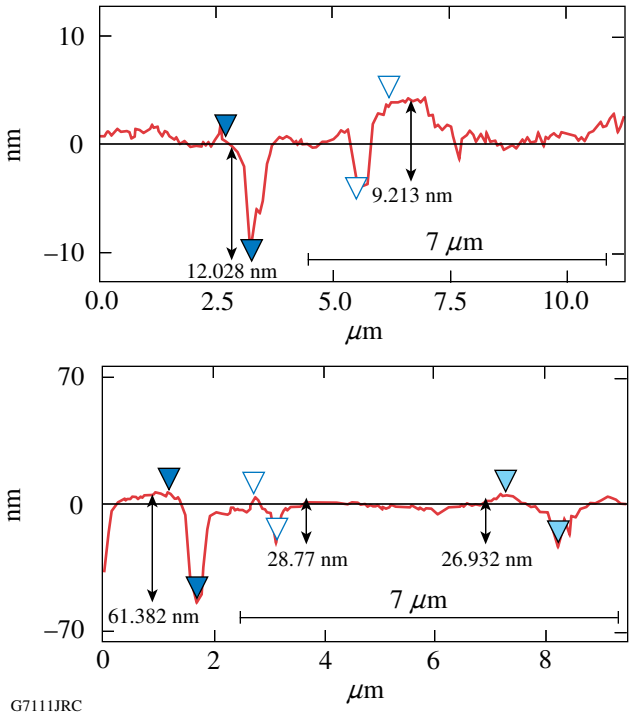

Figure 105.67
AFM surface profiles from the ddp region of a MRF spot taken on K801 (average grain size 7 μm). (a) 2.4 μm and (b) 8 μm were removed. The initial surfaces were rough ground and had a p–v surface roughness of 3.8 μm. The double arrows represent the vertical distance between markers and the scale bar represents the average grain size.

Conclusions

We have studied the response of five nonmagnetic WC composites to deterministic microgrinding. Grinding experiments showed that grinding-induced surface roughness decreased with decreasing diamond abrasive size. Microgrinding with a rough tool (40-μm grit size) involved fracture, leading to a p–v surface roughness in the range of 3.2 to 5.8 μm (150- to 700-nm rms). Microgrinding with medium and fine tools (10- to 20-μm and 2- to 4-μm grit size, respectively) was controlled by plastic flow. The medium tool led to p–v surface roughness values in the range of 0.5 to 3.8 μm (27- to 200-nm rms), whereas the fine tool resulted in surface p–v values in the range of 53 to 86 nm (7- to 13-nm rms). The true grinding-induced surface roughness was concealed by the deformed layer on the ground surface.

We have demonstrated that a MRF spot can be placed on ground surfaces of tungsten carbide and that the spot can be used to evaluate the depth of the surface deformed layer. For the rough and medium tools, the deformed layer is in the range 1.5- to 2.7-μm. The surface roughness of MRF spot at the deepest point of penetration can be used as a guide for establishing the optimal amount of material to be removed by MRF. Optimal MRF removal indeed removes the deformed surface layer caused by grinding. Excessive MRF removal may lead to preferential polishing and removal of the binder phase, also known as grain decoration. By utilizing both surface-roughness measurements and SEM imaging at the spot ddp, we were able to estimate the depth of the deformed layer. Thus, we showed that the depth of the deformed layer can be estimated in two ways. An optical profilometer-based measurement of the p–v surface microroughness of the ground surface provides an upper bound to the deformed layer thickness. This is a desirable estimate given the noncontact nature of this metrology technique. On the other hand, the MRF spot can also be used to reveal the depth of the deformed layer while reducing the surface roughness.

ACKNOWLEDGMENT

The authors thank A. Shorey of QED Technologies in Rochester, NY, for the use of the AFM and K. Muir of the Laboratory for Laser Energetics Summer High School Research Program for surface-roughness measurements. The authors acknowledge the Laboratory for Laser Energetics at the University of Rochester for its continuing support. One of the authors (S. Shafrir) is a LLE Horton Fellow. This work was supported by the U.S. Department of Energy Office Confinement Fusion under Cooperative Agreement No. DE-FC52-92SF19460, the University of Rochester, and the New York State Energy Research and Development Authority. The support of DOE does not constitute an endorsement by DOE of the views expressed here.

REFERENCES

1. G. S. Upadhyaya, *Cemented Tungsten Carbides: Production, Properties, and Testing*, Materials Science and Process Technology Series (Noyes Publications, Westwood, NJ, 1998).

2. G. Wirmark and G. Dunlop, in *Science of Hard Materials*, edited by R. K. Viswanadham, D. J. Rowcliffe, and J. Gurland (Plenum Press, New York, 1983), pp. 311–338.

3. J. Larsen-Basse, J. Mater. **35**, 35 (1983).

4. S. Imasato *et al.*, Int. J. Refract. Met. Hard Mater. **13**, 305 (1995).

5. L. Yin *et al.*, Int. J. Mach. Tools Manuf. **44**, 533 (2004).

6. W. K. Chen *et al.*, Precis. Eng. **29**, 315 (2005).

7. L. Yin *et al.*, Proc. Inst. Mech. Eng. B, J. Eng. Manuf. **218**, 419 (2004).

8. J. Larsen-Basse and N. Devnani, in *Science of Hard Materials*, edited by E. A. Almond, C. A. Brookes, and R. Warren, Institute of Physics Conference Series, No. 75 (Hilger, Bristol, England, 1986), pp. 883–895.

9. J. Larsen-Basse, in *Science of Hard Materials*, edited by R. K. Viswanadham, D. J. Rowcliffe, and J. Gurland (Plenum Press, New York, 1983), pp. 797–813.

10. W. Precht, R. K. Viswanadham, and J. D. Venables, in *Science of Hard Materials*, edited by R. K. Viswanadham, D. J. Rowcliffe, and J. Gurland (Plenum Press, New York, 1983), pp. 815–828.

11. J. B. J. W. Hegeman, J. Th. M. De Hosson, and G. de With, Wear **248**, 187 (2001).

12. J. A. Randi, J. C. Lambropoulos, and S. D. Jacobs, Appl. Opt. **44**, 2241 (2005).

13. Basic Carbide, Lowber, PA 15660.

14. Kennametal, Inc., Charlotte, NC 28273.

15. Fuji Die Co., Ltd., Ota-ku, Tokyo, Japan.

16. Materials tested were commercially available in January 2005, Cerbide, Inc., Orchard Park, NY 14127.

17. J. Larsen-Basse, in *Tribology—Friction, Lubrication and Wear, Fifty Years On: Proceedings of the Institution of Mechanical Engineers, International Conference* (Mechanical Engineering Publications Ltd., Bury St. Edmunds, Suffolk, 1987), pp. 277–282.

18. J. C. Lambropoulos, T. Fang, P. D. Funkenbusch, S. D. Jacobs, M. J. Cumbo, and D. Golini, Appl. Opt. **35**, 4448 (1996).

19. A. G. Evans, in *Fracture Mechanics Applied to Brittle Materials*, edited by S. W. Freiman (American Society for Testing and Materials, Philadelphia, 1979), Vol. ASTM STP 678, Part 2, pp. 112–135.

20. M. T. Laugier, J. Mater. Sci. Lett. **6**, 768 (1987).

21. OptiPro Systems, Ontario, NY 14519.

22. Opticut GPM 5% in water, pH 9-10, Lighthouse Lubricant Solutions, LLC, Overland Park, KS 66282.

23. S. D. Jacobs, H. M. Pollicove, W. I. Kordonski, and D. Golini, in *International Conference on Precision Engineering*, ICPE '97 (ICPE, Taipei, Taiwan, 1997), pp. 685–690.

24. A. B. Shorey, S. D. Jacobs, W. I. Kordonski, and R. F. Gans, Appl. Opt. **40**, 20 (2001).

25. S. R. Arrasmith, I. A. Kozhinova, L. L. Gregg, A. B. Shorey, H. J. Romanofsky, S. D. Jacobs, D. Golini, W. I. Kordonski, S. J. Hogan, and P. Dumas, in *Optical Manufacturing and Testing III*, edited by H. P. Stahl (SPIE, Bellingham, WA, 1999), Vol. 3782, pp. 92–100.

26. S. D. Jacobs, Finer Points **7**, 47 (1995).

27. Zygo NewView™ 5000 White Light Interferometer, Zygo Corporation, Middlefield, CT 06455.

28. Taylor Hobson TalySurf 2 PGI profilometer, 120-mm traverse unit, 10-mm gauge range, 12-nm vertical resolution, and 0.1-μm accuracy. Stylus specifications: 60° tip angle and 2-μm tip radius, Taylor Hobson, Inc., Rolling Meadows, IL 60008-4231.

29. Digital Instruments/Veeco Metrology Dimension 3100S-1 Atomic Force Microscope, Veeco Instruments, Inc., Woodbury, NY 11797-2902.

30. S. Tong, "Chatter in Contour Deterministic Microgrinding," Ph.D. thesis, University of Rochester, 2004.

31. L. L. Gregg, A. E. Marino, J. C. Hayes, and S. D. Jacobs, in *Optical Manufacturing and Testing V*, edited by H. P. Stahl (SPIE, Bellingham, WA, 2004), Vol. 5180, pp. 47–54.

32. M. T. Laugier, J. Mater. Sci. Lett. **6**, 779 (1987).

33. M. T. Laugier, J. Mater. Sci. Lett. **6**, 897 (1987).

Publications and Conference Presentations

Publications

R. Betti and C. Zhou, "High-Density and High-ρR Fuel Assembly for Fast-Ignition Inertial Confinement Fusion," Phys. Plasmas **12**, 110702 (2005).

K. M. Chandler, S. A. Pikuz, T. A. Shelkovenko, M. D. Mitchell, D. A. Hammer, and J. P. Knauer, "Cross Calibration of New X-Ray Films Against Direct Exposure Film from 1 to 8 keV Using the X-Pinch X-Ray Source," Rev. Sci. Instrum **76**, 113111 (2005).

A. C.-A. Chen, J. U. Wallace, L. Zeng, S. K.-H. Wei, and S. H. Chen, "Novel Light-Emitting Organic Materials with Variable Electron and Hole Conductivities," in *Liquid Crystals IX*, edited by I.-C. Khoo (SPIE, Bellingham, WA, 2005), Vol. 5936-18.

J. E. DeGroote, A. E. Marino, J. P. Wilson, K. E. Spencer, and S. D. Jacobs, "Effects of Nanodiamond Abrasive Friability in Experimental MR Fluids with Phosphate Laser Glass LHG-8 and Other Optical Glasses," in *Optical Manufacturing and Testing VI*, edited by H. P. Stahl (SPIE, Bellingham, WA, 2005), Vol. 5869, pp. 121–132.

J. A. Delettrez, J. Myatt, P. B. Radha, C. Stoeckl, S. Skupsky, and D. D. Meyerhofer, "Hydrodynamic Simulations of Integrated Experiments Planned for the OMEGA/OMEGA EP Laser Systems," Plasma Phys. Control. Fusion **47**, B791 (2005).

E. Fess, J. Schoen, M. Bechtold, D. Mohring, and C. Bouvier, "Ultraform Finishing Process for Optical Materials," in *Optical Manufacturing and Testing VI*, edited by H. P. Stahl (SPIE, Bellingham, WA, 2005), Vol. 5869, pp. 88–93.

J. M. Foster, B. H. Wilde, P. A. Rosen, R. J. R. Williams, B. E. Blue, R. F. Coker, R. P. Drake, A. Frank, P. A. Keiter, A. M. Khokhlov, J. P. Knauer, and T. S. Perry, "High-Energy-Density Laboratory Astrophysics Studies of Jets and Bow Shocks," Astrophys. J. **634**, L77 (2005).

D. R. Harding, T. C. Sangster, D. D. Meyerhofer, P. W. McKenty, L. D. Lund, L. Elasky, M. D. Wittman, W. Seka, S. J. Loucks, R. Janezic, T. H. Hinterman, D. H. Edgell, D. Jacobs-Perkins, and R. Q. Gram, "Producing Cryogenic Deuterium Targets for Experiments on OMEGA," Fusion Sci. Technol. **48**, 1299 (2005).

M. Haurylau, S. P. Anderson, K. L. Marshall, and P. M. Fauchet, "Electrical Tuning of Silicon-Based 2-D Photonic Bandgap Structures," in *Tuning the Optical Response of Photonic Bandgap Structures II*, edited by P. M. Fauchet and P. V. Braun (SPIE, Bellingham, WA, 2005), Vol. 5926, pp. 15–24.

A. Jukna, I. Barboy, G. Jung, S. S. Banerjee, Y. Myasoedov, V. Plausinaitiene, A. Abrutis, X. Li, D. Wang, and R. Sobolewski, "Laser Processed Channels of Easy Vortex Motion in $YBa_2Cu_3O_{7-\delta}$ Films," Appl. Phys. Lett. **87**, 192504 (2005).

J. Keck, J. B. Oliver, T. J. Kessler, H. Huang, J. Barone, J. Hettrick, A. L. Rigatti, T. Hoover, K. L. Marshall, A. W. Schmid, A. Kozlov, and T. Z. Kosc, "Manufacture and Development of Multilayer Diffraction Gratings," in *Laser-Induced Damage in Optical Materials: 2005*, edited by G. J. Exarhos, A. H. Guenther, K. L. Lewis, D. Ristau, M. J. Soileau, and C. J. Stolz (SPIE, Bellingham, WA, 2005), Vol. 5991, pp. 443–448.

K. L. Marshall, K. Adelsberger, B. Kolodzie, G. Mhyre, and D. W. Griffin, "A Second-Generation, Liquid Crystal Phase-Shifting Point-Diffraction Interferometer Employing Structured Substrates," in *Optical Diagnostics*, edited by L. M. Hanssen and P. V. Farrell (SPIE, Bellingham, WA, 2005), Vol. 5880, pp. 103–114.

R. L. McCrory, S. P. Regan, S. J. Loucks, D. D. Meyerhofer, S. Skupsky, R. Betti, T. R. Boehly, R. S. Craxton, T. J. B. Collins, J. A. Delettrez, D. Edgell, R. Epstein, K. A. Fletcher, C. Freeman, J. A. Frenje, V. Yu. Glebov, V. N. Goncharov, D. R.

Harding, I. V. Igumenshchev, R. L. Keck, J. D. Kilkenny, J. P. Knauer, C. K. Li, J. Marciante, J. A. Marozas, F. J. Marshall, A. V. Maximov, P. W. McKenty, J. Myatt, S. Padalino, R. D. Petrasso, P. B. Radha, T. C. Sangster, F. H. Séguin, W. Seka, V. A. Smalyuk, J. M. Soures, C. Stoeckl, B. Yaakobi, and J. D. Zuegel, "Direct-Drive Inertial Confinement Fusion Research at the Laboratory for Laser Energetics: Charting the Path to Thermonuclear Ignition," Nucl. Fusion **45**, S283 (2005).

A. G. Noto and K. L. Marshall, "Application of Computational Chemistry Methods to the Prediction of Chirality and Helical Twisting Power in Liquid Crystal Systems," in *Liquid Crystals IX*, edited by I.-C. Khoo (SPIE, Bellingham, WA, 2005), Vol. 5936-27.

J. B. Oliver, T. J. Kessler, H. Huang, J. Keck, A. L. Rigatti, A. W. Schmid, A. Kozlov, and T. Z. Kosc, "Thin-Film Design for Multilayer Diffraction Gratings," in *Laser-Induced Damage in Optical Materials: 2005*, edited by G. J. Exarhos, A. H. Guenther, K. L. Lewis, D. Ristau, M. J. Soileau, and C. J. Stolz (SPIE, Bellingham, WA, 2005), Vol. 5991, pp. 402–408.

J. B. Oliver, A. L. Rigatti, J. D. Howe, J. Keck, J. Szczepanski, A. W. Schmid, S. Papernov, A. Kozlov, and T. Z. Kosc, "Thin-Film Polarizers for the OMEGA EP Laser System," in *Laser-Induced Damage in Optical Materials: 2005*, edited by G. J. Exarhos, A. H. Guenther, K. L. Lewis, D. Ristau, M. J. Soileau, and C. J. Stolz (SPIE, Bellingham, WA, 2005), Vol. 5991, pp. 394–401.

S. Papernov, A. W. Schmid, A. L. Rigatti, J. B. Oliver, and J. D. Howe, "Damage Behavior of HfO_2 Monolayer Film Containing Gold Nanoparticles as Artificial Absorbing Defects," in *Laser-Induced Damage in Optical Materials: 2005*, edited by G. J. Exarhos, A. H. Guenther, K. L. Lewis, D. Ristau, M. J. Soileau, and C. J. Stolz (SPIE, Bellingham, WA, 2005), Vol. 5991, pp. 429–435.

O. Sadot, V. A. Smalyuk, J. A. Delettrez, D. D. Meyerhofer, T. C. Sangster, R. Betti, V. N. Goncharov, and D. Shvarts, "Observation of Self-Similar Behavior of the 3D, Nonlinear Rayleigh–Taylor Instability," Phys. Rev. Lett. **95**, 265001 (2005).

V. A. Smalyuk, O. Sadot, J. A. Delettrez, D. D. Meyerhofer, S. P. Regan, and T. C. Sangster, "Fourier-Space Nonlinear Rayleigh–Taylor Growth Measurements of 3D Laser-Imprinted Modulations in Planar Targets," Phys. Rev. Lett. **95**, 215001 (2005).

C. Stoeckl, T. R. Boehly, J. A. Delettrez, S. P. Hatchett, J. A. Frenje, V. Yu. Glebov, C. K. Li, J. E. Miller, R. D. Petrasso, F. H. Séguin, V. A. Smalyuk, R. B. Stephens, W. Theobald, B. Yaakobi, and T. C. Sangster, "Direct-Drive Fuel-Assembly Experiments with Gas-Filled, Cone-in-Shell, Fast-Ignitor Targets on the OMEGA Laser," Plasma Phys. Control. Fusion **47**, B859 (2005).

L. Zheng, J. C. Lambropoulos, and A. W. Schmid, "Molecular Dynamics Study of UV-Laser-Induced Densification of Fused Silica. II. Effects of Laser Pulse Duration, Pressure, and Temperature, and Comparison with Pressure-Induced Densification," J. Non-Cryst. Solids **351**, 3271 (2005).

Forthcoming Publications

Y. V. Artemova, G. S. Bisnovatyi-Kogan, I. V. Igumenshchev, and I. D. Novikov, "Black Hole Advective Accretion with Optical Depth Transition," to be published in the Astrophysical Journal.

R. Betti and C. Zhou, "Low-Adiabat Implosions for Fast-Ignition Inertial Confinement Fusion," to be published in Inertial Fusion Sciences and Applications 2005.

T. R. Boehly, E. Vianello, J. E. Miller, R. S. Craxton, T. J. B. Collins, V. N. Goncharov, I. V. Igumenshchev, D. D. Meyerhofer, D. G. Hicks, P. M. Celliers, and G. W. Collins, "Shock-Timing Experiments Using Double-Pulse Laser Irradiation," to be published in Physics of Plasmas (invited).

A. C.-A. Chen, J. U. Wallace, S. K.-H. Wei, L. Zeng, and S. H. Chen, "Light-Emitting Organic Materials with Variable Charge Injection and Transport Properties," to be published in Chemistry of Materials.

D. Clay, D. Poslunsy, M. Flinders, S. D. Jacobs, and R. Cutler, "Effect of $LiAl_5O_8$ Additions on the Sintering and Optical Transparency of LiAlON," to be published in the Journal of European Ceramic Society.

J. L. DeCiantis, F. H. Séguin, V. Berube, M. J. Canavan, C. D. Chen, J. A. Frenje, S. Kurebayashi, C. K. Li, J. R. Rygg, B. E. Schwartz, R. D. Petrasso, J. A. Delettrez, S. P. Regan, V. A. Smalyuk, V. Yu. Glebov, J. P. Knauer, F. J. Marshall, D. D. Meyerhofer, S. Roberts, T. C. Sangster, C. Stoeckl, K. Mikaelian, H. S. Park, and H. F. Robey "Proton Core Imaging of the Nuclear Burn in Inertial Confinement Fusion Implosions," to be published in Review of Scientific Instruments.

D. H. Edgell, W. Seka, R. S. Craxton, L. M. Elasky, D. R. Harding, R. L. Keck, L. D. Lund, and M. D. Wittman, "Characterization of Cryogenic Direct-Drive ICF Targets During Layering Studies and Just Prior to Shot Time," to be published in Inertial Fusion Sciences and Applications 2005.

D. H. Edgell, W. Seka, R. S. Craxton, L. M. Elasky, D. R. Harding, R. L. Keck, and M. D. Wittman, "Analysis of Cryogenic Target Shadowgraphs at LLE," to be published in Fusion Science and Technology.

V. N. Goncharov, O. V. Gotchev, R. L. McCrory, P. W. McKenty, D. D. Meyerhofer, T. C. Sangster, S. Skupsky, and C. Cherfils-Clérouin, "Ablative Richtmyer–Meshkov Instability: Theory and Experimental Results," to be published in Inertial Fusion Science and Applications 2005.

V. N. Goncharov, O. V. Gotchev, E. Vianello, T. R. Boehly, J. P. Knauer, P. W. McKenty, P. B. Radha, S. P. Regan, T. C. Sangster, S. Skupsky, V. A. Smalyuk, R. Betti, R. L. McCrory, D. D. Meyerhofer, W. Manheimer, D. Colombant, and C. Cherfils-Clérouin, "Early Stage of Implosion in Inertial Confinement Fusion: Shock Timing and Perturbation Evolution," to be published in Physics of Plasmas.

D. R. Harding, D. D. Meyerhofer, S. J. Loucks, L. D. Lund, R. Janezic, L. M. Elasky, T. H. Hinterman, D. H. Edgell, W. Seka, M. D. Wittman, R. Q. Gram, and M. J. Bonino, "Forming Smooth Cryogenic Target Layers for OMEGA Direct-Drive ICF Implosions and Prospects for Direct-Drive Targets for the NIF," to be published in Physics of Plasmas (invited).

J. H. Kelly, L. J. Waxer, V. Bagnoud, I. A. Begishev, J. Bromage, B. E. Kruschwitz, T. J. Kessler, S. J. Loucks, D. N. Maywar, R. L. McCrory, D. D. Meyerhofer, S. F. B. Morse, J. B. Oliver, A. L. Rigatti, A. W. Schmid, C. Stoeckl, S. Dalton, L. Folnsbee, M. J. Guardalben, R. Jungquist, J. Puth, M. J. Shoup III, D. Weiner, and J. D. Zuegel, "OMEGA EP: High-Energy Petawatt Capability for the OMEGA Laser Facility," to be published in Inertial Fusion Sciences and Applications 2005.

A. K. Knight and D. R. Harding, "Modeling the Sensitivity of a Polymer Vapor Deposition Process to Different Operating Conditions and Parameters," to be published in Fusion Science and Technology.

B. E. Kruschwitz, R. Jungquist, J. Qiao, S. Abbey, S. E. Dean, D. N. Maywar, M. D. Moore, L. J. Waxer, and M. E. Wilson, "Large-Aperture Deformable Mirror Correction of Tiled-Grating Wavefront Error," to be published in Inertial Fusion Sciences and Applications 2005.

S. I. Kudryashov, S. D. Allen, S. Papernov, and A. W. Schmid, "Nanoscale Laser-Induced Spallation in SiO_2 Films Containing Gold Nanoparticles," to be published in Applied Physics B.

C. K. Li and R. D. Petrasso, "Energy Deposition of MeV Electrons in Compressed Targets of Fast-Ignition Inertial Confinement Fusion," to be published in Physics of Plasmas.

C. K. Li and R. D. Petrasso, "Stopping, Straggling, and Blooming of Directed Energetic Electrons in Hydrogenic and Arbitrary-*Z* plasmas," to be published in Physical Review E.

J. A. Marozas, F. J. Marshall, R. S. Craxton, I. V. Igumenshchev, S. Skupsky, P. B. Radha, T. J. B. Collins, R. Epstein, P. W. McKenty, M. J. Bonino, D. Jacobs-Perkins, D. D. Meyerhofer, T. C. Sangster, J. P. Knauer, V. A. Smalyuk, V. Yu. Glebov, S. G. Noyes, W. Seka, and R. L. McCrory, "Progress in Polar-Direct-Drive Simulations and Experiments," to be published in Physics of Plasmas (invited).

F. J. Marshall, R. S. Craxton, M. J. Bonino, R. Epstein, V. Yu. Glebov, D. Jacobs-Perkins, J. P. Knauer, J. A. Marozas, P. W. McKenty, S. G. Noyes, P. B. Radha, W. Seka, S. Skupsky, V. A. Smalyuk, J. A. Frenje, C. K. Li, R. D. Petrasso, and F. H. Séguin, "Polar-Direct-Drive Experiments on OMEGA," to be published in Inertial Fusion Science and Applications 2005.

R. L. McCrory, D. D. Meyerhofer, S. J. Loucks, S. Skupsky, R. Betti, T. R. Boehly, T. J. B. Collins, R. S. Craxton, J. A. Delettrez, D. H. Edgell, R. Epstein, K. A. Fletcher, C. Freeman, J. A. Frenje, V. Yu. Glebov, V. N. Goncharov, D. R. Harding, I. V. Igumenshchev, R. L. Keck, J. D. Kilkenny, J. P. Knauer, C. K. Li, J. R. Marciante, J. A. Marozas, F. J. Marshall, A. V. Maximov, P. W. McKenty, S. F. B. Morse, J. Myatt, S. Padalino,

R. D. Petrasso, P. B. Radha, S. P. Regan, T. C. Sangster, F. H. Séguin, W. Seka, V. A. Smalyuk, J. M. Soures, C. Stoeckl, B. Yaakobi, and J. D. Zuegel, "Progress in Direct-Drive Inertial Confinement Fusion Research at the Laboratory for Laser Energetics," to be published in Inertial Fusion Sciences and Applications 2005.

F. H. Séguin, J. L. DeCiantis, J. A. Frenje, C. K. Li, J. R. Rygg, R. D. Petrasso, J. A. Delettrez, S. P. Regan, V. A. Smalyuk, V. Yu. Glebov, J. P. Knauer, F. J. Marshall, D. D. Meyerhofer, S. Roberts, T. C. Sangster, C. Stoeckl, K. Mikaelian, H. S. Park, and H. F. Robey "Measured Dependence of Burn Profiles on Implosion Conditions in Inertial Confinement Fusion Experiments," to be published in Physics of Plasmas.

W. T. Shmayda, R. Janezic, T. W. Duffy, D. R. Harding, and L. D. Lund, "Tritium Operations at the Laboratory for Laser Energetics," to be published in Fusion Science and Technology.

S. Skupsky, R. S. Craxton, F. J. Marshall, R. Betti, T. J. B. Collins, R. Epstein, V. N. Goncharov, I. V. Igumenshchev, J. A. Marozas, P. W. McKenty, P. B. Radha, J. D. Kilkenny, D. D. Meyerhofer, T. C. Sangster, and R. L. McCrory, "Polar Direct Drive—Ignition at 1-MJ," to be published in Inertial Fusion Sciences and Applications 2005.

V. A. Smalyuk, O. Sadot, R. Betti, V. N. Goncharov, J. A. Delettrez, D. D. Meyerhofer, S. P. Regan, T. C. Sangster, and D. Shvarts, "Rayleigh–Taylor Growth Measurements of 3-D Modulations in Nonlinear Regime," to be published in Physics of Plasmas (invited).

C. Stoeckl, J. A. Delettrez, J. H. Kelly, T. J. Kessler, B. E. Kruschwitz, S. J. Loucks, R. L. McCrory, D. D. Meyerhofer, D. N. Maywar, S. F. B. Morse, J. Myatt, A. L. Rigatti, L. J. Waxer, J. D. Zuegel, and R. B. Stephens, "High-Energy Petawatt Project at the University of Rochester's Laboratory for Laser Energetics," to be published in Fusion Science and Technology.

S. Wu, P. Geiser, J. Jun, J. Karpinski, J.-R. Park, and R. Sobolewski, "Long-Lived Coherent Acoustic Oscillators in GaN Single Crystals," to be published in Applied Physics Letters.

J. D. Zuegel, S. Borneis, C. Barty, B. LeGarrec, C. Danson, N. Miyanaga, P. K. Rambo, T. J. Kessler, A. W. Schmid, L. J. Waxer, B. E. Kruschwitz, R. Jungquist, N. Blanchot, E. Moses, J. Britten, C. LeBlanc, F. Amiranoff, J. L. Porter, J. Schwarz, M. Geissel, I. C. Smith, I. Jovanovic, and J. Dawson, "Laser Challenges for Fast Ignition," to be published in Fusion Science and Technology.

Conference Presentations

The following presentations were made at the 11th International Topical Meeting on Optics of Liquid Crystals, Sand Key, FL, 2–7 October 2005:

S. G. Lukishova, N. Lepeshkin, R. W. Boyd, and K. L. Marshall, "Feedback-Free Hexagon Pattern Formation with Liquid Crystals and Isotropic Liquids."

S. G. Lukishova and A. W. Schmid, "Near-Field Optical Microscopy of Cholesteric Oligomeric Liquid Crystal Layers."

S. G. Lukishova, A. W. Schmid, C. M. Supranowitz, A. J. McNamara, P. Freivald, R. P. Knox, R. W. Boyd, and C. R. Stroud, "Single-Photon Source for Quantum Information Based on Single Dye Molecule Fluorescence in Liquid Crystal Host."

K. L. Marshall, K. Adelsberger, G. Mhyre, and D. W. Griffith, "The LCPDI: A Compact and Robust Phase-Shifting, Point-Diffraction Interferometer Based on Dye-Doped LC Technology."

K. L. Marshall, G. Painter, K. Lotito, A. G. Noto, and P. Chang, "Transition Metal Dithiolene Near-IR Dyes and Their Applications in Liquid Crystal Devices" (invited).

The following presentations were made at the 47th Annual Meeting of the APS Division of Plasma Physics, Denver, CO, 24–28 October 2005:

K. Anderson and R. Betti, "2-D Simulations of Adiabat-Shaped Targets."

R. Betti and C. Zhou, "Fuel Assembly for Fast-Ignition Inertial Confinement Fusion."

R. Betti and C. Zhou, "High-Density and High-ρR-Fuel Assembly for Fast-Ignition Inertial Confinement Fusion."

T. R. Boehly, E. Vianello, J. E. Miller, R. S. Craxton, T. J B. Collins, V. N. Goncharov, I. V. Igumenshchev, D. D. Meyerhofer, D. G. Hicks, P. M. Celliers, and G. W. Collins, "Shock-Timing Experiments Using Double-Pulse Laser Irradiation" (invited).

M. J. Canavan, J. A. Frenje, R. Leiter, C. K. Li, J. R. Rygg, F. H. Séguin, R. D. Petrasso, and S. Roberts, "Characterization of a Fusion Product Source for ICF Diagnostic Development."

D. T. Casey, J. A. Frenje, C. K. Li, J. R. Rygg, F. H. Séguin, R. D. Petrasso, V. Yu. Glebov, D. D. Meyerhofer, T. C. Sangster, C. Stoeckl, S. W. Haan, S. P. Hatchett, P. A. Amendt, D. Eder, N. Izumi, O. L. Landen, R. A. Lerche, D. C. Wilson, R. Leeper, and R. E. Olson, "Design of the Shielding for the Magnetic Recoil Spectrometer (MRS) on OMEGA and the NIF Using the Neutron Transport Code TART2002."

C. D. Chen, C. K. Li, J. A. Frenje, F. H. Séguin, R. D. Petrasso, J. Myatt, and J. A. Delettrez, "Monte Carlo Simulations for Studying Hot-Electron Transport in Nondegenerate Plasmas of Arbitrary Z."

T. J. B. Collins, P. W. McKenty, P. B. Radha, V. N. Goncharov, and S. Skupsky, "Stability and Performance of a Direct-Drive, 1-MJ, Wetted-Foam Target Design."

R. S. Craxton, F. J. Marshall, M. J. Bonino, S. G. Noyes, and V. A. Smalyuk, "Radiation Transport in Saturn Targets Used for Polar Direct Drive."

J. A. Delettrez, J. Myatt, P. B. Radha, C. Stoeckl, and D. D. Meyerhofer, "Hydrodynamic Simulations of Integrated Experiments Planned for the OMEGA/OMEGA EP Laser Systems."

D. H. Edgell, R. S. Craxton, L. M. Elasky, D. R. Harding, L. S. Iwan, R. L. Keck, L. D. Lund, S. J. Verbridge, M. J. Wittman, and W. Seka, "Calibration of Cryogenic Target Optical Shadowgraphic Characterization."

R. Epstein, T. J. B. Collins, J. A. Delettrez, V. N. Goncharov, J. P. Knauer, J. A. Marozas, P. W. McKenty, P. B. Radha, and V. A. Smalyuk, "Effects of Perturbed Picket Pulses in Adiabat-Shaped Direct-Drive Implosion Experiments."

J. A. Frenje, D. T. Casey, C. K. Li, J. R. Rygg, F. H. Séguin, S. Volkmer, R. D. Petrasso, V. Yu. Glebov, D. D. Meyerhofer, T. C. Sangster, C. Stoeckl, S. W. Haan, S. P. Hatchett, P. A. Amendt, D. Eder, N. Izumi, O. L. Landen, R. A. Lerche, D. C. Wilson, R. Leeper, and O. L. Olson, "A Magnetic Recoil Spectrometer (MRS) for ρR, Yield, and T_i Measurements of Implosions on OMEGA and the NIF."

M. Ghilea, D. D. Meyerhofer, T. C. Sangster, D. Lonobile, A. Dillenbeck, R. A. Lerche, and L. Disdier, "Neutron Imaging with Bubble Chambers."

V. Yu. Glebov, T. C. Sangster, S. Roberts, M. J. Moran, and B. Davis, "Neutron Time-of-Flight Detectors Based on Vacuum Photodiodes for the NIF and LMJ."

V. N. Goncharov, G. Li, P. B. Radha, J. A. Delettrez, A. V. Maximov, and R. L. McCrory, "Electron Transport Modeling in Inertial Confinement Fusion Experiments."

O. V. Gotchev, D. D. Meyerhofer, and C. Stoeckl, "A Compact, Multiangle Electron Spectrometer for Ultra-Intense Laser–Plasma Interaction Experiments."

L. Guazzotto, R. Betti, and J. P. Freidberg, "First Results of a Linear MHD Stability Code for Axisymmetric Plasmas with Arbitrary Equilibrium Flow."

D. R. Harding, D. D. Meyerhofer, S. J. Loucks, L. D. Lund, R. Janezic, L. M. Elasky, T. H. Hinterman, D. H. Edgell, W. Seka, M. D. Wittman, R. Q. Gram, and M. J. Bonino, "Forming Smooth Cryogenic Target Layers for OMEGA Direct-Drive ICF Implosions and Prospects for Direct-Drive Targets for the NIF" (invited).

I. V. Igumenshchev, R. S. Craxton, P. W. McKenty, J. A. Marozas, and S. Skupsky, "Reduction of the Effects of Nonuniform Laser Irradiation in Polar-Direct-Drive Implosions on the NIF."

P. A. Jaanimagi, R. Boni, and D. D. Meyerhofer, "Update on the Rochester Optical Streak System."

N. Jang, J. P. Knauer, R. Betti, and D. D. Meyerhofer, "Laser Driven Magnetic Field Compression."

J. P. Knauer, K. Anderson, R. Betti, T. J. B. Collins, V. Yu. Glebov, V. N. Goncharov, F. J. Marshall, D. D. Meyerhofer, P. B. Radha, S. P. Regan, T. C. Sangster, C. Stoeckl, J. A. Frenje, C. K. Li, R. D. Petrasso, and F. H. Séguin, "Direct-Drive, Low-Adiabat ICF Implosions."

C. K. Li and R. D. Petrasso, "Stopping, Straggling and Blooming of Directed Energetic Electrons in Hydrogenic and Arbitrary-*Z* Plasmas" (invited).

C. K. Li, F. H. Séguin, J. R. Rygg, J. A. Frenje, R. D. Petrasso, T. C. Sangster, V. A. Smalyuk, J. A. Delettrez, J. P. Knauer, S. P. Regan, J. M. Soures, F. J. Marshall, P. W. McKenty, D. D. Meyerhofer, C. Stoeckl, R. P. J. Town, A. J. MacKinnon, P. A. Amendt, N. Izumi, and O. L. Landen, "Proton Radiography of Electro-magnetic Fields Generated by Laser-Driven Plastic Foils."

D. Li and V. N. Goncharov, "Numerical Study of Temporal Density Variation Effects on Nonlinear Perturbation Evolution in Classical Rayleigh–Taylor Instability."

G. Li and V. N. Goncharov, "Effect of Ponderomotive Terms on Heat Flux in Laser-Produced Plasmas."

J. A. Marozas, F. J. Marshall, R. S. Craxton, I. V. Igumenshchev, S. Skupsky, P. B. Radha, T. J. B. Collins, R. Epstein, P. W. McKenty, M. J. Bonino, D. Jacobs-Perkins, D. D. Meyerhofer, T. C. Sangster, J. P. Knauer, V. A. Smalyuk, V. Yu. Glebov, S. G. Noyes, W. Seka, and R. L. McCrory, "Progress in Polar-Direct-Drive Simulations and Experiments" (invited).

F. J. Marshall, R. S. Craxton, M. J. Bonino, R. Epstein, V. Yu. Glebov, D. Jacobs-Perkins, J. P. Knauer, J. A. Marozas, P. W. McKenty, S. G. Noyes, P. B. Radha, W. Seka, S. Skupsky, V. A. Smalyuk, J. A. Frenje, C. K. Li, R. D. Petrasso, and F. H. Séguin, "Polar-Direct-Drive Experiments on OMEGA."

A. V. Maximov, J. Myatt, and R. W. Short, "Electron Distribution and Transport in a Laser Field in Direct-Drive ICF Plasmas."

P. W. McKenty and M. D. Wittman, "Role of Hydrogen Fractionation in ICF Ignition Target Designs."

D. D. Meyerhofer, T. C. Sangster, C. Stoeckl, S. F. B. Morse, J. H. Kelly, S. J. Loucks, and R. L. McCrory, "OMEGA EP: Status and Use Planning."

J. E. Miller, T. R. Boehly, D. D. Meyerhofer, and J. H. Eggert, "Equation-of-State Measurement in High Porosity Ta_2O_5 Foam."

J. Myatt, J. A. Delettrez, W. Theobald, C. Stoeckl, M. Storm, A. V. Maximov, R. W. Short, R. P. J. Town, and L. A. Cottrill, "Numerical Calculations of Laser-Generated MeV Electrons and Characteristic X-Ray Production in Copper Foil Targets."

R. D. Petrasso and C. K. Li, "Energy Deposition, Penetration, and Blooming of Energetic Electrons in Fast Ignition and Preheat Scenarios."

P. B. Radha, R. Betti, V. Yu. Glebov, V. N. Goncharov, J. P. Knauer, P. W. McKenty, J. A. Marozas, D. D. Meyerhofer, S. P. Regan, T. C. Sangster, and C. Stoeckl, "Two-Dimensional Simulations of Low-Adiabat Plastic-Shell Implosions on OMEGA."

S. P. Regan, J. A. Delettrez, V. Yu. Glebov, V. N. Goncharov, J. A. Marozas, F. J. Marshall, P. W. McKenty, D. D. Meyerhofer, P. B. Radha, T. C. Sangster, V. A. Smalyuk, C. Stoeckl, J. R. Rygg, J. A. Frenje, C. K. Li, R. D. Petrasso, and F. H. Séguin, "Target Performance of Direct-Drive, D_2-, D^3He-, and DT-Filled Plastic-Shell Implosions on OMEGA."

C. Ren, G. Li, and V. N. Goncharov, "Hot Electron Generation During ICF Target Compression."

J. R. Rygg, J. A. Frenje, C. K. Li, F. H. Séguin, R. D. Petrasso, J. A. Delettrez, V. Yu. Glebov, D. D. Meyerhofer, and T. C. Sangster, "Studies of Shock Convergence in ICF Implosions Using Nuclear Burn History Measurements."

O. Sadot, V. A. Smalyuk, J. A. Delettrez, D. D. Meyerhofer, T. C. Sangster, D. Shvarts, R. Betti, and V. N. Goncharov, "Measurements of Bubble Evolution in the Nonlinear Ablative Rayleigh–Taylor Instability."

T. C. Sangster, J. A. Delettrez, V. Yu. Glebov, V. N. Goncharov, D. R. Harding, J. P. Knauer, F. J. Marshall, P. W. McKenty, D. D. Meyerhofer, P. B. Radha, S. P. Regan, S. Skupsky, V. A. Smalyuk, C. Stoeckl, J. A. Frenje, C. K. Li, R. D. Petrasso, and F. H. Séguin, "Recent Cryogenic Implosion Results on OMEGA."

H. Sawada, S. P. Regan, T. R. Boehly, I. V. Igumenshchev, V. N. Goncharov, F. J. Marshall, B. Yaakobi, T. C. Sangster, D. D. Meyerhofer, G. Gregori, D. G. Hicks, S. H. Glenzer, and O. L. Landen, "Measurements of T_e and Z in Direct-Drive, Shock-Heated Planar Targets."

F. H. Séguin, J. DeCiantis, C. K. Li, J. A. Frenje, J. R. Rygg, R. D. Petrasso, S. P. Regan, J. A. Delettrez, R. Epstein, J. P. Knauer, F. J. Marshall, P. W. McKenty, D. D. Meyerhofer,

S. Roberts, T. C. Sangster, V. A. Smalyuk, K. Mikaelian, H. S. Park, H. F. Robey, and R. Tipton, "Measured Nuclear Burn Region Sizes and Symmetries for Different Capsule and Drive Conditions in Direct Drive."

W. Seka, H. Baldis, J. Myatt, A. V. Maximov, R. W. Short, R. S. Craxton, R. E. Bahr, and T. C. Sangster, "Stimulated Brillouin Scattering in Plasmas Relevant to Direct-Drive Laser Fusion."

R. W. Short and J. Myatt, "Relativistic Electron Beam Microinstabilities in the Fast-Ignition Regime."

S. Skupsky, R. S. Craxton, F. J. Marshall, R. Betti, T. J. B. Collins, R. Epstein, V. N. Goncharov, I. V. Igumenshchev, J. S. Keller, J. A. Marozas, P. W. McKenty, P. B. Radha, J. D. Kilkenny, D. D. Meyerhofer, T. C. Sangster, and R. L. McCrory, "Polar Direct Drive on the National Ignition Facility."

V. A. Smalyuk, O. Sadot, R. Betti, V. N. Goncharov, J. A. Delettrez, D. D. Meyerhofer, S. P. Regan, T. C. Sangster, and D. Shvarts, "Rayleigh–Taylor Growth Measurements of 3-D Modulations in Nonlinear Regime" (invited).

A. Solodov, R. Betti, and J. Myatt, "Stopping of Fast Electrons in Dense Hydrogenic Plasmas."

A. Solodov, C. Ren, J. Myatt, R. Betti, and W. B. Mori, "Simulation of Weibel Electromagnetic Instability of Electron Beams in Plasma Using the Codes LSP and OSIRIS."

C. Stoeckl, T. R. Boehly, J. A. Delettrez, J. Myatt, J. E. Miller, R. B. Stephens, W. Theobald, and T. C. Sangster, "Measurements of Plasma Filling Inside a Fast-Ignitor Cone Target Using Streaked Optical Pyrometry."

S. Sublett, J. P. Knauer, I. V. Igumenshchev, A. Frank, and D. D. Meyerhofer, "Temporal Evolution of Directly Driven Hydrodynamic Jets Relevant to Astrophysics."

W. Theobald, J. E. Miller, T. R. Boehly, E. Vianello, I. V. Igumenshchev, V. N. Goncharov, A. V. Maximov, and T. C. Sangster, "Optical Measurements at Preheated Polystyrene and Aluminum Layers."

S. Volkmer, F. H. Séguin, C. K. Li, J. R. Rygg, R. D. Petrasso, T. C. Sangster, V. Yu. Glebov, D. D. Meyerhofer, and C. Stoeckl, "Improved Signal-to-Background for Neutron Spectroscopy Through Coincidence Counting of Charged-Particle Tracks in CR-39 Detectors."

C. Zhou and R. Betti, "Shock Fast Ignition of Thermonuclear Fuel with High Areal Density."

S. G. Lukishova, A. W. Schmid, R. Knox, P. Freivald, S. Schrauth, L. Bissell, R. W. Boyd, C. R. Stroud, Jr., and K. L. Marshall, "Deterministically Polarized, Room Temperature Source of Single Photons," Single-Photon Workshop 2005: Sources, Detectors, Applications and Measurement Methods, Teddington, UK, 24–26 October 2005.